Scanning tunnelling microscopy studies of the graphitic superconductor CaC_6

Kaveh Christopher Rahnejat

A thesis presented for the degree of Doctor of Philosophy

Department of Physics and Astronomy

University College London

England

September, 2012

Declaration

I, Kaveh Christopher Rahnejat, confirm that the work presented in this thesis is my own. Where information has been derived from other sources, I confirm that this has been indicated in the thesis. Permission has been granted to the author for the electronic reproduction of all sourced copyrighted material in this e-thesis, unless otherwise redacted.

Acknowledgements

The road to a thesis is a long one. Years of hard work ultimately result in a single tome big enough to prop up the most broken of coffee tables. There's been a lot of help along the way, and there are many people to thank. My parents, Homer and Patricia, have supported me during this journey of work, life and science, and have suffered inordinantly waiting for me to complete this thesis. Not least of all they have financed almost the entirety of my life, perhaps making this the most expensive book they've ever bought. A special thanks to my brother, Adam, for tolerating me as a flatmate, and my little sister, Katie, because nothing motivates hard work like trying to avoid setting a bad example.

To my supervisor, Mark Ellerby, thank you for taking me on as a student, and for the years of guidance and help along the way. Thanks also to Chris Howard, who is the most excellent person to work with, and Nick Shuttleworth, for the random escapades that have punctuated our science careers. I would also like to thank all of the UCL Carbon group and the denizens of the F10 offices, past and present, for being a truly great group of people to work around. A special thanks to Ross Springell, James Chivall and Nick for making our golden age of F10b a truly memorable, though perhaps not especially productive, office to work in.

I'd also like to thank all of the LCN STM group, for being a great group and a great lab to work in. In particular I'd like to thank Ben Bryant for teaching me how to use an STM and starting me off on my career as an STM scientist, and Gabriel Aeppli for being an incredibly busy genius who nevertheless found a lot of time to help me with my work and in publishing my first paper. In that vein I'd also like to thank Cyrus Hirjibehedin, Katsuya Iwaya and Steven Schofield for their help in perfecting the analysis of the data and getting it published. I'd like to thank all of the collaborators I've worked with over the years, with a special mention to Christoph Renner, who is a pleasure to work and discuss ideas with. Last but not least, I'd like to thank my cousin Roya, and my friends Matthew Stratton, Michael Pearce, David Kane, Adam Harvey-Thompson, Simon Hardy and Graham Wilson for their morale-boosting distractions during the thesis writing process. To anyone I may have missed, I assure you it is not deliberate.

Thank you all, I quite literally could not have done it without you.

Abstract

Graphitic systems have an electronic structure that can be readily manipulated through electrostatic or chemical doping, resulting in a rich variety of electronic ground states. One such class of materials are graphite intercalation compounds, a significant number of which exhibit superconductivity at low temperatures. The optimal superconductor in this class is CaC_6, which superconducts at 11.5 K. This thesis presents the first atomic-resolution surface studies of CaC_6 revealing not only the surface structure but also, via detailed spectroscopic imaging and Fourier transform techniques, a stripe phase. This stripe phase corresponds to a charge density wave with a period three times that of the Ca superlattice. The work presented in this thesis is the first such reporting and detailed characterization of a charge density wave in a graphitic material. Of further interest is the fact that the stripe phase is found to modulate the Ca lattice but no distortion of the graphene lattice is found indicating the graphene sheets may host the ideal, purely electronic, charge density wave. The implications for the understanding of superconductivity in CaC_6, graphene and the apparent ubiquity of CDWs with superconductivity in anisotropic layered materials are discussed.

Contents

List of Figures

Nomenclature

1D	One dimensional
2D	Two dimensional
3D	Three dimensional
AC	Alternating current
AR	Atomic resolution or atomically resolved
ARPES	Angle-resolved photoelectron spectroscopy
BCS	Barden-Cooper-Schrieffer
CaC_6	Calcium graphite
CDW	Charge density wave
CITS	Current imaging tunnelling spectroscopy
DC	Direct current
DFT	Density functional theory
dFT	Discrete Fourier transform
DOS	Density of states
E_F	Fermi energy
FCC	Face centre cubic
FE	Field emission
FFT	Fast Fourier transform
FIB	Focused ion beam
FQHE	Fractional quantum Hall effect

FT Fourier transform

FWHM Full width half maximum

GIC Graphite intercalation compound

HOPG Highly orientated pyrolytic graphite

LDOS Local density of states

LT-STM Omicron low temperature STM

$NbSe_2$ Niobium diselenide

Pt-Ir Platinum-Iridium alloy

RT Room temperature

SDW Spin density wave

SEM Scanning electron microscopy

SI Spectroscopic imaging

SQUID Superconducting quantum interference device

STM Scanning tunneling microscope or microscopy

STS Scanning tunneling spectroscopy

T_c Superconducting temperature

UHV Ultra high vacuum

WKB Wentzel–Kramers–Brillouin

XRD X-ray diffraction

Chapter 1

Introduction

This chapter serves as a short introduction to the research and an overview of the thesis structure. The contents of the thesis, including the aims and motivation behind the research are discussed and a summary of the results and the methods used are also provided. The most significant results presented within the thesis, pertaining to the newly-discovered charge density wave (CDW) phase of CaC_6, are also reported in *Nature Communications* by Rahnejat *et al.* [1]

1.1 Aims, objectives and motivation

Superconductivity in CaC_6 was first discovered by *T. E. Weller* of the UCL Carbon Physics group in 2005. [2] When the work for this thesis first began in 2007 there were many questions regarding the nature of superconductivity in CaC_6 and indeed other alkali-earth and alkali-metal graphite intercalation compounds (GICs). A detailed account of the physical and electronic structures of graphite, alkali-earth-metal GICs, and in particular CaC_6 are included in Chapter 2. Included in this is a history of what is known about the nature of superconductivity in CaC_6 and the questions that still remain at time of writing.

Motivated by a desire to understand and characterise the superconducting phase of these materials a number of scanning tunnelling microscopy (STM) experiments were planned with the aim of measuring the superconducting gap, the anisotropy of the gap, and to image the superconducting vortex lattice. Measurements similar to these were reported by Bergeal *et al.* including successful measurement of a superconducting gap at approximately 10 K and STM imaging of a superconducting vortex lattice. [3] However, gap isotropy was not explored and the data did not include successful atomic resolution imaging, consequently the surface structure was not confirmed. Furthermore, at this time the purity of CaC_6 samples being used was significantly below 100%. For these reasons it was felt that improvements on the data could be made. In particular it was felt that successful atomic resolution imaging was vital for confirming that the surface structure matched the bulk as this is frequently not the case, e.g. surface reconstructions as seen in Au(100) [4], and to allow the possibility of exploring any potential anisotropy of the superconducting gap.

The task of achieving atomic resolution in GICs is extremely difficult. A number of challenges had to be overcome, starting with achieving sample purity close to 100%, and preparation of samples such that an atomically-flat surface could be achieved inside the STM without contamination of the air-sensitive samples at any point during fabrication, transfer and measurement. Details of how these challenges were overcome are included in Chapters 3 and 4.

Initial studies aiming to find the surface structure were performed at 78 K, with the intention of cooling the sample below the superconducting transition of 11.5 K once the surface had been characterised. However, imaging studies of the surface revealed a variety of surface types, including an unexpected uni-directional stripe phase commensurate with the expected CaC_6 structure. As a result of both experimental difficulties and progress made by other groups on the question of superconductivity in

CaC_6 the original studies of the superconducting phase were abandoned in favour of a detailed study of the newly-discovered stripe phase. Experiments were performed to fully characterise this phase, determining that the stripes are the manifestation of a CDW. The presentation and analysis of these results are discussed in Section 1.3. The history and mechanics of CDWs, including the study of CDWs by STM, and discussion of the possible link between CDW phases and superconductivity are included in Chapter 2.

1.2 Summary of methods

Chapters 3 and 4 cover all of the methods used in producing the results presented within this thesis as well as some information about the theory and history of the methods used where appropriate. Methods pertaining to the samples are covered in Chapter 3. These include the techniques used to fabricate samples, the details of how samples are characterised and the preparation of samples for STM experiments. Particular focus is given to determining the quality and purity of samples and the prevention of contamination. Chapter 4 presents methods which pertain to the STM, scanning tunnelling spectroscopy (STS) and spectroscopic imaging (SI-STM) measurements performed. These include both a theoretical and practical description of each technique as well as the methodology of tip preparation and the steps taken in maintaining the STM environment. Details of analysis techniques used for the interpretation of data, such as Fourier transform STM (FT-STM) and STS (FT-STS), are included. The use of FT-STS analysis for the characterisation of a CDW, in particular for associating local density of states (LDOS) features with non-dispersing reciprocal-space features, is a new and innovative method for analysing such phenomena. Chapter 4 also presents, as a proof-of-principle for the cutting-edge analysis techniques, example measurements and analysis of $NbSe_2$ taken from calibration data, the preparation of which is also described in Chapter 3. Other examples of CDW characteristics as reported in STM studies are included in the background, Chapter 2.

1.3 Summary of results

As part of the STM studies a range of different surface types were discovered for CaC_6. Broadly these can be divided into surfaces for which atomic resolution (AR) imaging was successfully achieved, which is a first as prior to the work reported in this thesis

there were no reports of successful imaging or determination of the CaC_6 surface structure, and those for which AR imaging was not achieved, much like the surfaces already reported. [3] The expected CaC_6 structure of graphene with a superlattice of Ca atoms forms the basis for all of the reported AR surfaces. However, interestingly a number of unexpected phases are discovered including a striped phase which, via detailed analysis and characterisation, is determined to be a CDW. It is demonstrated that the striped CDW phase is commensurate, reduces symmetry and exhibits both a LDOS gap at the Fermi level and a structural distortion of intercalant lattice both associated with the CDW wavevector. Imaging and spectroscopic studies of all the surface types discovered, together with detailed analysis and characterisation for each surface, are included in Chapter 5. All of the reported surfaces were studied at 78 K under ultra-high vacuum (UHV) conditions on high-purity CaC_6 samples.

Chapter 6 presents discussion and a comparison of the different surface types. Hypotheses regarding the underlying causes for some of the unexpected surface features encountered are included. Following the characterisation of the stripe phase there is a detailed discussion of potential mechanisms for the newly-discovered CDW and the possible implications for superconductivity in CaC_6 and other related doped-graphitic materials. The existence of a CDW in a graphitic superconductor, or indeed any graphitic system, is a significant new discovery and its impact for the study of this class of materials, and of 2D layered superconductors in general, is also discussed. There are a number of ways the research can be furthered, to study the interactions between the CDW and superconducting phases in CaC_6 and to search for CDW phases or superconductivity in other related GICs. It is also important to expand the study to find the relationship between the surface behaviour and potential behaviour in the bulk. Furthermore, the results reported, together with the recently-reported existence field-effect induced insulating Wigner crystal phases in graphene, suggest a possible strategy for driving graphene superconductivity. [5]

Chapter 2

Theory and Background

This chapter presents a background for the thesis. Topics covered include graphite, GICs and CaC_6 as well as superconductivity and CDWs. Particular focus is given to recent work on CaC_6, and to the relationship between superconductivity and CDWs in 2D layered materials. A number of examples of STM measurements of CDW systems, including highly studied transition metal dichalcogenide 2D layered superconductors are included.

2.1 Graphite and graphitic materials

2.1.1 Introduction to graphite

Graphite is a semi-metallic allotrope of carbon. In its most basic form it is a layered material of strong, flexible and inelastic flakes characterised by a strong sp^2 bonded hexagonal honeycomb lattice in-plane. Macroscopically it exhibits good electrical conducting properties and superlubricity. It is familiar to most people as the material used in pencil lead, although it has a multitude of other uses. A single layer of graphite is known as graphene, the archetypal 2D material [6, 7], which has a unique electronic structure that can be significantly modified not only when cut, folded or rolled to form carbon nanotubes, fullerines and other molecular carbon species [8], but also when assembled with dopant layers between graphene sheets to form graphite intercalation compounds. [9] The ground states of graphitic materials can be metallic, semi-metallic or semiconducting, depending on the allotrope form or intercalated species, and some have even been shown to superconduct [9, 10] with transition temperatures above 10 K. [2, 11]

Bulk graphite itself is available in a number of forms. On an atomic scale these forms should be identical. However, the macroscopic properties can vary significantly. Two different forms of crystalline, non-turbostratic graphite were used for the research reported in this thesis. The first, and most widely available form of crystalline graphite, is highly-oriented pyrolytic graphite (HOPG). This is graphite created synthetically through chemical vapour deposition then mechanically pressed such that the angular difference between the graphene sheets is less than 1^o. This high level of c-axis alignment makes this form of graphite particularly popular for scientific research and for use in other applications, such as monochromators. Manufactured graphite also has other uses such as neutron moderators in nuclear reactors, electrodes, carbon fibre and various carbon-reinforced materials. The degree of ordering between the graphene planes is called the mosaic spread. One advantage of HOPG, beyond those already mentioned, is that samples of any size can be fabricated. However, a significant drawback is the fact that HOPG samples are polycrystalline in-plane, i.e. crystal size and alignment is good between the layers but poor in the directions which run parallel to the plane of the graphene layers. [12] The crystals are typically a few μm in size and do not necessarily share the same in-plane orientation. HOPG is available in a range of qualities, ZYA being the highest quality with the lowest surface roughness and mosaic spread and ZYH being the lowest quality. The quality is determined

by the manufacturer using finding X-ray diffraction (XRD). Typically manufacturers quote better than 10 ppm ash or other contaminants in HOPG samples. Most of the research presented was performed using ZYA-grade HOPG or HOPG-based samples.

The alternative form of graphite used in these experiments and GIC fabrication was natural crystalline graphite. This is naturally formed, flat, plate-like graphite, typically available only in very small flake sizes measuring a few mm in diameter and significantly less than 1 mm in thickness. Despite this limited size these samples are highly crystalline even in-plane where crystals can exceed 250 μm in size and have a very low defect count. [12] However, the mosaic spread in natural flake graphite is slightly worse than the highest grade of HOPG. Typical uses of natural graphite include a wide range of applications such as dry lubrication, steelmaking, pencils, zinc-carbon batteries, brake linings and as a substitute for asbestos.

2.1.2 Importance of graphite

Further to the applications already discussed in Section 2.1.1, graphite has long been a technologically and scientifically important material. In 1924 graphite was used as the test sample for very early XRD experiments by *J. D. Bernal*. [13] Graphite has also played an important role in the development of other scientific techniques including, but not limited to, the development of STM techniques in the 1980s by *Binnig* and *Rohrer*. [14] Graphite itself is highly studied, in all of its numerous forms, in particular because of its percieved importance as a potential electronic material of the future. Much of this promise comes from the wide variety of graphitic allotropes and the ease of electronic manipulation and modification through doping [9], field effects [5, 15] and structural modification [8] leading to useful electronic properties such as lightweight, inexpensive, easily-produced superconductors. As an electronic material graphene has already demonstrated the potential for flexible transparent displays [16], replacing indium tin oxide in flat screens, and GICs are already used in battery technology. It is hoped that continued research in the field will pave the way for new and exciting technologies such as superconducting wires, single-electron transistors [17] and hydrogen storage technology. [18]

2.1.3 Crystal and electronic structure

Graphite is a layered, low dimensional (2D) carbon allotrope. Each layer, referred to as a graphene sheet, is made up of a honeycomb hexagonal network of sp^2 bonded carbon atoms with a binding energy of 7 eV per carbon. In raw, undoped graphite

Figure 2.1: The structure of graphite with the Bernal stacking arrangement. The crystallographic coordinates of the atoms in the unit cell are clearly marked and the unit cell itself contains four carbon atoms and is indicated by the parallelepiped which touches all three marked directional axes. Image source: [9]

the unit cell measures 0.246 nm in size containing four carbon atoms with a C-C bond length of 0.142 nm. Electronic or structural manipulation of the graphite can result in doping or depletion of bonding or anti-bonding orbitals which can cause the hexagonal network to become more or less dense. The sp^2 bonding is extremely strong, in fact the C-C bonds in-plane are stronger than the sp^3 C-C bonds in diamond, but the graphene layers themselves are held together by van der Waals bonding which has a binding energy of only 0.02 eV per carbon. Consequently graphite is extremely anisotropic with high strength, stiffness and conductivity in-plane but low mechanical strength and conductivity between the layers. This is what allows the mechanical isolation of graphene sheets, as reported by Novoselov *et al.* [6], and ultimately why graphene-based structures such as carbon nanotubes and fullerines are feasible. This in-plane strength is also one of the reasons why graphite is used in numerous mechanical applications. The distance between the graphene sheets in unintercalated graphite at ambient pressure is 0.335 nm. However, the weak interlayer bonding means that relatively little energy is required to change the size of the gap between the sheets, this is one of the reasons graphite can be intercalated to form GICs. Sheets stack with an ABAB registry, i.e. every other sheet of graphene is aligned perfectly in-plane but those inbetween are laterally translated such that half the carbons ("A" type) rest above or below another carbon atom in an adjacent layer but the other half ("B" type) rest between the holes of the carbon hexagons of the layers above and below. Consequently, the unit cell contains two layers of carbon atoms, the complete structure and unit cell are presented in Fig. 2.1 which shows clearly that the unit cell contains four carbons. This structure was first resolved by *J. D. Bernal* [13] and the stacking registry is commonly known as Bernal stacking. Special cases for structures which deviate from the Bernal structure have been reported over the years but are not relevant to the work reported in this thesis, they are nonetheless well documented in a letter by *E. J. Freise.* [19] It is conventional in graphitic systems, and indeed other layered materials, to refer to the out-of-plane direction as the c-axis and the directions perpendicular to the plane as the ab-plane or basal plane.

The hexagonal graphite Brillouin zone is presented in Fig. 2.2. The carbon atoms

Figure 2.2: The hexagonal graphite Brilluoin zone showing a schematic representation of the graphitic electron and hole pockets found at the high symmetry H, H', K and K' points. The Γ-K directions lie in-plane and the Γ-A directions are out of plane. Image source: [9]

are held in-plane by strongly-coupled trigonal bonding and anti-bonding σ bands which are formed by the hybridization of the carbon 2s, $2p_x$ and $2p_y$ orbitals. [9] The remaining carbon p_z orbitals form the valence band, a single bonding π band, and the conduction band, a single antibonding π^* band. These bands are degenerate at the six equivalent K points, through which the Fermi level passes, in the Brilluoin zone. At each K point the DOS is proportional to energy, i.e. the band structure has a linear dispersion approaching the Fermi level. This results in a Dirac cone, as shown in Fig. 2.3, whereby the π and π^* bands touch asymptotically at the K points. In the ground state the π bands are completely occupied and the π^* bands are completely empty. This is characterised by a V-shape zero band-gapped DOS around the Fermi level. The Dirac cone results in many of the interesting properties of graphene, such as ballistic transport, and is one of the reasons for the high levels of interest in graphene as an electronic material. [7, 8]

Because of the linear dispersion of the band structure even the smallest amount of doping shifts the Fermi level away from the Dirac point. This is so sensitive that even in bulk graphite (i.e. not a single graphene layer) the electronic structure is modified by the presence of adjacent graphene sheets. In this case the number of π bands is doubled due to the four carbons in the unit cell. These bands are subject to a weak interlayer interaction which results in a band overlap of approximately 40 meV at the Fermi level. This yields one electron and two hole pockets between the H and K points, as seen in Fig. 2.2. As a consequence of this DOS of bulk graphite is not zero at the Fermi level, but rather has a low carrier concentration five orders of magnitude below that which is seen for metals, resulting in the known graphitic semi-metallic behaviour. For an example measurement of the graphitic DOS see Fig. 4.5. Lastly graphite also exhibits a free-electron-like, parabolic band above the Fermi level, distributed between the graphene sheets, resulting from interlayer interactions. This is known as the interlayer band. [20, 21, 22] The full band structure of graphite may be calculated using the Slonczewski-Weiss-McClure model. [23]

Figure 2.3: The band structure of graphene showing the linear dispersion of the band structure at the Dirac points K and K' as illustrated by the focus inset. Image source: [24]

2.1.4 Graphite intercalation compounds

Graphite can act as a host for various atomic and molecular species, which are housed within the galleries between the graphene layers, to form GICs. Graphite accepts many intercalant species including various types of alkali, alkali-earth and rare earth metals, and even molecular such as halides. [9] The introduction of intercalants can positively or negatively dope the graphene host, this can in turn increase or decrease occupation of the π^* and π bands leading to a small, typically less than 1%, change in the C-C distance. [25] In the case of CaC_6 the graphitic hexagon distance is approximately 0.25 nm. [26] Conversely, the introduction of intercalant material can increase the graphene layer separation by as much as 200%, this is possible because of the weak interlayer forces. [9] In the case of MC_6 alkali-earth-metal-doped donor GICs, of which CaC_6 is one, dopant metal atoms are hosted between the graphene sheets in a regular lattice. Structurally these GICs are stage-1, this means that there is only one graphene sheet between adjacent intercalant layers; a stage-n compound has n layers of graphene between intercalant layers. Furthermore, the graphene sheets are displaced such that Bernal stacking is lost and the graphite stacking is AA. Two different crystal unit cell structures are found in this subclass of GICs: a hexagonal structure with AαAβ-stacking (Fig. 2.4a) and a rhombohedral structure with AαAβAγ-stacking (Fig. 2.4b) where the greek letters denote the stacking structure of intercalant layers. CaC_6 exhibits the rhombohedral structure with a graphene-to-graphene interlayer spacing of 0.4524 nm. From a top-down perspective, as seen in STM, one expects to measure a $\sqrt{3}a \times \sqrt{3}a$ unit cell determined by the hexagonal Ca superlattice, rotated by 30° (R30°) with respect to the graphene lattice, where $a = 0.25$ nm - the graphite hexagon size. [27] A schematic representation of this superlattice notation is given in Fig. 2.5. Whilst CaC_6 has not yet successfully been imaged with AR various other GICs have. [28, 29, 30, 31, 32]

The metal atoms also have a significant impact on the electronic structure, they donate some or all of their valence electrons to the graphitic host, some of which occupy the interlayer bands and some of which are donated to the π^* bands. As a consequence of this doping these GICs are metallic in nature, rather than semi-

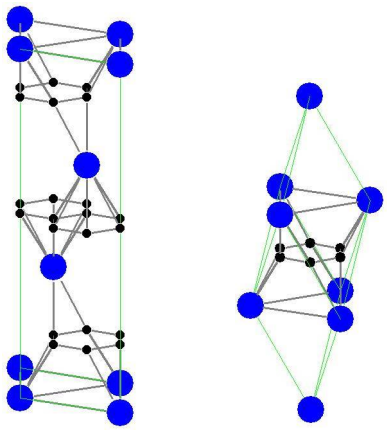

Figure 2.4: Schematics of the unit cells for (**a**) hexagonal and (**b**) rhombohedral structures of MC_6 GIC. Carbon atoms are shown by the small black spheres and intercalant atoms are shown by the big blue spheres.

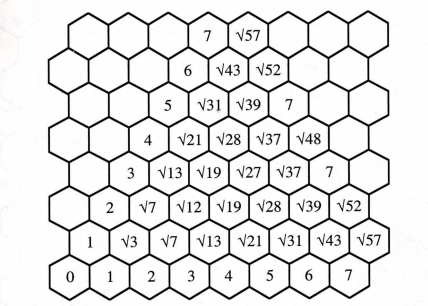

Figure 2.5: Superlattice notation for hexagonal systems. Image source: [33]

Figure 2.6: DFT-calculated LDOS as a function of energy (eV) of CaC_6 presented as a cumulative total of the DOS contributions of graphite and a number of Ca orbitals (as indicated in the legend). Note the position of the Dirac point at approximately -2 eV. Image source: [35]

metallic, and are also more 3D in nature than raw graphite, however, overall the materials remain anisotropic. [9] In CaC_6 density functional theory (DFT) calculation and angle-resolved photoelectron spectroscopy (ARPES) measurements indicate that 1.2 valence electrons per Ca atom are donated to graphitic bands [34, 35], most of this charge is thought to go to the π^* bands. The DOS of CaC_6 as calculated by Calandra *et al.* is presented in Fig 2.6, note that the charge donated by the Ca atoms means that the Fermi level is approximately 2 eV above the Dirac point.

In some cases the modification of the phonon and electronic band structures leads to superconductivity. CaC_6 is the optimal superconductor in this class with a T_C of 11.5 K at ambient pressure [2], an order of magnitude higher than most other GICs [9] and the highest of any bulk graphitic material, although it should be noted that some fullerine superconductors have higher superconducting temperatures. [36, 37] The superconducting properties and mechanisms of CaC_6 are discussed in Section 2.2.1.

In addition to superconductivity the high-tunability of the graphite electronic structure lends itself to various other phenomena. [38] Measurements of the fractional quantum Hall effect (FQHE) in graphene by field-effect doping reveal that Wigner crystals, insulating phases where electrons crystallize to form a lattice, can exist for the highest carrier densities of 10^{-3} electrons per carbon. [5, 15] This is still significantly less doping than the 0.2 electrons per carbon seen in CaC_6 or other chemically doped systems. Prior to the discovery of a CDW in CaC_6 [1] there was no substantiated report of a CDW in a graphitic material. [9] However, CDWs have been suggested as a possible origin for a variety of anomalous long-range superlattices seen in graphite intercalation compounds and graphite by electron diffraction [39] and STM. [30, 31, 32] Because of a lack of complementary electronic structure measurements, the authors of these reports were unable to rule out other effects, including Moiré patterns, which have been observed in graphite [40], electron standing waves, reported in various metals [41], and surface reconstruction or lattice depletion, seen in both GICs and other metals. [4, 32]

Perhaps the most interesting of these anomalous phenomena are the stripe orders

Figure 2.7: Topographic STM images of (**a**) CsC_8 and (**b**) RbC_8 exhibiting a uni-directional stripe phase. In the case of RbC_8 domain boundaries are seen at which the stripe period rotates. Images and original captions source: [32]

reported on CsC_8 and RbC_8 [32], shown in Fig. 2.7, both of which are donor alkali-metal GICs. [9] The stripes, which are seen with topographic STM imaging, form a uni-directional long range lattice and are reported to exist in topographic areas between 10 and 60 nm across. Domain boundaries are sometimes found for which the stripe direction rotates by 120° with respect to its original orientation. CsC_8 and RbC_8 are known to superconduct at very low temperatures below 0.1 K [42], and as MC_8 GICs they have a different 2×2 superlattice structure with which the stripes do not appear to be commensurate. The authors suggest a number of possible explanations including CDWs and surface reconstructions but with no spectroscopic or bias-dependent studies the true nature of the stripes is difficult to determine. Earlier measurements of the CsC_8 surface by ARPES measurement also highlighted the possibility of a CDW phase [43], although the authoratitive review paper by *Dresselhaus* and *Dresselhaus* does not consider CsC_8 to be an established CDW system. [9]

2.2 Superconductivity and charge density waves

This sections concerns two very interesting phenomena, namely CDWs and superconductivity. Both of these ground states are thought to arise from electron-phonon interactions. Tunnelling measurements, such as STM, allow detailed study of the LDOS which can reveal both physical and electronic information about the behaviour of electrons and the consequences of these electron-phonon interactions. Superconductivity is found in numerous GIC systems [2, 9, 44], but prior to publication of the results presented in this thesis there was no substantiated or characterised measurement of a CDW in a graphitic system.

This section presents a discussion of the mechanisms of superconductivity, with particular focus on BCS theory and superconductivity in CaC_6, and the mechanisms and nature of CDWs. Focus is given to the observation of CDWs in STM and STS measurements and the characteristics observed when measuring them. Additionally there is discussion of the possible connections between CDWs and superconductivity, in particular their apparent ubiquity in 2D layered materials with anisotropic electronic structures such as various cuprate [45], organic high-temperature superconductors

[46] and transition-metal dichalcogenide systems. [47] Whilst the connection between these two phenomena are not fully understood many theorists, particularly those working in high temperature superconductivity, believe that a full understanding the interaction could be vital for shedding light on the subtleties of the superconducting mechanism in numerous 2D layered systems.

2.2.1 Superconductivity

The story of ultra low temperature physics can be said to have started in 1908 when *H. Kamerlingh Onnes*, a physicist based in Leiden, successfully liquified helium for the first time. [48] This discovery allowed access to a wealth of new physics, liquid He could be used as a cryogen in experiments which could be performed at low temperatures. Perhaps the most dramatic result of this breakthrough came in 1911 when Onnes observed that the direct current (DC) resistivity of mercury dropped sharply to zero below 4.2 K (Fig. 2.8). [49] This was in sharp contrast to the low temperature metallic T^5 temperature dependence of DC resistivity expected by Onnes' competitors. [50] Although, it is now known that at the lowest temperatures most metals have a T^2 dependence. [51] Indeed, even the addition of impurities to the samples failed to produce a measureable resistance below the critical temperature. This newly discovered low temperature state of matter is known as superconductivity; a superconducting material may host a supercurrent which exhibits no resistance and no loss of energy so long as the material remains within the superconducting state. A wide range of materials exhibit superconductivity, however, the critical superconducting temperature T_C below which the superconducting state is found varies significantly between different superconductors. [48]

Progress in the field was initially slow, but in 1933 physicists *Meissner* and *Ochsenfeld* discovered that superconductors also expel magnetic flux, i.e. superconductors exhibit perfect diamagnetic behaviour. [52] This effect is known as the Meissner effect and, together with the drop in DC resistivity, they are considered the defining characteristics of a superconductor. It took a further 24 years for a microscopic understanding of superconductivity to be developed. In 1957 physicists *Bardeen*, *Cooper* and *Schrieffer* forwarded a theory explaining superconductivity in terms of an effective attraction between electrons mediated by vibrations of the lattice, known as phonons. [53] This theory, dubbed BCS theory, was remarkably successful in addressing the mystery of superconductivity and lead to the three physicists involved winning the Nobel prize in Physics in 1972.

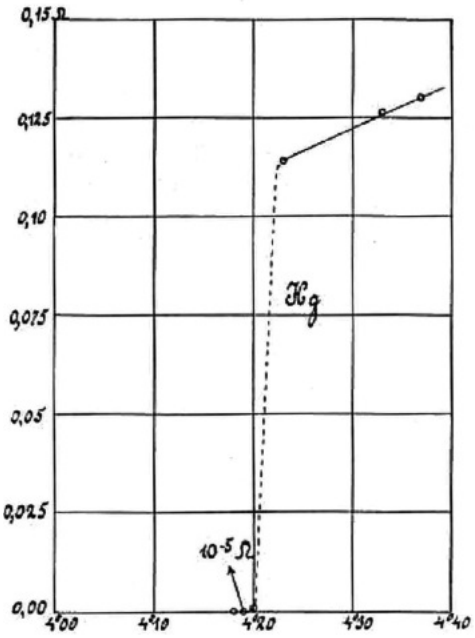

Figure 2.8: The discovery of superconductivity: The resistance of a Hg wire drops to zero below 4.2 K. Image source: [49]

At high temperatures vibrations of the lattice scatter electrons, impeding the flow of current, resulting in the electrical resistivity of metals. BCS theory states that at low temperature, below the superconducting transition temperature, in the presence of an attractive potential between electrons, the Fermi surface is unstable against the formation of a coherent many-body ground state known as Cooper pairing. In simple terms an electron may attract the positive nuclei of the lattice around it such that the lattice shields the electron creating a virtual positive charge, a second electron is then attracted to the region of increased positive charge density, by this mechanism a phonon is exchanged between the electrons mediating an attraction between them. As a consequence of this phonon-mediated attraction the two electrons of opposing spin overcome the Coulomb repulsion and form a Cooper pair. Above the superconducting transition the phonon coupling is suppressed by thermal noise before the interaction can occur, i.e. the pairing potential is insignificant compared to scattering from other phonons. Electrons are Fermions (integer-half spin) and as such as governed by the Pauli exclusion principle, this means that all of the electrons are correlated and as such to break one Cooper pair one must break all of them. However, when coupled together the paired state is treated as an integer spin Boson quasi-particle. These Bosons form a low energy Bose-Einstein condensate of many such pairs: in otherwords a charged (electron) super fluid ground state is formed resulting in superconductivity. Because all of the pairs are correlated a single gap opens in the energy spectrum, the gap

represents the energy required to break the pairing mechanism, this is known as the superconducting gap Δ_C which appears at T_C (above T_C this is exceeded by thermal energy) and grows with decreasing temperature. Assuming a weak attractive potential between electrons, and that the DOS does not vary greatly close to the Fermi surface, then BCS theory predicts the superconducting gap as shown in Equation 2.1.

$$\Delta_C = 1.74\Delta_0\sqrt{1-(\frac{T}{T_C})} \tag{2.1}$$

This applies for the condition $T \approx T_C$ where T is temperature, Δ_0 is the size of the superconducting gap at 0 K and there is no applied magnetic field. The size of Δ_0 is determined by the strength of the coupling between electrons and phonons. This varies between superconductors and is quantified in terms of the parameter-free result C_S expressed in Equation 2.2.

$$C_S = \frac{2\triangle_0}{k_B T_C} \tag{2.2}$$

For weakly coupled systems this coupling value is approximately 3.5, as for example in tin, but can be notably higher in strongly coupled systems. [48] This BCS estimate of coupling strength can in fact also be applied to non-BCS phonon-electron-mediated phases for systems such as CDWs. [54]

The Meissner effect is also explained by BCS theory. When a magnetic field is applied to a superconductor a supercurrent appears near the surface. The magnetic field of this supercurrent perfectly cancels the applied external field such that the interior of the superconductor expels all flux. Close to the surface the flux penetrates a short distance, in Type I superconductors flux is expelled up to a critical field after which the magnetic field is too strong, the spins of the Cooper pairs are aligned to the field and Cooper pairing is broken resulting in the material returning to the normal state. In Type II superconductors there are two critical fields, above a lower critical field flux is able to penetrate the superconductor, however, the small coherence lengths for the Cooper pairing in Type II superconductors means that vortices of supercurrent can form around the flux lines and the material is able to continue in the superconducting phase around these flux vortices. Above an upper critical field the material is, as with Type I, returned to the normal non-superconducting state. It is possible for the flux lattice of a Type II superconductor to be imaged inside an STM with a magnetic field applied between the lower and upper critical fields, as demonstrated for CaC_6 by Bergeal *et al.* [3]

BCS theory is particularly successful in modelling superconductivity in metallic systems. Prior to 1986 superconductivity had only been discovered in metals and metallic alloys with reported T_C values up to 23 K. In 1986 *Georg Bednorz* and *Alex Müller* reported that the cuprate insulator Ba-doped La_2CuO_4 exhibits superconductivity below 36 K. [55] This result lead to the discovery of many high temperature superconductors, including but not limited to cuprates, pnictides and organic superconductors, with superconducting temperatures even exceeding that of liquid nitrogen (77 K). In general BCS is found to apply less well to these high temperature superconductors, explanations for superconductivity in these systems favour electron-correlation or spin-fluctuation-mediated models [56] rather than the phonon-mediated model, but the importance of electron-phonon interactions are not discounted. [48]

Superconductors which are governed by BCS theory are generally referred to as conventional superconductors, and those which are not are referred to as unconventional superconductors. BCS is found to hold best for systems which are weakly-coupled, i.e. the attractive potential is small, but is flexible enough to be applied to strongly coupled systems as well. Following the 2005 discovery of superconductivity in CaC_6 by Weller *et al.* [2] a number of mechanisms were proposed including both weak and strongly-coupled conventional BCS, and unconventional plasmon-mediated superconductivity. [35, 57, 58, 59] However, in the years that have followed the general consensus of the GIC community is that the superconductivity in CaC_6 is conventional BCS, although the precise details of the mechanism are still widely debated, in particular the strength of the coupling and the specifics of which phonons and electrons are involved. Perhaps the strongest evidence that the superconductivity in CaC_6 is electron-phonon mediated comes from Hinks *et al.* who reported a Ca isotope effect on the superconducting temperature. [60] Change of isotope means a change in phonon modes because of the increased or decreased mass of the atomic species within the superconductor, when this leads to a change in superconducting temperature it is taken to mean that the phonons are important to superconductivity and therefore that the superconductivity is conventional and phonon-driven. The implication of Hinks' findings is that Ca phonon modes mediate the superconductivity, assuming a simple BCS model of the isotope effect. However, this is still not universally accepted at this time. There are also questions regarding which electronic bands are involved in the electron-phonon mechanism, numerous studies have been undertaken into both the phonon and electronic structure. Valla *et al.* report charge transfer of 1.2 electrons per Ca to the π^* bands and suggest these electrons play an important role in the

Figure 2.9: Peierls distortions: Schematic representations of (**a**) an undistorted 1D chain of atoms with a uniform charge density and metallic band structure, (**b**) a Peierls distorted 1D chain of atoms with a position-dependent sinusoidal charge distribution and gapped band structure. Images and original caption source: [65]

superconductivity [34], contrary to other measurements [61] and calculations [35, 58] suggesting that the intercalation process leads to increased occupancy of Ca-derived interlayer band and that this interlayer state play an important role. It would be fair to say that the community has not settled on any one specific explanation at this time, except to say that CaC_6 is probably a strongly-coupled [62] conventional s-wave [63, 64] Type II superconductor. Also of note is the fact that application of pressure can often also result in changes in superconducting temperature and this has indeed also been shown to be the case for CaC_6 for which T_C has been shown to increase linearly with applied hydrostatic pressure up to at least 15.1 K. [11]

2.2.2 Charge density waves

CDWs are a symmetry-reducing ground-state most commonly found in low-dimensional, anisotropic materials. [65, 66] Over the years CDWs have been interpreted as electron-phonon coupled states similar to superconductivity, or as collective electron states driven by electron-electron interactions. [67, 68, 69, 70] Ultimately strong involvement from both interactions is found in many CDW materials and systems are identified as CDWs by observation of characteristic behaviour which will be described in this section.

The most basic understanding of CDWs and lattice distortions comes from *Peierls* [71] who states that a 1D metal at absolute zero, in the absence of electron-electron and electron-phonon interactions, would form a period lattice with lattice spacing a (shown in the upper frame of Fig. 2.9). However, in the presence of electron-phonon interactions it becomes energetically favourable to introduce a lattice distortion (lower frame of Fig. 2.9) which is dependent on the Fermi wavevector k_F (Equation 2.3).

$$\lambda = \frac{\pi}{k_F} \tag{2.3}$$

This distortion, known as a Peierls distortion, results in the opening of a gap at the Fermi level, consequently the distorted phase is, in theory, semiconducting. The decrease in electronic energy is in competition with an increase in elastic energy of

the lattice. For small distortions and at low thermal energies the total energy of the coupled system is less than that of the undistorted metal. The size of the gap and magnitude of the distortion are determined by the point of maximal energy gain. The modification of the dispersion relation shown in Fig. 2.9 results in a periodic position-dependent charge distribution known as a CDW. When λ/a forms a rational fraction the CDW is said to be commensurate, when it does not the CDW is said to be incommensurate. At finite temperatures the amplitude of the distortion and the size of the gap are both found to be temperature dependent below a critical transition temperature T_{CDW}. Because the Peierls distortion is electron-phonon mediated one can apply Equation 2.2 to relate the critical temperature and gap size and this method has been used to estimate the strength of the coupling in a number of CDW systems. [54]

Whilst Peierls interpretation is useful in understanding how CDWs arise, it deviates from experimental measurements in a number of ways. When applying the model for a 1D chain to a real material, which is inevitably not truly 1D, a number of differences can arise. Firstly, many CDWs do not make a transition from a metal state to a semiconducting or insulating state. In these cases the opening of a gap associated with the period charge redistribution is seen as a depletion of the FS at the critical transition temperature which can be directly measured by DOS probes as a depletion of states close to the Fermi level. The period of such distortions are determined by Fermi surface nesting, i.e. correlation or coupling of electrons on the FS which are linked by the wavevector k_F. For this reason CDWs are most common in materials which have a highly anisotropic FS with points of high symmetry and which have crystal structures formed of chains of atoms. This typically results in parallel FS with a high probability of electron scattering between parallel states. Secondly, CDWs are not uniquely 1D, indeed 2D CDW lattices are common in materials such as transition-metal dichalcogenides [47, 72, 73], although 1D CDWs and stripe phases [74] are also common in both the same class of materials and in other materials such as blue and purple bronzes. [75, 76, 77, 78, 79] In a 1D or striped CDW system one expects the charge distribution to be near-perfectly sinusoidal in nature and as such for the wavefunctions for the occupied and unoccupied elements of the CDW to be perfectly out of phase. [67] In 2D systems this can also be true but it is not always the case since CDW elements working in different directions may cancel. However, Mallet *et al.* report quasi-perfect inversion of STM imaging contrast with bias polarity in $K_{0.9}Mo_6O_{17}$, a purple bronze system which exhibits a 2D hexagonal CDW lattice.

[79]

Much like superconductivity there are many special cases of CDWs for which the Peierls model does not hold particularly well, in particular the checkboard patterns found in high temperature cuprate superconductors, which contain numerous dispersing elements as well as elements of spin density wave (SDW) involvement [80], but nonetheless the pseudogap phases are believed by some to be CDW in nature. [45]

STM is a versatile probe of CDWs, and has a long history as such [81], because it accesses structural information regarding the position and distortions of the lattice as well as the electronic spectrum, including—most notably—the CDW gap. For more information about STM techniques see Chapter 4. Numerous CDW systems have been studied by STM, in particular $NbSe_2$, which is well-characterised by STM and frequently used as a test sample for calibration and analysis techniques (an example of this is provided in Chapter 4). Fig. 2.10 presents topographic imaging and LDOS measurements for the 1D CDW system $TbTe_3$. [77] In this system both a periodic, incommensurate stripe modulation and a CDW gap at the Fermi level are seen. These are both characteristic indicators of CDWs in STM. Of particular note is the fact that the CDW gap is of order 300 mV, which is significantly larger than a superconducting gap, but not necessarily outside the normal range for a CDW. [54] The small gap depth indicates the CDW is extremely subtle and this is consistent with the small topographic presence of the stripe. As postulated earlier in this section, as for many real CDW systems, the gap does not extend to zero occupancy, i.e. the CDW transition is metal-metal and not metal-semiconducting. Another 1D CDW system is Na-intercalated VSe_2. [76] The sinusoidal influence of the CDW on the measured topography of the surface can be seen in the line profile presented in Fig. 2.11. In this particular system there is no CDW until the system is doped by the Na-intercalation. Consequently the level of doping is linked to the strength of the CDW, the numerically differentiated STS measurements in Fig. 2.11 present the LDOS at no doping (A), moderate doping (B), and optimum doping (C). The CDW is slowly revealed as doping reaches optimum, manifesting as the expected depletion of states near the Fermi level. Once again the gaping is incomplete indicating that the CDW phase is still metallic.

However, whilst STM can measure the characteristic wavelength of a CDW, from which the Fermi nesting wavevector may be inferred, STM cannot directly measure the FS and therefore does not directly measure the nesting vector and cannot be used to determine what parts of the FS are nested. Other techniques can be used to

Image redacted for copyright reasons.
Please see the original source or print copy of this thesis.

Figure 2.10: Local probe measurements of the uni-directional stripe CDW in $TbTe_3$. The stripe period propogates in the c-direction marked in the topographic STM image. Below the image is a LDOS plot as recorded by numerically differentiated STS. A subtle depletion of states near to the Fermi level ($V = 0$) caused by a CDW gap is seen. This is easier to see in the $5\times$ expanded plot. Figure source: [77]

Images redacted for copyright reasons.
Please see the original source or print copy of this thesis.

Figure 2.11: Striped CDW phase on Na-intercalated VSe_2. (**a**) A line profile recorded from a topgraphic STM image reveals the sinusoidal influence of the CDW superposed upon the normal atomic corrugation of the lattice. (**b**) Increasing Na intercalation (A through C) fuels the development of the CDW which can be seen by development of the CDW gap. Figures source: [76]

complement STM measurement. ARPES is an effective tool for measuring the FS of a material. In $NbSe_2$ ARPES has been used to successfully measure the nested parts of the FS. Shen *et al.* report that high symmetry points over a broken honeycomb portion of the FS are nested by the appropriate CDW wavevector. They go on to demonstrate that with decreasing temperature these portions of the FS show an increase rate of depletion below T_{CDW} with respect to other parts of the FS, demonstrating that a CDW gap is opening up on the FS at the nested points. [68] Despite this success finding the nesting vector can be extremely difficult, indeed the search was so difficult for the nesting vector in $NbSe_2$ that despite extensive experimental study the nesting vector took three decades to find, and it was even the subject for theories of hidden Fermi surface nesting. [67] It has also been noted that whilst STM is very effective for finding CDW phases at the surface of materials it can often be difficult to replicate this success when performing bulk measurements to find the CDW phase in the rest of the material. [45, 77] However, STM can sometimes reveal information about the propogation of CDWs into sub-surface layers, such as for the chiral CDWs reported by Ishioka *et al.* [78]

2.2.3 Ubiquity of superconductivity and charge density waves

Many 2D layered materials, including the transition-metal dichalcogenides [47, 54, 68, 82, 83], metal-containing organic compounds [46], and cuprate high-temperature superconductors [44, 45, 80], exhibit superconductivity as well as CDWs. This has lead to much speculation among theorists that CDW and stripe phases [74] play a crucial role for superconductivity. [69, 70, 84] In particular even high temperature superconductivity is believed to be linked to the fluctuating stripe phases and the

checkboard patterns found in cuprate superconductors. [44, 80] These are linked to the pseudogap phase which some people ascribe to a CDW state. [45] One of the difficulties in relating the pseudogap to a CDW is the fact that the gapped state persists in part even into the normal phase, however, this has recently been shown to happen even in the widely-accepted CDW and superconducting material $NbSe_2$[85] indicating perhaps that these states are more closely linked than previously thought.

In 1954 *Frölich* suggested that for a 1D system in the absence of damping an incommensurate CDW would inevitably lead to supercurrent. [65, 86] The implication of this claim is that CDWs may, under the correct conditions, lead to superconductivity. Indeed in $NbSe_2$ the superconducting and CDW states are demonstrated to co-exist (see Chapter 4) indicating that either the states, or the conditions (phonons etc.) which mediate them are closely linked. However, this is not always the case, in many systems the two phases are shown to compete (e.g. in S [87]) and suppression of the CDW phase, by pressure or doping, is shown to enhance the superconducting temperature of the material. Competition between Peierls CDWs, SDWs and superconductivity is well-documented, even if a full understanding is not yet evident. [88] However, this competition is also found for high temperature superconductors (e.g. $YBa_2Cu_3O_y$ [89]) indicating that such mechanisms are not unique to conventional phonon-driven superconductors, but are in fact of general importance to all superconductors. Indeed, this continues to be an area of keen interest for theorists in conventional and high temperature superconductivity. [69, 70, 84, 88] Given the ubiquity of these states in 2D materials, and the abundance of superconducting graphitic materials [9, 10], it is perhaps a surprise that prior to the discovery in CaC_6 CDWs had not been found in graphite, graphene or any GIC superconductors.

Chapter 3

Sample-related methods

This chapter presents the sample fabrication techniques for the creation of high purity CaC_6 samples as well as their characterisation and preparation for STM experiments. The precautions taken to minimise contamination from graphite and other impurities and atmospheric exposure are discussed in detail, as are the preparation techniques used for graphite and $NbSe_2$ STM calibration samples. Additionally data concerning the intercalation process and the bulk electronic properties of CaC_6 are presented herein.

3.1 Sample fabrication

Fabrication techniques for CaC_6 and other GICs [9] are covered in great detail in the works of *Emery* [26], *Pruvost* [90] and *Weller* [91] respectively. There are three commonly used intercalation techniques: immersion of the graphitic host in a molten metal, vapour transport, or mediation using a solvent such as ammonia. The most effective intercalation method for the fabrication of CaC_6 is alloy immersion, typically sample purities of greater than 99.9% can be achieved with careful application. Vapour transport techniques are also viable for the creation of CaC_6, with sample purities of up to 60%. The methods, types of graphite, and macroscopic properties of samples made by these two different techniques vary significantly. The techniques used for samples created for experiments reported in this thesis were refined by extensive trial and error to give the best possible sample purity. Each method is described in detail in this chapter.

3.1.1 Fabrication of calcium graphite by Li-Ca alloy technique

CaC_6 can be most readily formed via the Li-Ca alloy technique. [90] This technique involves immersing a graphitic host in a molten alloy of Li and Ca under an inert atmosphere and high temperature. Immersion of graphite in molten Ca does not provide a good Ca uptake resulting in low purity CaC_6. [91] However, by using a Li-Ca alloy the graphite host is first intercalated by the Li atoms and then over the course of the intercalation reaction the Li atoms are slowly substituted by Ca. This process is believe to be facilitated by the Li atoms increasing the interlayer spacing in the graphite host, weakening the van der Waals bonds between the graphene sheets, which then allows Ca atoms to enter the galleries and intercalate the sample. If the reaction is performed under the right conditions of time, temperature and pressure then the substitution provides samples of better than 99.9% phase purity of CaC_6. Whilst the method is simple the technique has been highly refined such that high purity samples can be fabricated with minimum inclusion of Li, alloy or LiC_6 impurities.

First the graphite host is prepared by being outgassed, this is very important as Ca, Li and the GIC itself are all very sensitive to impurities, especially water, oxygen and nitrogen. The graphite is placed inside a reactor tube which is dynamically vacuum pumped using a turbo pump, typically reaching a pressure of $<10^{-6}$ mbar. Once base pressure is reached the graphite is heated to 500^{o}C inside a tube furnace. During heating active pumping continues, this procedure causes adsorbed water, hydrocarbon

and other gaseous or liquid impurities to be expelled from the graphite surface and galleries, as a result the pressure inside the tube temporarily increases. This process continues for approximately 24 hours after which time the pressure inside the tube has returned to the base pressure of the turbo pump indicating that the graphite is fully outgassed.

The graphite is then transferred to an argon atmosphere glovebox slightly above ambient pressure, typically around 1.1 bar, without being exposed to atmosphere (in particular oxygen or water vapour) again. All the remaining steps are performed within an argon atmosphere. The Li-Ca alloy is prepared by placing Li and Ca metal within a reactor tube with a ratio of 3:1 mol of Li to Ca. The reactor tube is sealed and then transferred to a tube furnace heated to 350°C in order to form the alloy. The alloy is left under heating for 24 hours in order to ensure uniform distribution of Li and Ca throughout the metal.

Once the alloy is ready the tube is transferred back to the glovebox before being unsealed, the graphite is then placed underneath the alloy inside the reactor tube. It is important to have an abundance of Ca atoms, for best results rather than having a ratio of 1:6 mol Ca to carbon a ratio greater than to 1:2 mol is used, i.e. a ratio of 4:2 mol of alloy to carbon. The tube is then resealed and transferred back to the furnace and heated to 350°C once again, as the alloy becomes molten the graphite is immersed within the metal and intercalation can begin. The process is quite slow, if the reaction is stopped early then the intercalation yield will be low and Li or Li-based impurities will be extremely prevalent, in order to get maximum yield and purity the tube is heated for seven days at constant temperature.

After seven days the furnace is turned off and the tube is quenched by removing it from the furnace causing it to cool rapidly until it reaches ambient temperature. The tube is then unsealed inside the glovebox. At this stage, if all has gone well, the tube contains a number of high purity CaC_6 samples encased in what remains of the Li-Ca alloy. In order to extract the samples the open tube is heated to a temperature below the intercalation temperature, so as to avoid de-intercalation of the samples, but high enough to make the predominantly Li metal molten, typically around 300°C. At this temperature the alloy is easily removed from the samples by brushing or scrapping them gently, the sample is then ready for characterisation, which is covered in Section 3.2.

The physical condition of the sample depends on the form of graphite used. The STM measurements published in this thesis all pertain to samples created using

HOPG as the graphite host by the alloy immersion technique. However, data presented of scanning electron microscopy (SEM) measurements (Fig. 3.5) are of natural flake-based samples. This technique can also be used to intercalate turbostratic graphite or natural flake graphite with equal success. In general the alloy intercalation process is vigorous and decreases the crystallinity of samples grown by this method, i.e. the average CaC_6 crystal size is typically slightly (same order of magnitude) smaller than the average crystal size of the original graphite host.

3.1.2 Fabrication of calcium graphite by vapour transport technique

CaC_6 can also be made via the vapour transport technique. Samples made by this method have lower intercalation yields than those made using the alloy technique, typically purity is around 60%. However, the vapour transport process is much less vigorous than other techniques and samples maintain the graphite host crystal size. Furthermore, no intermediary metals are used in the fabrication process and as such there are less potential non-graphite impurities in samples created by this method. Unlike the alloy technique not all forms of graphite work well as a host for this process. For HOPG samples Ca uptake is low resulting in samples typically below 10% CaC_6 content (e.g. [91]), natural flake graphite provides the best results with some samples exhibiting up to 60% CaC_6 content. In all cases the non-GIC content of the sample is predominantly non-intercalated graphite (see Section 3.2.3).

The graphite host is outgassed as described in Section 3.1.1. Once inside the argon atmosphere glovebox the graphite is put inside a quartz tube together with Ca metal. It is important to ensure an abundance of Ca metal far in excess of the 6:1 mol ratio of carbon to Ca required to form CaC_6, the reason for this is that during the vapour transport process a significant amount of Ca metal is wasted. The tube is then fitted with a gas fitting valve and transferred to a turbo pump where the tube is evacuated down to a vacuum of approximately 10^{-6} mbar. Great care is taken such that the contents of the quartz tube are never exposed to atmosphere, only argon and then vacuum. Once the tube is evacuated an oxy-acetyline torch is used to seal the tube, trapping the graphite and Ca metal within an ampoule of quartz under vacuum.

Once fully sealed the ampoule is transferred to a furnace and baked at 465°C for two weeks. At this temperature and low pressure the Ca metal vapourises and spreads throughout the ampoule, over time this high temperature Ca vapour is able to enter the galleries in the graphite host resulting in intercalation. If successful the samples

will be intercalated to reasonable high purity as described above. A lot of Ca metal is lost coating the outside of samples and the inside of the quartz ampoule, hence the need for a great abundance of Ca metal for this procedure. The amount of Ca used is limited by the size of the ampoule but typically up to a 2500% excess is used.

After two weeks the samples are transferred back to the argon atmosphere glovebox and the tube is broken open and the samples can then be recovered and mechanically scraped to remove excess Ca metal from the surface. It should be noted that for some time this technique was used in a *two-zone* method [91] whereby the metal and the graphite were placed in two separate parts of the ampoule and intercalation occurs as the metallic vapour passes over the graphite. However, extensive studies at UCL indicate that intercalation uptake is superior when the Ca metal and graphite host are mixed together.

3.2 Sample characterisation

STM is highly localised, and extremely sensitive to impurities, defects and surface effects (this discussed in Chapter 4). Consequently, if one wishes to make a true measurements of the DOS (or LDOS) of CaC_6, and to see the correct physical structure, the sample must be highly pure and properly prepared for STM study. These requirements also apply to other locally sensitive or surface sensitive experiments and many complications can arise from the highly air-sensitive nature of the samples.

Although the fabrication techniques usually provide highly-quality samples, it is important to characterise sample purity for new samples before using them for experiments. In general high quality CaC_6 samples are silver in appearance. When the samples are created by the alloy method gold impurities can sometimes be seen, it has been determined that this is due to the presence of LiC_6 inclusions. Some publications have reported that pure CaC_6 samples are gold in appearance [61] but extensive samples making and characterisation for numerous experiments indicate that samples only appear gold if they contain at least 5% LiC_6 as measured in XRD.

Sample purity can be verified in a number of ways. The approach used for the experiments reported in this thesis is XRD in the 00l direction: the XRD patterns for graphite, CaC_6, LiC_6 and other impurities are all very distinctive and XRD is a bulk technique, as such this allows the purity of a sample to be determined with a high level of precision (Section 3.2.1). The superconducting transition in CaC_6 is also sensitive to impurities or low intercalation yield, a high purity sample should

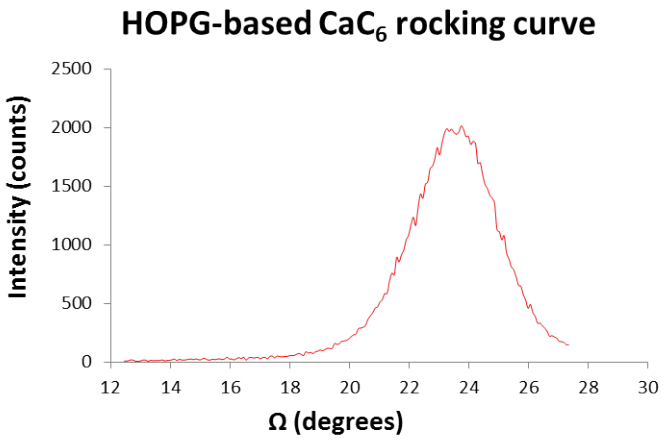

Figure 3.1: XRD scan (Cu X-ray tube) in ϑ of a HOPG-based CaC_6 sample (006) peak reveals good c-axis crystal alignment within the sample.

exhibit a superconducting transition at 11.5 K with a transition width of 0.3 K or less. This property can be easily checked when performing four-contact resistivity measurements or DC magnetisation in a superconducting quantum interference device (SQUID) (Section 3.2.2), both of these techniques are sensitive to the behaviour of electrons (charge and spin carriers respectively) and as such can be used to measure a superconducting transition. Additionally, whilst not used for characterisation of samples for experiments, SEM can provide useful insight into how the intercalation process works and reveal how GIC samples look at the micron-scale (Section 3.2.3).

3.2.1 X-ray diffraction

XRD can be used to determine the crystal structure of a material. For each batch of CaC_6 samples fabricated, typically containing 25 - 30 samples, at least one sample is characterised by XRD in order to verify that the samples are high quality and therefore appropriate for use in other experiments. Samples are loaded onto a platform and covered with kapton (X-ray permeable plastic) tape such that the sample is isolated from the environment around it. Once prepared the sample is transferred from the argon atmosphere glovebox to a Philips Xpert diffractometer, a single-axis X-ray diffractometer with a Cu tube (wavelength 1.54 nm). ϑ scans (also known as a rocking curve), such as the example provided in Fig. 3.1, can be used to estimate the degree of c-axis alignment in layered samples. In this case the full-width-half-maxiumum (FWHM) of the scan gives a c-axis mosaic of 3.2°, this is a low value for GICs indicating relatively good c-axis alignment in HOPG-based samples as expected (see Section 3.1.1).

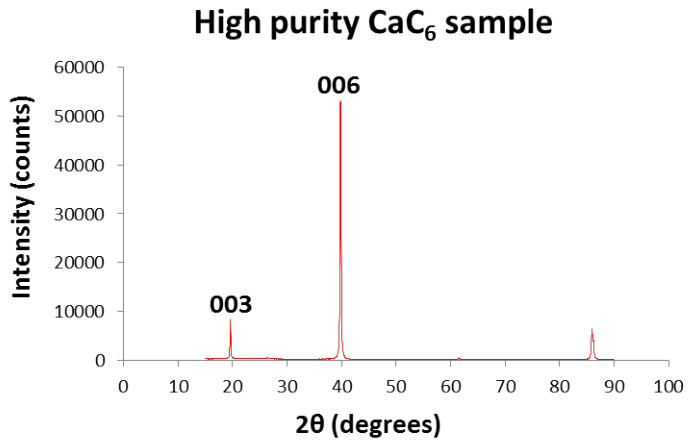

(a)

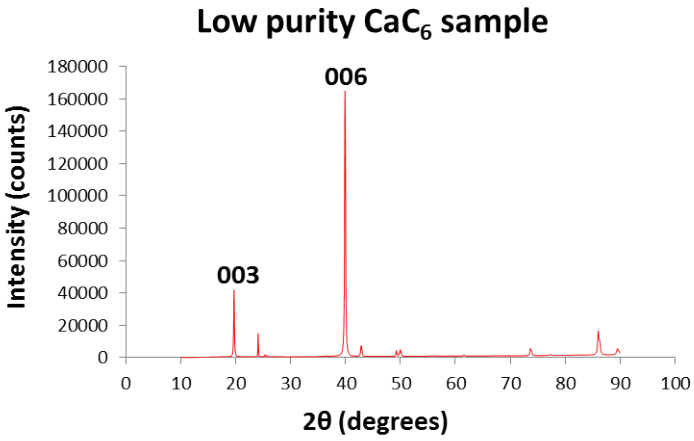

(b)

Figure 3.2: XRD measurements (Cu X-ray tube) in 2ϑ of two CaC_6 samples.(**a**) A high purity HOPG-based CaC_6 sample exhibiting only the expected (003), (006), (009) and (00 12) peaks. (**b**) A low purity HOPG-based CaC_6 sample exhibiting the expected peaks as seen in (a) in addition to peaks corresponding to LiC_6 and graphite impurities.

Fig. 3.2 presents measurements in 2ϑ of two different HOPG-based CaC_6 samples made via the Li-Ca alloy technique. Part (a) displays the XRD pattern for a high-purity sample with an intercalation yield of 99.9% or more, only the CaC_6 (003), (006), (009) and (00 12) peaks are visible corresponding to a (001) spacing of 1.357 nm as expected for a pure sample. [26] Part (b) displays the XRD pattern for a low-purity sample exhibiting both the expected CaC_6 peaks and additional peaks corresponding to common impurities in poorly intercalated CaC_6 samples, these include: LiC_6 (001) and (002) peaks at 24.0° and 48.1° respectively, and graphite (002) and (004) peaks at 26.3° and 54.1° respectively.

This technique allows the purity of samples to be determined quickly and accurately. As a bulk measurement it determines the purity of the sample throughout,

which is very important for STM experiments as the cleaving process used in sample preparation (Section 3.3.2) means that measurements are in fact made on a surface from deep within the original sample. Results presented in this thesis were measured on high purity samples which exhibit no measurable graphite or LiC_6 content (or indeed any other contaminant).

3.2.2 Electronic transport and DC magnetisation

Bulk transport or magnetisation measurements can be employed to discover phase transitions or other phenomena involving charge and spin carriers in a material. In the case of CaC_6 these techniques can be used to reveal the superconducting transition and to search for other interesting behaviour. The sharpness of the superconducting transition can be used as a measure of sample purity by which to judge the validity of other transitions discovered by transport measurements. However, it should be noted that samples from each batch used in transport or magnetisation experiments were also confirmed to be 99.9% pure by XRD.

For resistance measurements CaC_6 samples are prepared, inside an argon atmosphere glovebox, with four contacts in a linear arrangement and placed within a sample holder. Each contact is made from high purity gold wire and fixed to a clean sample surface using conductive silver epoxy. The sample and holder are transferred to an Oxford Maglab (low temperature magnet and helium flow cryostat) using a helium-filled glovebag to avoid exposure to atmosphere. Once inside the instrument the sample area is evacuated and then filled with inert helium exchange gas. An example of a four-contact resistance measurement made on a high quality high purity CaC_6 sample is provided in Fig. 3.3. The sample exhibits metallic behaviour as expected, as well as a sharp superconducting transition at 11.5 K with a width of less than 0.3 K which demonstrates the sample is clean and has a high purity. An anomalous transition can be seen at approximately 250 K, the upper inset shows the derivative (gradient) of resistance which clearly highlights a change in gradient at approximately 250 K. This transition has not been previously reported and its precise nature is not clear, however, it is reminiscent of CDW transition as seen in $NbSe_2$ and other materials. [65, 72, 92] A study of 13 different CaC_6 samples revealed that five samples exhibited a subtle transition at $T = 250 \pm 20\,\mathrm{K}$.

A complementary DC magnetisation measurement made using a SQUID at a magnetic field of 1 T is presented in Fig. 3.4. For measurements of this type CaC_6 samples are loaded into a sample straw inside the argon glovebox and then transferred to the

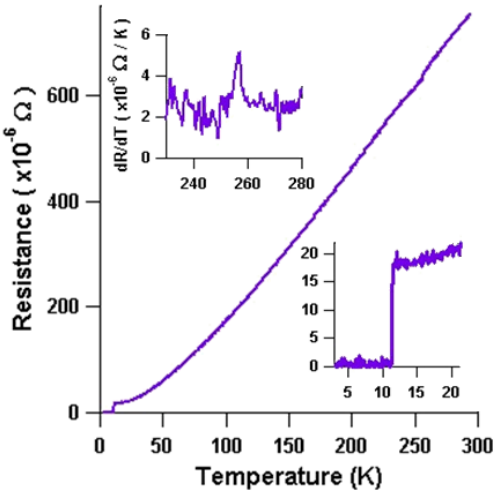

Figure 3.3: Four-contact resistance measurements of a high purity CaC_6 sample. Lower inset: A sharp superconducting transition at 11.5 K with $\Delta T < 0.3$ K. Upper inset: Derivative $\frac{dR}{dT}$ highlights small unexpected transition at approximately 250 K. Both insets are plotted in the same units as the main figure unless otherwise indicated.

SQUID inside a small bubble of argon within the straw. Inside the SQUID the sample chamber is evacuated using a turbo pump down to approximately 10^{-7} mbar. Fig. 3.4 is a typical example of measurements performed on three different CaC_6 samples. In all cases samples were zero field cooled to the instrument's base temperature of 4.2 K, the superconducting transition was then measured at a magnetic field of 2 Oe, an example of which is included inset in the figure. The samples were then warmed from base to ambient temperature at a field of 1 T and then cooled from ambient temperature back to base. In 100% of cases an anomalous transition closely matching that which is seen in resistance was observed at $T = 250 \pm 10\,\mathrm{K}$ characterised by a dramatic drop in moment when warming. However, it should be noted that the transition was never reproduced on cooling, the reason for which is not clear.

Whilst the transition was not always reproducible in resistance the fact that it was seen five times and was also measured at approximately the same temperature in magnetisation in three of three samples indicates that the transition is a real property of the sample. All samples used were high purity and exhibit very sharp superconducting temperatures, indicating good intercalation yield, at the correct temperature of 11.5 K, indicating neglible impurities. In resistance the transition is clearly metal-metal and the sample is in fact more metallic below the transition than above. This is atypical for a phenomenon such as a CDW but it is not unprecedented, $NbSe_2$, one of the most widely studied CDW systems [72, 82, 92], displays a similar phenomenon. Furthermore, analogous effects have been seen in the high-temperature superconduct-

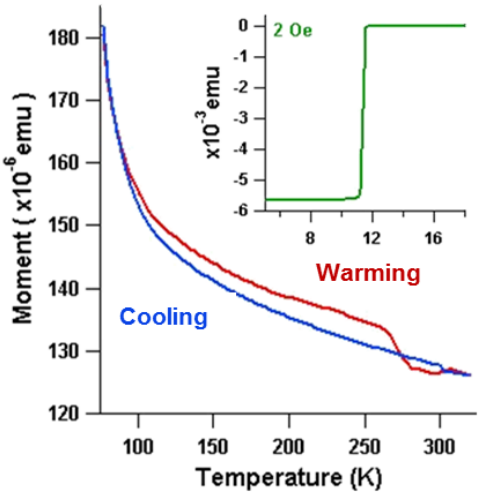

Figure 3.4: DC magnetisation measurement of a high purity CaC_6 sample at 1 T. An anomalous transition resulting in a dramatic decrease in moment is seen on warming, but not cooling, at approximately 250 K. Inset: A sharp superconducting transition measured at 11.5 K with $\Delta T < 0.3$ K using a 2 Oe magnetic field. Inset is plotted in the same units as the main figure.

ing cuprates around the pseudogap temperature [93], which some ascribe to a CDW transition. [45] One proposed mechanism is that the loss of FS density below T_{CDW} can sometimes eliminate so-called cold spots in the FS which, it is postulated, could increase conductivity. [82] Likewise an increased moment below the transition temperature indicates an increase in the density of available spin carriers which is consistent with an increase in available electrons as indicated by the resistance data.

3.2.3 Scanning electron microscopy

SEM is not used for measuring sample purity, but it can be used to observe the intercalation process and the general physical condition of GIC samples. Fig. 3.5 presents a series of SEM images of a CaC_6 sample grown by the vapour transport method. This sample was fabricated using a natural graphite flake host as described in Section 3.1.2 and is known, by XRD measurement, to have an intercalation yield of approximately 40%. The sample was transferred from the argon atmosphere glovebox to the SEM in a small bag of argon gas and then placed in the SEM airlock. This required momentary exposure to atmosphere before the airlock was evacuated and the sample observed under vacuum of approximately 10^{-6} mbar.

Fig. 3.5a reveals the overall appearance of the sample. As a result of exposure to atmosphere some oxide has formed, particularly around the edges of the sample, this is visible as a white-coloured fur on various parts of the sample surface. A great deal of the sample is covered with metal, which is a non-uniform bright grey in appearance.

However, in the centre of the sample a small area of dark surface is visible, this is unintercalated graphite, and the uniform silver puddling which can be seen on and around this is CaC_6 GIC. In a fully intercalated sample the surface appears a uniform silver colour, but in this partially intercalated sample puddles of GIC material can be seen on the graphite (Fig. 3.5b). This demonstrates clearly that intercalation is not a case of slowly distributing Ca atoms throughout the sample until saturation, but rather that crystals of CaC_6 form at the edges or defects of the graphite host and then these crystals grow as the intercalation process progresses. Fig. 3.5c also reveals that these GIC crystals do not necessarily meet in a uniform manner, grain boundaries in the CaC_6 formation are clearly present, indicating that the intercalation process increases the polycrystallinity of the graphite host. Note also that despite the sample surface appearing somewhat flat for extended areas of 1 - 2 μm there are a number of random pieces of surface junk, the nature of which is not clear but could be excess metal, oxide or graphite dust. Finally, Fig. 3.5d demonstrates that each GIC puddle also has a finite depth, in this case a FIB was used to mill away a trench in a number of the CaC_6 crystals, from the cross sectional view it is clear that the crystals have a depth of order 100 nm.

The information revealed by SEM is vital for understanding how to prepare a CaC_6 sample for STM study. It is clear that the sample surface is too rough and unclean for the stringent requirements of STM study (discussed in great detail in Chapter 4). The presence of oxides, graphite dust and other debris would be detrimental to the stability of the tunnelling junction. Furthermore, the surface is not a single uniform crystal but a polycrystalline collection of CaC_6 puddles. If sample purity is not 100% one would expect to observe areas of sample surface exhibiting 100% pure CaC_6 and other areas exhibiting unintercalated graphite, rather than a uniform districtuion of low yield GIC. Sample preparation of CaC_6 is covered in Section 3.3.2.

3.3 Sample preparation for STM

It is important that samples prepared for STM meet the stringent requirements for stable imaging and spectroscopy, namely that there are flat surfaces which are free of contamination positioned such that the STM is able to approach and scan them. When working with layered materials the most effective method of preparing such surfaces is through sample cleaving. This means applying mechanical force to the sample such that layers of the surface are peeled away revealing a new, clean and flat

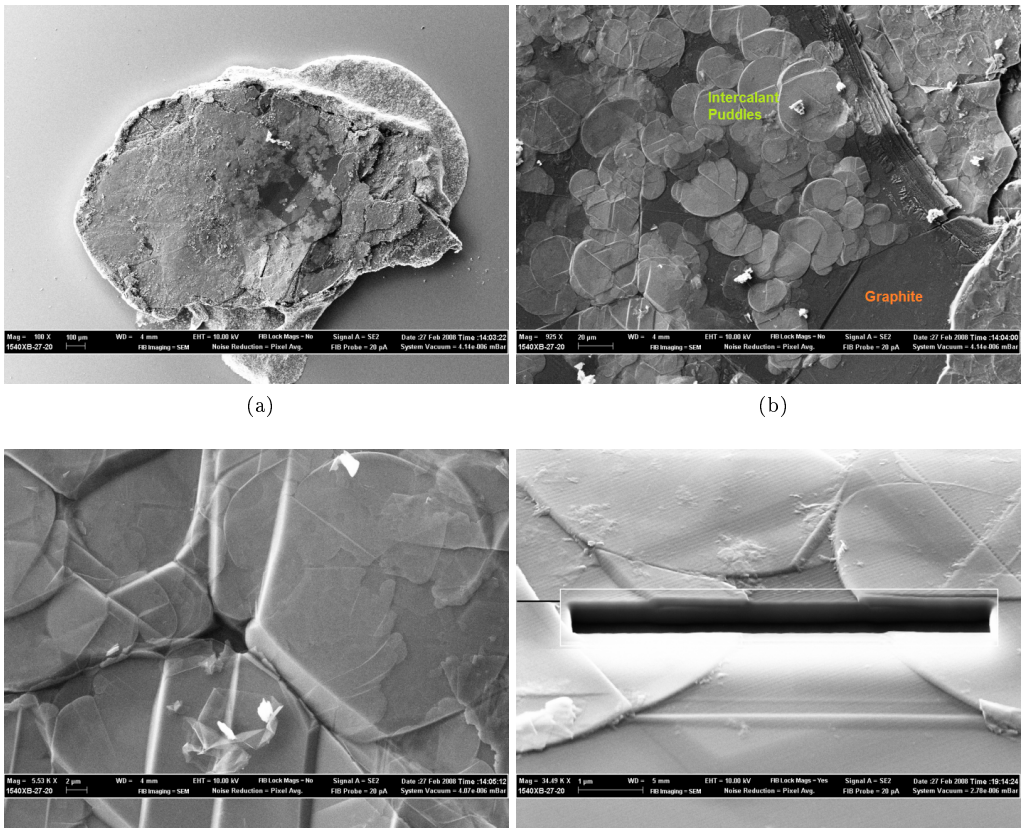

(a) (b)

(c) (d)

Figure 3.5: SEM images of a natural flake-based CaC_6 sample partially intercalated by the vapour transport method. (**a**) The entire flake can be seen spanning approximately 2 mm in width. Brighter areas indicate greater electron density. Rough areas are Ca metal and oxide from the vapour transport process (**b**) Focus on a 200 μm wide area of partially intercalated graphite (as seen in the centre of the first image) surrounded by areas which are covered with metal or oxide. (**c**) Focus on puddles of CaC_6 on the sample surface, entire image is approximately 30 μm wide. (**d**) A segment of the sample surface is removed by FIB milling to reveal that CaC_6 puddles have a finite depth.

surface from within the sample. The exact method varies from sample to sample, the details for the preparation of the $NbSe_2$ and graphite calibration samples, the data for which is presented in Chapter 4, and for the CaC_6 samples, the data for which is presented in Chapter 5, are discussed in this section.

3.3.1 Preparations of graphite and niobium diselenide

Graphite and $NbSe_2$ are both hexagonal quasi-2D layered materials with weak intralayer forces, consequently both materials cleave readily along their ab-planes. Since both samples are inert in atmosphere the cleaving method for both samples is identical. The samples are first fixed to a Ti or Mo STM sample plate using a conducting silver-based epoxy, this serves as a sample holder for transporting and storing samples inside the STM itself. The silver epoxy paste cures in 5 minutes at 300°C, at this temperature there are no adverse effects to the samples. Furthermore, the plate provides a conducting pathway between the sample and the STM ground via the silver epoxy, the technical details of the STMs and their operation are covered in Chapter 4. Samples are orientated such that the ab-plane lies parallel to the sample plate, and hence the same plane will lie perpendicular to the STM tip inside the instrument allowing the user to study the samples in-plane.

To complete the sample preparation the sample is cleaved using sticky tape (e.g. 3M's white "Scotch tape"). The tape is applied across the surface of the sample ensuring a good adhesive contact by pressing across the sample with the back of a scalpel blade. Once prepared the tape is removed in a slow peeling motion, if successful this results in a number of sample layers also being peeled away with the tape to reveal a flat, clean and reflective sample surface. If unsuccessful, for example because of partial layering or debris left on the surface, the process can be repeated numerous times until the surface has a satisfactorily flat and smooth appearance. Graphite cleaves very easily to give a shiny black-silver surface. Although slightly more difficult to cleave perfectly, when successful the $NbSe_2$ sample surface has a black, obsidian-like appearance.

Once cleaved the samples can be loaded into the STM for study. However, whilst both graphite and $NbSe_2$ are inert in air there is a tendency for monolayers of water to form on the surface of samples, at low temperature this can form ice and interfere with spectroscopy of the surface. To avoid this problem samples are heated to 120°C inside the STM preparation chamber in order to remove any water or other condensates. The temperature of this outgassing procedure is kept relatively low to avoid affecting

the conductivity of the silver epoxy. The preparation chamber operates at UHV (see Section 4.3.1 for more details), the pressure rises slightly during the procedure, heating continues until the pressure drops back to base, typically this takes between four and six hours. Once outgassed the samples are ready for study, if successful the sample surface should be flat and clean.

3.3.2 Preparation of calcium graphite

CaC_6 is physically more 3D in nature than graphite, specifically the intralayer bonds are significantly stronger due to the presence of Ca atoms between the graphene sheets, and as such CaC_6 is more difficult to cleave mechanically. To overcome this problem a cleaving post method is used as reported by Bergeal *et al.* [3] The CaC_6 sample is fixed to a sample plate as described in Section 3.3.1. The exposed sample surface is then fixed to a stainless steel rod, known as a cleaving post, using the same silver epoxy. For CaC_6 samples the silver epoxy curing temperature of 300°C could cause some de-intercalation, therefore if possible the samples are cured at ambient temperature for three full days inside a high purity argon atmosphere glovebox. If time is short the epoxy can instead be cured at 120°C for approximately half an hour inside the glovebox using a hot plate. Once cured the sample should be encased completely in silver epoxy with a fault line running through the epoxy where the cured epoxy on the sample plate meets the epoxy holding the screw in place. This is such that when a lateral force is applied to the screw the sample is cleaved forcefully across the weak point in the epoxy revealing a flat, clean sample surface from deep within the original sample.

Samples are prepared inside the argon atmosphere glovebox to avoid contamination from exposure to oxygen, water vapour or nitrogen. Once prepared samples are transferred in a small bag of argon gas to the STM and loaded into the STM airlock. This requires temporary exposure of the sample plate to atmosphere, however, the silver epoxy should fully encase the sample and prevent exposure of the CaC_6. Once the sample is inside the airlock it is pumped down to a vacuum of 10^{-8} mbar or better before being transferred into the STM chamber. The cleaving is performed *in situ* using mechanical force applied to the side of the cleaving post using a manually operated manipulator. In most cases some or all of the sample surface is sufficiently well cleaved for study. Once the sample has been cleaved study begins immediately so as to avoid any problems with deterioration of the surface. It should be noted that this is only a precaution, the pressure in the STM chamber is typically close to 10^{-11} mbar

so the sample is exposed to negligible amounts of contaminants or air.

In some cases samples were heated at approximately 120°C for four to six hours after cleaving. The aim of this was to remove loosely-bound intercalant material from the surface, without causing de-intercalation of the sample, in order to guarantee the surface terminated in a graphene sheet. This proved a successful measure for protecting the STM tip from contamination-related tip condition changes. Furthermore, the propensity for discovering the expected surface type (Section 5.4) was increased dramatically by this process at the expense of non-AR surface types (Section 5.2), but the occurence rates of other surface types were unaffected.

Chapter 4

Scanning tunnelling microscopy

This chapter concerns the methods and theory specific to STM and the various imaging and spectroscopic techniques which can be employed to study material surfaces. This includes a brief overview of tunnelling theory, application of tunnelling principles to STM imaging and spectroscopy, advanced spectroscopic imaging techniques, analysis of STM imaging and spectroscopic data, and instrumental details of the STMs used and STM tip preparation procedures. In addition some example data and data analysis is presented for $NbSe_2$ and raw graphite from the author's own calibration and testing data.

4.1 Introduction to STM

The STM is a powerful tool for studying the surfaces of materials. The instrument works by bringing a sharp local probe into close proximity to a flat sample surface, a potential difference is introduced between the probe and the sample resulting in a small tunnelling current between the two via the *tunnelling junction* (a vacuum gap). Classically the flow of current without a conductance path is not possible, however, according to the wave mechanical treatment of electrons introduced by quantum mechanics, electrons with sufficient kinetic energy can pass through a potential barrier by the tunnelling effect. [94] Even before the advent of STM tunnelling has been used as an excellent tool for studying the DOS of many materials, including measurement of phenomena such as superconducting gaps. [95, 96] In the case of STM the potential barrier is the vacuum gap between the tip and the sample and tunnelling occurs when the potential difference, V, across this junction exceeds the difference in work function, ϕ, of the two materials. By utilising the exponential dependence of the tunnelling current, I, with probe-sample separation, z, voltage, V, and probe position, $\overrightarrow{r} = (x, y)$, highly detailed real space imaging is possible. The first successful demonstration of vacuum tunnelling using an STM was presented in 1982 by *G. Binnig, G. Rohrer, Ch. Gerber* and *E. Weibel*. [97] This triumph was shortly followed by successful atomic resolution imaging of metal surfaces [98], the 7×7 reconstruction of the Si(111) surface [99, 100], and the corrugation of graphite. [14] For their work on the STM *Binnig* and *Rohrer* shared the Nobel Prize in Physics in 1986.

4.1.1 Tunnelling theory

Tunnelling is the mechanism by which electrons pass through a potential barrier, classically this is forbidden but in quantum mechanics the wave-like treatment of electrons allows for transmission across such a gap, this is best modelled using the time-dependent perturbation theory. In the case of the STM we have a tunnelling junction consisting of a metal tip and a metallic or semi-conducting sample separated by a vacuum gap. The tip is extremely sharp so as to probe the sample surface with atom-scale spatial resolution, consequently the junction can be treated as a 1D problem. Consider an electron with energy E in the presence of a potential barrier $U(z)$ where z is the distance from the tip surface. The electron wavefunction $\psi(z)$ can be found by solving Schrödinger's equation:

$$-\frac{\hbar^2}{2m}\frac{\partial^2\psi(z)}{\partial z^2} + U(z)\psi(z) = E\psi(z) \tag{4.1}$$

For a square barrier where $\hbar = \frac{h}{2\pi}$ is the reduced Planck's constant, m is the electron's mass and $z = 0$ is defined as the position of the tip surface. Outside the barrier, $E > U(z)$, when the electron is within the conducting tip or sample, the solution is that of a propogating wave:

$$\psi(z) = \psi(0)e^{\pm iKz} \tag{4.2}$$

$$K = \frac{\sqrt{2m(E - U(z))}}{\hbar} \tag{4.3}$$

Inside the barrier, $E < U(z)$, when the electron is within the vacuum gap, the solution is that of a decaying wave:

$$\psi(z) = \psi(0)e^{\pm kz} \tag{4.4}$$

$$k = \frac{\sqrt{2m(U(z) - E)}}{\hbar} \tag{4.5}$$

There are two solutions; a wave decaying in the positive z direction (tip to sample) with decay constant $-k$ and a wave decaying in the negative$-z$ direction (sample to tip) with decay constant k. For now the formulation will follow that of the transmitted wave, tip to sample tunnelling, though it is important to note that sample to tip tunnelling is also possible. In order for tunnelling to occur the wavefunctions of the tip and sample must overlap in such a way that when a small potential difference, V, is applied across the barrier the probability of finding an electron within or on the other side of the barrier, P, is greater than zero. [101] For sample position D the probability of overlap is expressed thusly:

$$P \propto \left|\psi(0)\right|^2 e^{-2kD} \tag{4.6}$$

For very a small potential difference only states near the Fermi level $E_F \pm eV$ are excited, where E_F is the Fermi energy and e is the charge of an electron, note that in this case eV is the product of the electron charge and voltage, not the unit of energy eV. Only excited electrons can cross the potential barrier, consequently only electrons near the Fermi level can tunnel between the tip and sample. Furthermore, for small V the energy required to excite an electron for tunnelling is approximately equal to the work function, ϕ, which is defined as the minimum energy required to excite an

electron from the Fermi level to the vacuum level:

$$U(z) - E \simeq \phi \implies k = \frac{\sqrt{2m\phi}}{\hbar} \tag{4.7}$$

For simplicity it is assumed that the Fermi energy and work function are each respectively the same for both the tip and sample and that $\phi \gg eV$. This is certainly the case for most materials used in STM where $\phi \approx 5$ eV, e.g. Tungsten, a commonly used material for STM tips, has a work function of 4.8 eV. In the STM the sample is at an effective bias of V with respect to the tip, such that the Fermi level of the sample is lowered by eV, the precise configurations for the STMs used are discussed in section 4.3.1. Recall that thus far the tunnelling barrier has been assumed to be a square barrier, it is in fact tilted with the height of the barrier lowered by eV at the sample side, however, for STM measurements $eV \ll \phi$ therefore treatment as a square barrier is a good approximation. Sufficiently positive V results in tunnelling from the tip to the sample, negative V results in tunnelling from the sample to the tip. Tunnelling also requires that in order for an electron of given energy to cross the barrier there must also be an unoccupied state of the same energy on the other side of the barrier. Consequently tunnelling current will be dependent on the LDOS of the tip and sample. For example, the tunnelling current when tunnelling from the tip to the sample is dependent on both the number of electrons near to the Fermi level in the tip and the number of unoccupied states with the corresponding energies in the sample. When tunnelling from the sample to the tip the reverse is true; current is dependent on the number of electrons near to the Fermi level in the sample and the number of unoccupied states with corresponding energies in the tip. In short, the more states available near the Fermi level the greater the tunnelling current:

$$I \propto \sum_{E_F - eV}^{E_F} \left|\psi(0)\right|^2 e^{-2kD} \tag{4.8}$$

This expresses the tunnelling current as a probability density; the number of available states satisfying equation 4.6 within the energy interval $E_F - eV$ to E_F per unit volume. It is more desirable to express current as a function of LDOS. For a small interval in energy, ε, near the Fermi level the LDOS of the sample, ρ_s, is expressed as follows:

$$\rho_s(z, E) = \frac{1}{\varepsilon} \sum_{E-\varepsilon}^{E} \left|\psi(z)\right|^2 \tag{4.9}$$

The current can then be expressed as a function of the states available near the

Fermi level at the sample surface:

$$I \propto V\rho_s(0, E_F)e^{-2kD} \tag{4.10}$$

Solving equation 4.7 for $\phi \approx 5$ eV yields $k \approx 11.4$ nm^{-1}therefore, according to equation 4.10, the current changes by a factor of 9.78 for every 0.1 nm change in tip-sample distance. This allows for an extremely high level of detail when measuring the topography of the sample surface as small variations in the tip-sample distance have a dramatic effect on the tunnelling current. [101] Indeed the greater ϕ the higher the level of precision for measuring changes in I or D. Necessarily the current must be the same on either side of the barrier, therefore the following expression is also true:

$$I \propto V\rho_s(D, E_F) \tag{4.11}$$

For a quantum system the transition rate, T, between an initial energy eigenstate $\left|i\right\rangle$ and a final energy eigenstate $\left|f\right\rangle$ due to perturbation is determined by Fermi's golden rule:

$$T_{i\longrightarrow f} = \frac{2\pi}{\hbar}\left|\left\langle f\right|H^{'}\left|i\right\rangle\right|^2\rho_f \tag{4.12}$$

Where $H'$is the perturbing Hamiltonian and ρ_f is the final density of states. This can be applied to STM by treating the wavefunction at the tip, ψ, and at the sample, χ, independently. [102] The rate of tunnelling, ω, can be expressed thusly:

$$\omega = \frac{2\pi}{\hbar}\left|\left\langle \chi\right|H^{'}\left|\psi\right\rangle\right|^2\rho_s\delta(E_\psi - E_\chi) = \frac{2\pi}{\hbar}\left|M\right|^2\rho_s\delta(E_\psi - E_\chi) \tag{4.13}$$

$$M = \frac{2\pi}{\hbar}\int_S(\chi^*\frac{\partial\psi}{\partial z} - \psi\frac{\partial\chi^*}{\partial z})\mathrm{d}S \tag{4.14}$$

Where $M = \left\langle \chi\right|H^{'}\left|\psi\right\rangle$ is the tunnelling matrix which is the overlap of the wavefunctions of the tip and sample, each of which decays exponentially within the tunnelling barrier. The full expression for the tunnelling matrix integrated over all states, S, is expressed in equation 4.14. However, in 1961 *J. Bardeen* showed that for a realistic set of assumptions and small energy differences between the states on either side of the barrier, M can be assumed to be a constant and independent of energy. [102] The Dirac function, $\delta(E_\psi - E_\chi)$, represents the restriction that tunnelling may only occur between states of approximately the same energy as stipulated earlier, furthermore this term satisfies the requirement that M is constant only for small energy differences. The transfer rate can be used to formulate current given that the charge

carriers are electrons with charge e then it is expected that $I \simeq -2e\omega$ where the factor of 2 is due to spin degeneracy. At this stage it is important to recall that tunnelling is possible from tip to sample and vice versa as per the two solutions in equation 4.4, consequently we have the following two equations for tunnelling current:

$$I_{tip\rightarrow sample} = -\frac{4\pi e}{\hbar}\left|M\right|^2 \rho_t(\varepsilon + E_F) f(\varepsilon + E_F)\rho_s(\varepsilon + E_F - eV)[1 - f(\varepsilon + E_F - eV)] \tag{4.15}$$

$$I_{sample\rightarrow tip} = -\frac{4\pi e}{\hbar}\left|M\right|^2 \rho_s(\varepsilon + E_F - eV) f(\varepsilon + E_F - eV)\rho_t(\varepsilon + E_F)[1 - f(\varepsilon + E_F)] \tag{4.16}$$

Where ρ_t is the tip density of states and the probabilities of finding occupied and unoccupied states on the appropriate side of the tunnelling barrier have been restated in terms of the Fermi function, $f(E)$, which is defined as the probability that an electronic energy state of energy E will be occupied at temperature T:

$$f(E) = \frac{1}{e^{(E-E_F)/k_B T} + 1} \tag{4.17}$$

Where k_B is the Boltzmann constant. Therefore, equation 4.15, which expresses the tunnelling current from the tip to the sample, can be seen as a function of electrons available in the tip, $\rho_t(\varepsilon + E_F) f(\varepsilon + E_F)$, and unoccupied states of the corresponding energy available in the sample, $\rho_s(\varepsilon + E_F - eV)[1 - f(\varepsilon + E_F - eV)]$, for tunnelling. Conversely, equation 4.16, which expresses the tunnelling current from the sample to the tip, is seen to be a function of electrons available in the sample, $\rho_s(\varepsilon + E_F - eV) f(\varepsilon + E_F - eV)$, and unoccupied states of the corresponding energy available in the tip, $\rho_t(\varepsilon + E_F)[1 - f(\varepsilon + E_F)]$. The total tunnelling current, I, is found by summing tunnelling in both directions over all states:

$$\begin{aligned} I \;=\; & -\frac{4\pi e}{\hbar}\int_{-\infty}^{\infty}\left|M\right|^2 \rho_s(\varepsilon + E_F - eV)\rho_t(\varepsilon + E_F) \\ & \times\{f(\varepsilon + E_F - eV)[1 - f(\varepsilon + E_F)] - [1 - f(\varepsilon + E_F - eV)]f(\varepsilon + E_F)\}\mathrm{d}\varepsilon \end{aligned} \tag{4.18}$$

This equation expresses the current as a function of the density of states for both tip and sample, and also of the probabilities of filled and empty states of corresponding energy on either side of the barrier within an interval , around the Fermi energy, satisfying all the criteria stipulated earlier. This formulation is very similar to that which is presented in the *Tersoff-Hamann* theory of STM.[103, 104] All data presented in this thesis were recorded at 78 K. At such a low temperature the value $k_B T \approx$

6.7 meV is very small such that $k_BT \ll \varepsilon + E_F$, $\varepsilon + E_F - eV$, consequently further simplification is possible:

$$f(\varepsilon + E_F - eV) - f(\varepsilon + E_F) \simeq \begin{cases} 0 & \varepsilon + E_F < 0 \\ 1 & 0 < \varepsilon + E_F < eV \\ 0 & \varepsilon + E_F > eV \end{cases} \tag{4.19}$$

This means tunnelling only occurs close to the Fermi level in the interval $0 < \varepsilon + E_F < eV$, this is consistent with the relation derived earlier in equation 4.8, consequently the tunnelling current can be expressed as an integral over states in this finite range:

$$I = -\frac{4\pi e}{\hbar} \int_0^{eV} \left|M\right|^2 \rho_s(\varepsilon + E_F - eV)\rho_t(\varepsilon + E_F)\mathrm{d}\varepsilon \tag{4.20}$$

To within an error of $k_BT \approx 6.7$ meV in energy. The dependence of the tunnelling current on the tip's DOS highlights the importance of selecting an appropriate material for the tip. When studying a sample it is desirable to measure features in the DOS of the sample surface, in order to be able to deconvolute the contribution of the sample DOS from that of the tip, when measuring the tunnelling current, one must ensure the tip has a featureless DOS (i.e. behaves as a perfect metal with a constant DOS independent of energy) within a small energy window $0 < \varepsilon + E_F < eV$ near the Fermi surface. Further discussion of this is provided in section 4.3.2. For simplicity the featureless DOS of the tip within this range shall be denoted $\rho_t(0)$. Also recall that for a small energy difference between two states on either side of a potential barrier the tunnelling matrix M is approximately constant and has no dependence on energy:

$$I = -\frac{4\pi e}{\hbar}\left|M\right|^2 \rho_t(0) \int_0^{eV} \rho_s(\varepsilon + E_F - eV)\mathrm{d}\varepsilon \tag{4.21}$$

For a given barrier width D, as defined earlier, M can be found by solving equation 4.14. The solution given by employing the semi-classical Wentzel-Kramers-Brillouin (WKB) approximation is as follows:

$$\left|M\right|^2 = e^{-2\int_0^D k dz} = e^{-2kD} \tag{4.22}$$

Where k is the same as in equation 4.7. This is consistent with the relation derived earlier in equation 4.10. Therefore, the final approximation for I as a function of V

and D is given in equation 4.23:

$$I = -\frac{4\pi e}{\hbar}\rho_t(0)e^{-2kD}\int_0^{eV}\rho_s(\varepsilon + E_F - eV)\mathrm{d}\varepsilon \tag{4.23}$$

4.1.2 STM imaging

The STM is capable of a number of measurement modes, broadly speaking these include imaging techniques, covered in this section, and spectroscopic techniques, covered in section 4.2. When imaging the tip is rastered across the sample surface by means of a piezo tube scanner which can finely control the height of the tip, z, with respect to the sample (which is fixed) and scan the tip in two orthogonal directions, x and y, within the plane of the sample surface. The piezo tube consists of piezo electric ceramic drives which work by expansion or contraction of quadrants of the tube when voltage is applied such that the tip is moved in the $\pm x$ or $\pm y$ direction with an extremely high level of precision (typically better than 0.01 nm). The STM exploits the fact that the tunnelling current is highly-dependent on the DOS and tip-sample separation in order to gather information about the structure and LDOS of the sample surface. These two facts are mathematically framed in equation 4.23. However, as the STM tip is moved between locations close to the sample surface both the local density of states and topographic structure of the surface will vary locally, therefore it is prudent to express both of these properties as functions of the tip location defined by the real-space position vector $\overrightarrow{r} = r(x, y)$. Note that the cross-over point between point contact tunnelling and vacuum tunnelling is considered to be when the separation of the two conductors is in the range 0.5 - 0.8 nm.[105] In otherwords the physics outlined in section 4.1.1 applies only when the tip-sample separation falls within this range. However, it is notoriously difficult to determine the true absolute value of the tip-sample separation due to the substantial changes in current even for small changes even of the order of a fraction of an atom, but relative values of z between different surface locations can be measured. Changes in x, y, z are recorded by the STM in the form of voltages applied to the piezo tube and these are then expressed as distances by converting using the known calibration for the piezo crystals at a given temperature. A revised version of equation 4.23 to allow for these realities of STM is presented in equation 4.24:

$$I(\overrightarrow{r}, z, V) \approx I_0 e^{-2kz}\int_0^{eV}\rho_s(\overrightarrow{r}, \varepsilon + E_F - eV)\mathrm{d}\varepsilon \tag{4.24}$$

Where $I_0 = -\frac{4\pi e}{\hbar}\rho_t(0)e^{-2kz_0}$ is a constant, the precise value of which cannot always be determined but since most measurements involve comparing changes in height, current or LDOS it can be worked around. In this case z_0 represents the constant offset between the arbitrary zero point chosen for z and the unknown absolute value of the tip-sample separation $D = z + z_0$. There are two primary forms of imaging, constant-height (current) imaging and constant-current (topographic) imaging, in both cases the sample bias is held at a constant set point value $V = V_{Set}$. In current imaging mode the STM records changes in the current as the tip rasters the surface at a fixed value of z, this generates a 3D data set which is plotted as the image $I(\overrightarrow{r}, V)$. The current recorded is a function of both variations in the height of the sample surface and the LDOS of the sample at each $\overrightarrow{r}$ as expressed in equation 4.24. There are a number of drawbacks to this imaging technique; it is difficult to determine and regulate the constant set point for z and if the surface topography varies by a greater amount than the initial tip-sample separation the tip could contact the surface effectively ruining probe. Topographic imaging mode avoids these problems by regulating the tip-sample distance by means of a feedback loop; the feedback loop adjusts the height of the tip such that for a given sample bias $V = V_{Set}$ the current is maintained at a set point $I = I_{Set}$. By holding the tip at a fixed height with respect to the sample surface the probability of tip drift or the tip coming into contact with the sample is minimised. As the tip rasters the surface changes in the absolute tip height are recorded by the STM, the data set is plotted as an image $z(\overrightarrow{r}, V)$. Note that the when the tip rasters the surface, in either imaging mode, it scans an entire line horizontally before stepping up vertically, therefore the x-direction is sometimes referred to as the *fast scan* direction and the y-direction is referred to as the *slow scan* direction, this can important for the interpretation of noise or drift in images. An example a topographic STM image is provided in Fig. 4.1, in this example the surface displayed is the Si(111) surface for which the famous 7×7 reconstruction has been recorded by topographic STM imaging. Each Si atom is imaged in real space with atomic resolution. The tip height quoted in the colour bar is the relative tip height recorded by the piezo crystal as described in this section rather than a true absolute height of the surface.

The exponential dependence of tunnelling current on tip-sample separation means that the feedback loop is extremely reliable, even a tiny variation in separation would result in a dramatic change in current. From equation 4.24: for a fixed value of I it can be seen that z will depend upon not only the change in surface topography but

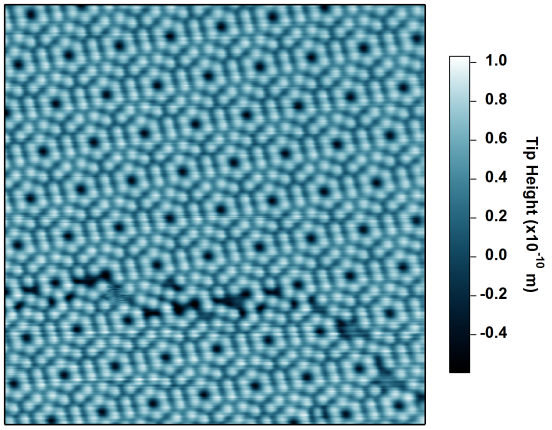

Figure 4.1: The famous Si(111) 7×7 reconstruction as imaged in real space by topographic STM imaging. The image measures 20 nm $\times$ 20 nm in plane. A phase boundary between two silicon crystals is visible running approximately horizontal across the lower half of the image.

also the change in LDOS $\rho_s(\overrightarrow{r}, \varepsilon + E_F - eV)$ at position $\overrightarrow{r}$. The topographic image $z(\overrightarrow{r}, V)$ traces a contour of constant charge density in the energy interval $0 < \varepsilon < eV$ which is a convolution of both the physical structure of the surface and the LDOS at each surface position. Understanding this fact is key to interpretation of topographic STM images, particularly when the surface structure and LDOS are not uniform across the scan area.

4.1.3 Fourier transform STM

Real space analysis (topographic STM images) can yield a lot of important information about a surface, however often the most interesting structures found on the nano-scale are highly periodic. FT-STM is a powerful tool for studying periodic structures such as atomic lattices, superlattices, charge ordering, CDWs and other forms of super modulation. The principle behind this technique is extremely simple; a topographic STM image can be subjected to a 2D FT where the real space image $z(\overrightarrow{r}, V)$ is used to calculate a discrete Fourier transform (dFT) which in this case is the reciprocal space image $Z(\overrightarrow{k}, V)$ where $\overrightarrow{k} = (k_x, k_y) = \frac{1}{\overrightarrow{r}}$ is the reciprocal space position vector. Typically FT-STM data is plotted in units of $k_x = \frac{1}{x}$ and $k_y = \frac{1}{y}$. A dFT is mathematically expressed in equation 4.25:

$$Z_m = \sum_{n=0}^{N-1} z_n e^{-\frac{2\pi i}{N} nm} \tag{4.25}$$

Where $m = 0, 1, \cdots, N-1$, N is the number of data points, and z and Z are the real space input and reciprocal space output respectively as discussed above. In

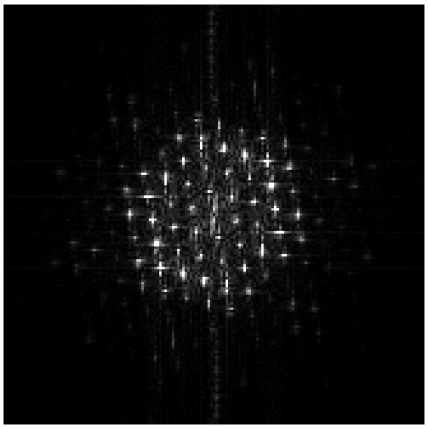

Figure 4.2: FT-STM image of a topographic STM image of the Si(111) 7×7 reconstructed surface.

the case of our analysis package the dFT is solved using the *Cooley-Tukey* fast FT (FFT) algorithm. [106, 107] Periodicities in the real space image are represented by peaks in reciprocal space at the wavevector of the lattice, the height of such peaks is a convolution of both the number of unit cells seen in real space and the prominence or intensity of the lattice in real space. In an ideal calculation a given lattice of size a would result in a single sharp peak at the wavevectors $\overrightarrow{k} = \pm q$ where $q = \frac{1}{a}$. However, in reality the FFT will produce a series of peaks of finite broadness at $\overrightarrow{k} = \pm jq$ for $j \in \forall\mathbb{N}$ where the intensity of the Fourier peak drops exponentially with increasing j. This effect is caused by the finite resolution of the STM data and the fact that data points are recorded in a square lattice, consequently some lattice positions are a single pixel closer or further apart resulting in the FFT calculation returning peaks at $\overrightarrow{k} = \pm(q + q, q + q + q \ldots$ or $jq)$ instead of $\pm q$. The same phenomenon occurs when two or more lattices are present. For two lattices a and b one expects to find reciprocal lattice peaks in the FFT image at $\pm q_a$ and $\pm q_b$ respectively and also satelite peaks for each superlattice at each permutation of $\overrightarrow{k} = \pm q_a \pm q_b$. However, in reality peaks are found for every $\pm jq_a \pm lq_b$ where $j, l \in \forall\mathbb{N}$ and peak intensity drops exponentially with increasing j or l. This also holds true if there are more than two lattices or periodic features present in the topographic image. Importantly, in order for a lattice to produce a clear peak in FFT the original topographic imaging (image) resolution must exceed critical sample for the lattice, namely at least four data points (pixels) per unit cell. As an example of the FFT process the calculated FT-STM image $Z(\overrightarrow{k}, V)$ of Fig. 4.1 is provided in Fig. 4.2.

In this example many Fourier peaks are seen, each of which can be assigned to either the Si unit cell, the 7×7 reconstruction, or both as described above. The

origin $\overrightarrow{k} = 0$ is located at the centre of the image. The peak width is a function of the standard deviation of the lattice period from its average, either real or as a result of the finite data grid, in general this is very low when imaging atomic lattices with many unit cells. However, abnormally wide peaks could also indicate modulation in the lattice period caused by charge ordering, density waves or simply scan drift. Measuring interatomic distances from their reciprocal lattice peak is more precise than attempting to measure the distances between atoms in real space images. This form of analysis is effective for any periodic modulation or structure and can often reveal periodicities in the real space images which are too subtle to see by eye. For example, a superlattice below the sample surface could have a highly periodic structure, however the effect on the charge at the surface may be very minor and as such the tiny modulations recorded may be too small for an observer to identify by eye, but because of the strong periodic nature a clear peak would appear in the FFT.

It is important to note that the reciprocal lattice for a hexagonal system does not transform simply as $a \rightarrow q = \frac{1}{a}$ as with linear or simple cubic systems. The Bravais lattice for a simple hexagonal system with lattice constant a is also a simple hexagonal lattice measuring $q = \frac{2}{a\sqrt{3}}$ rotated 30^{o} with respect to the original lattice. This is very important for the interpretation of FT images of systems which include hexagonal lattices, both for the correct determination of the real space lattice size and also for comparing orientations of hexagonal lattices with non-hexagonal lattices.

4.1.4 Imaging of CDWs and other similar phenomena by STM

Topographic imaging is a versatile tool for studying the physical structure and atomic lattices of surfaces as seen in the study of both the Si lattice and Si(111) 7×7 reconstruction. It is important to realise that the tunnelling current depends on the sample LDOS (eqn. 4.24), this means that electronic information about the sample surface is also convoluted into the topographic images. Consequently, a topographic image does not represent only the physical structure of a surface but also any electronic structure or phenomena which modify the LDOS. This can be a drawback when one is only interested in studying the real structure, but when searching for exotic electronic states this dependence can be a powerful tool. The convolution of physical and electronic structure can be difficult to analyse. However, for systems with known physical structure (e.g. those measured by XRD) it is possible to distinguish the different components of the image and gather useful structural information. Among the many exotic electronic states commonly studied by STM techniques are CDWs.

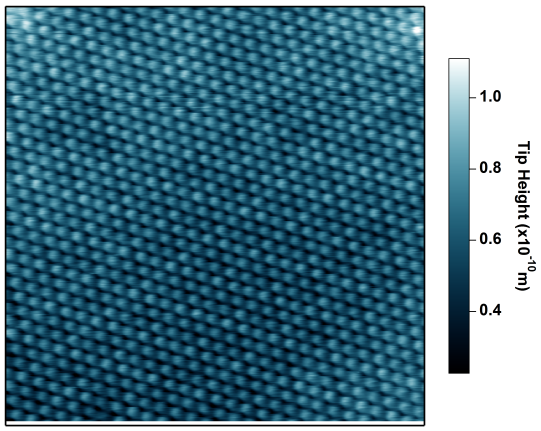

Figure 4.3: A 10×10 nm^2 topographic STM image of $NbSe_2$ recorded with +100 mV sample bias and 1 nA tunnelling current at 6 K. Note the hexagonal atomic lattice and near-commensurate 2D hexagonal CDW pattern which manifests as an small increase in topographic brightness on approximately every third atom.

STM imaging is the ideal tool for characterising both general properties of CDWs such as period, phase, symmetry and behaviour at different energies, as well as highly specific local information such as the effect of defects, dopants and other physical features on the CDW properties. $NbSe_2$ is one of the most studied CDW systems, it was one of the earliest CDW systems to be studied using STM and has been well characterised, it is now commonly used as a control or calibration sample for STM studies. Fig. 4.3 presents a topographic STM image of $NbSe_2$ as measured using a tungsten tip by the UCL low temperature STM (LT-STM) (see Sec. 4.3.1).

The image presents a hexagonal atomic lattice which matches the expected Se-lattice structure for the $NbSe_2$ surface. A second larger 2D hexagonal pattern is dimly visible, as expected for the CDW. This is a very typical manifestation of a CDW as seen by STM, namely an increase in topographic height in areas of increased LDOS rather than the appearance of additional structure as would be expected for a superlattice or dopant. The measurement was recorded at $T = 6\,\mathrm{K}$, below both the CDW transition of 33.2 K and the superconducting transition $T_C = 7.2\,\mathrm{K}$. Not all CDWs persist within the superconducting phase, in fact it is more common for a CDW state to switch off when cooling through the superconducting transition, however this does not mean co-existence of both states is unique to $NbSe_2$(see Section 2.2.3). In this case the periodicity and phase of the CDW are difficult to determine precisely in real space due to the small topographic amplitude, FT-STM can be used in order to further characterise the phenomenon. [108]

Fig. 4.4 presents an FT-STM image of $NbSe_2$ as calculated from the topographic STM image given in Fig. 4.3. The superposition of two hexagonal lattices, namely

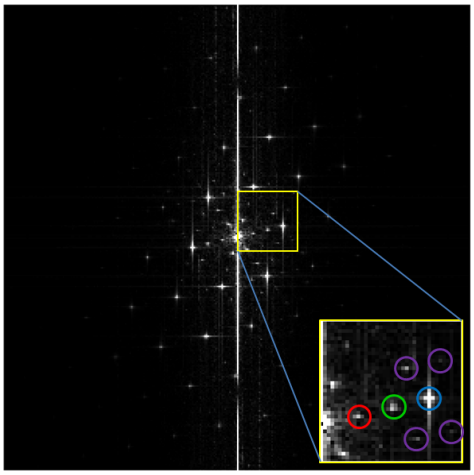

Figure 4.4: Fourier transform STM image of $NbSe_2$. The bright primary hexagonal lattice (blue circle inset) matches the reciprocal lattice position of the Se-atoms. A smaller hexagonal set of peaks (red circle) can be seen, this is ascribed to the hexagonal CDW phase. The purple circles mark CDW satelite peaks around the primary lattice peak. The green circle marks an overlap between the second harmonic of the CDW peak and one of the CDW satelite peaks from the primary lattice peak.

those of the Se atoms and the CDW, produces a complex array of hexagonal peaks. It is evident from the size of the wavevector and the intensity that the brightest hexagonal pattern of peaks matches the reciprocal Se lattice for all $k = \pm q_{Se}$ in each of the three symmetry directions, for clarity one peak from this set is circled in blue within the expanded inset. A second hexagonal pattern with a smaller wavevector is produced by the CDW for all $k = \pm q_{CDW}$ in each of the three symmetry directions, one of these peaks is circled in red within the inset. The CDW and Se lattices share the same symmetry directions. Furthermore, the CDW appears near-commensurate with $q_{Se} \simeq 3q_{CDW}$, therefore in real space the CDW has a periodicity three times that of the Se lattice $a_{CDW} \simeq 3a_{Se}$. The remaining Fourier peaks are ascribed to harmonics or satelite peaks as described in Section 4.1.3. A number of examples are given within the inset; the purple circles mark part of a hexagonal set of CDW satelite peaks $\pm q_{CDW}$ around q_{Se} and the green circle marks an overlap between one such CDW satelite peak and the second harmonic $2q_{CDW}$ of the CDW reciprocal lattice peak from the origin. In commensurate systems such overlaps are expected, it is analagous to superposition between two harmonic waves. Note that whilst at this scale the CDW is near perfectly commensurate XRD experiments, which sample a greater number of unit cells, have established that the CDW in $NbSe_2$ is in fact slightly incommensurate by a factor of order 1%. This highlights some of the limitations of STM techniques, namely that they are highly localised and measurements often do not include a large number of unit cells. Furthermore, it is important to remember

that STM has a limited resolution, either the size of the pixels in the image or the instrument's limit of resolution, which is typically around 0.01 nm (see Section 4.3.1), whichever is higher.

Topographic imaging and FT-STM has allowed the characterisation of the period, symmetry and commensurability of the CDW. However, imaging techniques alone are limited in that they cannot always distinguish between different types of physical and electronic structures. Topographic images trace a contour of constant charge density as discussed in Section 4.1.2. However, this contour is a convolution of the surface structure together with any factors which affect the local charge density, this includes CDWs, but can also include a number of other phenomena which affect the LDOS. When studying unexpected LDOS phenomena it is important to consider all the possibilities before concluding whether the system is exhibiting a CDW or not. Numerous exotic electronic states or phenomena can appear similar to CDWs in topographic imaging, these include, but are not limited to: Charge ordering, Jahn-Teller distortions, dimerisation, surface reconstructions and relaxation, electron standing waves and SDWs.

Charge ordering is seen in systems which contain one or more elements with multiple oxidation states, for example in manganites, in these systems the different ion valencies may arrange in regular pattern creating a uniform structural lattice of atoms but with a superlattice of different charge states. [109] Jahn-Teller distortions [110] are a type of geometic distortion by which a system reduces degeneracy, dimerisation is in fact an example of a Jahn-Teller distortion and the most studied example of a dimer surface seen in STM is the Si(100) surface. Both of these effects require specific criteria, namely element species with multiple oxidation states for charge ordering, and tetragonal or octagonal bonding systems for Jahn-Teller distortions, consequently when dealing with graphitic systems which are 2D, hexagonal and monovalent systems these two phenomena can be discounted.

Surface reconstructions occur when the surface structure or lattice symmetry varies significantly from the bulk material, whereas surface relaxation refers to either a change in the bond length perpendicular to the surface plane, or depletion of surface lattices or superlattices. Au(100) has a surface reconstruction, in this case the bulk Au structure is face centre cubic (FCC) but under certain temperature conditions the surface atoms rearrange into a hexagonal lattice, consequently the surface has the appearance of a hexagonal lattice superposed with a stripe pattern caused by interference between the bulk and surface structures. [4] In CaC_6 the strong sp^2

bonding seen in the graphene layers means that it is unlikely a graphene surface would undergo a reconstruction or depletion. However, the Ca superlattice is much more weakly bound and the possibility of one or more such surface effects cannot be discounted.

The presence of defects, adatoms or dopants can significantly alter the LDOS of the surface around them. One example of such an effect is an electron standing wave; a spatial modulation of the LDOS around a charged dopant, defect or feature such as a step edge. [41] Electron standing waves appear as rings or stripes which disperse with energy, in Fourier space this manifests as a peak with an energy-dependent wavevector. These kind of effects are most commonly seen in metallic systems such as cuprates [80] but can also be seen in semiconducting samples such as doped silicon surfaces. Finally, SDWs are very closely related to CDWs are can sometimes occur in the same systems, however STM is blind to SDWs unless the measurements are done using a spin-polarised probe so for the measurements taken in this thesis this phenomenon can be discounted.

In conclusion, there are many electronic phenomena which can manifest similarly to CDWs in topographic STM imaging. For some phenomena knowledge of the bulk properties of the material allows one to discount the possibility (Jahn-Teller, dimerisation, charge ordering), others are discounted because of the nature of the measurements (SDW). However, for a given CDW-candidate this still leaves surface reconstructions, depletions and electron standing waves. Topographic imaging alone cannot conclusively distinguish between the various manfestations of these different effects, therefore it is necessary to explore the spectroscopic properties of the surface, namely the behaviour of the LDOS with energy.

4.2 Spectroscopic techniques

This section concerns the concept of tunneling spectroscopy and its application in the numerous spectroscopic imaging (SI) and tunnelling spectroscopy (STS) techniques allowing the user to probe the LDOS and electronic structure of surfaces and surface phenomena. These techniques can be very important for distinguishing between different surfaces with similar physical structures or for ascertaining the nature of ambiguous surface features such as superlattices and surface modulations.

4.2.1 Probing the local density of states by STS

The simplest form of spectroscopic measurement is STS. The STM tip is held at a fixed position with the feedback loop disabled such that the tip height remains constant, i.e. the tunnelling barrier is fixed. The measurement is then performed by applying a recorded alternating current (AC) voltage pulse across the tunnelling barrier, the response of the tunnelling current is recorded by an electrometer yielding a spectra $I(V)$ relating current and voltage. Recall that in general the position-independent tunnelling current is dependent on voltage, tip-sample separation and the sample LDOS (equation 4.23). For a fixed sample position D_0 the exponential term can be reduced to a constant e^{-2kD_0} such that the current $I(V)$ is dependent only on the voltage and LDOS as shown in equation 4.26:

$$I(V) = C_0 \int_0^{eV} \rho_s(\varepsilon + E_F - eV)\mathrm{d}\varepsilon \tag{4.26}$$

Where $C_0 = -\frac{4\pi e}{\hbar}\rho_t(0)e^{-2kD_0}$ is a constant. The $I(V)$ spectra recorded by the STM can be differentiated in order to calculate the conductivity, $g(V)$, which is closely related to the LDOS. Spectra are typically plotted as a function of V with the Fermi level, E_F, plotted as $V = 0$, therefore the generalised LDOS term, $\int_0^{eV} \rho_s(\varepsilon + E_F - eV)\mathrm{d}\varepsilon$, is better expressed only in terms of gap voltage such that: $\int_0^{eV} \rho_s(\varepsilon + E_F - eV)\mathrm{d}\varepsilon \simeq \int_0^{V} \rho_s(V)\mathrm{d}V$.

$$g(V) = \frac{\mathrm{d}I(V)}{\mathrm{d}V} \simeq C_0\rho_s(V) \tag{4.27}$$

STS data is typically presented in terms of $g(V)$ which is proportional to $\rho_s(V)$. The same data can also easily be expressed as a function of energy $E = eV$ if desired. An example of STS data which has been numerically differentiated to give $g(V)$ is provided in Fig. 4.5. In this example the presented $g(V)$ is the average of 100 spectra each recorded at a tunnelling set point of +800 mV and 50 pA. This means that the tip height was normalised at 800 mV sample bias for a tunnelling current of 50 pA using the feedback loop then the loop was suspended for measuring $I(V)$ whilst sweeping the voltage from +800 mV to -800 mV. This kind of measurement can yield important information about the electronic structure of the surface. In this case the spectra are V-shaped as expected at the Fermi level close to the Dirac point in graphite - here the π and π^* bands meet at a point of near-zero density - undoped graphite is referred to as a zero band gap semiconductor or a semi-metal (see Chapter 2 for more details).

In addition to observing the expected LDOS shape for graphite these spectra also tell us that there is little or no doping in this sample, because we see no shift of the

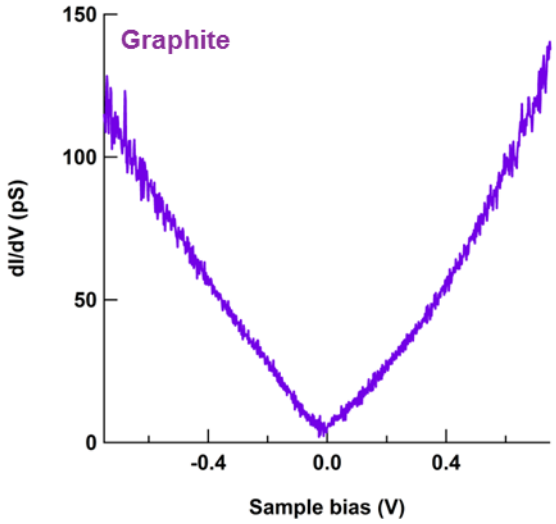

Figure 4.5: Position-independent differentiated STS $g(V)$ recorded on a graphite sample with a tunnelling set point of +800 mV and 50 pA.

LDOS minimum away from $V = 0$ (i.e. the Fermi level) and $g(0) \simeq 0$ - in a doped system the Fermi level would rest within either the π or π^* band resulting in a metallic system where $g(0) > 0$. In other systems STS can also be used to measure gaps in the LDOS such as CDW gaps [54], the characteristic depletion of states around E_F, and superconducting gaps, the energy gap introduced by the Cooper pairing mechanism in BCS superconductors.

4.2.2 Spectroscopic imaging techniques

STS techniques can help with the identification and characterisation of the kinds of electronic and charge phenomena discussed in section 4.1.4 but are still limited in that the measurements are largely position-independent and sample sets are small. SI techniques can be used to gather position-dependent spectroscopic data sets, allowing the user to learn information about how the LDOS varies on a local scale and to associate LDOS features with specific positions or features on a surface. The SI technique used in this thesis is called current imaging tunnelling spectroscopy (CITS). In this mode spectra are taken in a regular grid, combining the image-rastering techniques with the spectroscopic measurement technique of STS at each data point. This technique yields a position-dependent set of spectra in a similar fashion to current imaging (equation 4.24) but instead of measuring current at constant V spectra $I(V)$ are measured at every position $\overrightarrow{r}$ for a fixed tip height to generate a four-dimensional data set $I(\overrightarrow{r}, V)$. Combining equations 4.24, 4.26 and 4.27 gives the approximate relation between conductivity, calculated from measured CITS, and surface LDOS as

expressed in equation 4.28.

$$g(\overrightarrow{r},V) = \frac{\mathrm{d}I(\overrightarrow{r},V)}{\mathrm{d}V} \simeq C_0\rho(\overrightarrow{r},V) \tag{4.28}$$

Data of this form can be plotted either as an array of LDOS (conductivity) images for each V or as an STS measurement for a specific position $\overrightarrow{r}$ on the surface. This type of measurement is commonly used in the study of dopants, defects, steps and other features and is particularly useful for identifying effects such as electron standing waves. Furthermore, the use of topographic imaging and SI together can allow for differentiation between physical and electronic structure, something which topographic imaging alone cannot achieve. On very flat surfaces only electronic structure is seen in SI, whereas both electronic and physical structure are seen in topographic images, comparison of the two can allow the user to identify the nature of interesting features seen during imaging. Furthermore, the user can extract STS curves from interesting surface locations in order to see how the LDOS varies over the entire voltage range. When the surface is not very flat (e.g. large adatoms, steps or terracing) then some small component of physical structure can be seen even in LDOS images. This is because if the changes in sample topography are too great then the tip height renormalisation between data points can be imperfect resulting in a slightly position-dependent value for z which is included within C_0 in equation 4.28.

4.2.3 Fourier transform spectroscopy

FT-STS works in a very similar way to FT-STM. Rather than performing a 2D FFT on a single topographic image FT calculations are made at every voltage for the position-dependent conductivity $g(\overrightarrow{r},V)$ yielding reciprocal space conductivity $g(\overrightarrow{k},V)$ as a function of sample bias V and reciprocal space vector, $\overrightarrow{k}$, conjugate to real space position. This type of spectroscopic analysis utilises CITS measurements to access the LDOS contributions from specific points in Fourier space, this allows the user to track dispersion in electronic phenomena and assign electronic structure to specific $\overrightarrow{k}$ vectors. FT-STS data can be plotted either as reciprocal space images $g(\overrightarrow{k},V)$ at a fixed V or as conductivity curves for a specific position $\overrightarrow{k} = q$ where q is the reciprocal space position of a specific electronic feature. However, whilst $I(\overrightarrow{k},V)$ or $z(\overrightarrow{k},V)$ describe both structural and electronic features $g(\overrightarrow{k},V)$ describe only electronic features to within the limitations discussed in section 4.2.2. Peaks in FT-STS images are described in the same way as peaks in FT-STM images as

discussed in section 4.1.3. An example of FT-STS analysis of $NbSe_2$ is provided in Figs. 4.6, 4.7 and 4.8.

The spatially averaged $g(V)$ for the $NbSe_2$ surface (surface shown in Fig. 4.3) is presented in Fig. 4.6, this data was recorded by CITS at 10 K which is below the CDW transition but above T_C for superconductivity. Ideally the spectra should show small CDW gap of approximately 32 mV and an asymmetric LDOS with greater conductivity below the Fermi level. The spectra provided satisfies the latter condition, however the spectra is missing features above the Fermi level including features from the CDW gap, this is most likely due to an imperfect tip whereby the tip does not have a uniform DOS at high bias, this results in an imperfect measurement of the sample LDOS at these energies. Consequently the data is not perfect, however it is sufficient to demonstrate the principles of FT-STS. Fig. 4.7 presents a series of images $g(\overrightarrow{k}, V)$ for six different voltages. The Se atomic lattice and CDW lattice, together with their respective satelite peaks, can be seen at voltages close to 0 mV, however at high voltage (+50 mV) only white noise is seen as expected in light of Fig. 4.6. It is immediately apparent that at different voltages different parts of the reciprocal lattice are responsible for conduction (i.e. different parts of the Fermi surface) as the relative intensities of the peaks change significantly between the images, it is however easier to quantify this effect by isolating peaks of interest and plotting the respective contribution to the LDOS. Fig. 4.8 presents such an approach, in Fig. 4.8a a peak is circled for each lattice, Se and CDW, located at q_{Se} and q_{CDW} respectively. The remaining panels present the extracted conductivity contributions for each of the two lattice q vectors and an average of the background, which is taken anywhere that is dark in the image at 0 mV when all the reciprocal lattice peaks are visible. It is immediately apparent that there are significant differences between the extracted LDOS contributions. The background shows only a broad parabolic shape which is simply a reflection of the fact that at higher energy one expects more noise (e.g. a small vibration will produce a larger current response at higher voltage) but is otherwise featureless. The Se atomic lattice shows an approximately constant contribution at all voltages as one would expect for a perfect metal, deviation from this is due to a number of factors; thermal noise, imperfect tip (as discussed), and amplification of noise in the data by the numerical methods used to analyse the data (numerical differentiation and FFT). However, the most interesting is the contribution from the CDW; the significant asymmetry of the overall LDOS around the Fermi level is reflected only in the contributions from the CDW. Had the tip been perfect one

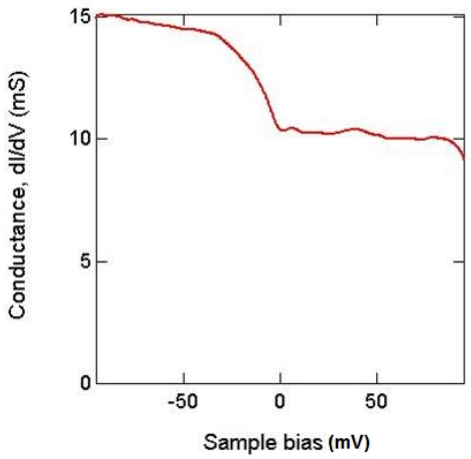

Figure 4.6: Spatially averaged conductivity $g(V)$ from a CITS data set recorded on a $NbSe_2$ surface at +100 mV sample bias and 50 pA tunnelling current set point. Data was recorded at 10 K.

would also expect to see a gap in the conductivity around the Fermi level in the CDW contribution. Importantly, this technique demonstrates that a feature seen in the overall LDOS can be tied to a particular periodicity or lattice which gives unique electronic information about specific physical or electronic structure seen in imaging. This is a very valuable tool for analysing phenomena which manifest with a regular structure and can help to differentiate between effects such as CDWs and surface reconstructions where imaging or position-independent spectroscopy alone cannot. Other similar applications of this technique include the study of dispersing electronic features in high-temperature superconductors, particularly in the study of the checkboard patterns of cuprate superconductors. [80]

4.3 STM-related methodology

This section concerns experimental details of the STM instrumentation and other STM-related methodology which has not already been covered, this includes noise reduction and tip preparation. Sample preparation is covered in Chapter 3.

4.3.1 Instrument details

The CaC_6 and $NbSe_2$ experiments reported in this thesis were all performed on an Omicron LT-STM. This STM has a temperature range of 4.2 K up to room temperature (RT) achieved by an vacuum-insulated cryostat consisting of a liquid nitrogen bath surrounding a liquid helium tank coupled directly to the STM head with a heater installed on the STM head itself. However, note that all CaC_6 experiments reported

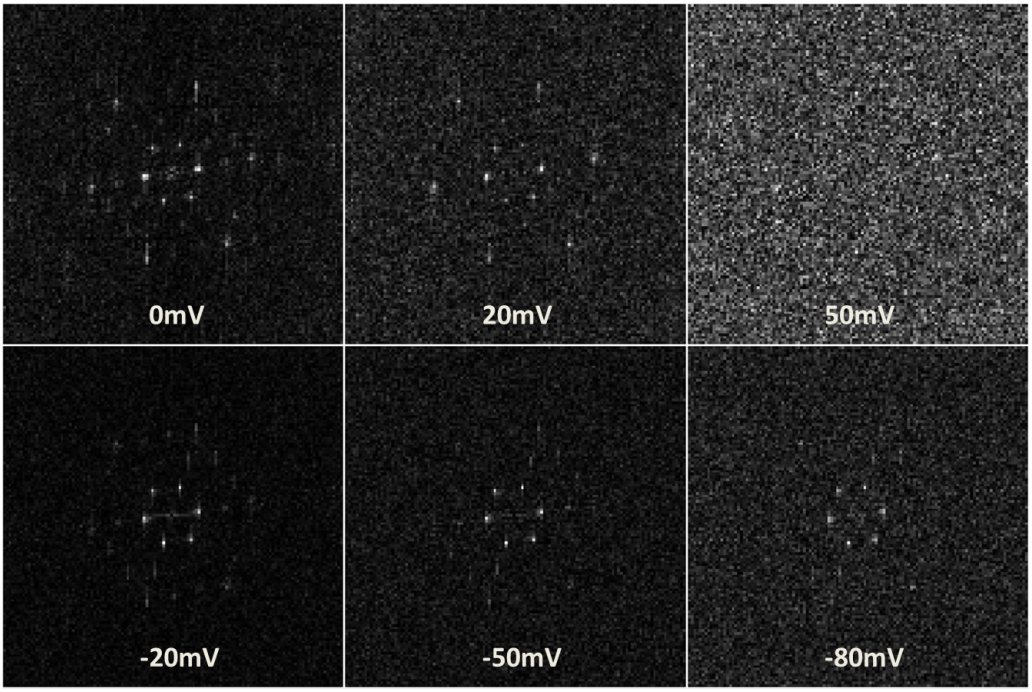

Figure 4.7: FT-STS images $g(\overrightarrow{k}, V)$ of $NbSe_2$ recorded at +100 mV sample bias and 50 pA tunnelling current set points. Each image is a single frame at the sample bias indicated.

in this thesis were performed at a controlled 78 K against a cold reservoir of liquid nitrogen at 77 K. The STM chamber has a true UHV environment with a base pressure of approximately 10^{-11} mbar achieved by a combination of a turbo pump, ion pump and titanium sublimation pump. This is true even for experiments performed at RT as the STM and sample preparation chambers are kept ultra-clean and there is no need for cryo pumping. The preparation chamber also has a residual gas analyser (RGA) which is used to confirm the absence of any water or oxygen contamination. The STM tip itself has macroscopic x, y and z motion by means of a piezo tube allowing for experiments probing many different surface locations on a given sample. This is particularly important for studying polycrystalline samples such as HOPG and HOPG-based GICs.

The STM data presented for raw unintercalated graphite was recorded using an Oxford low temperature STM. This STM has a cryogenic flow cryostat suitable for use with either liquid helium or nitrogen coupled by copper braids to the STM head allowing for a temperature range of approximately 5 K up to RT. The Oxford STM is also maintained at UHV with a base pressure better than 10^{-10} mbar achieved through turbo, ion and sublimation pumping. The STM tip has no macroscopic in-plane motion, consequently this STM is more appropriate for samples with relatively large in-plane crystal sizes such as natural flake graphite.

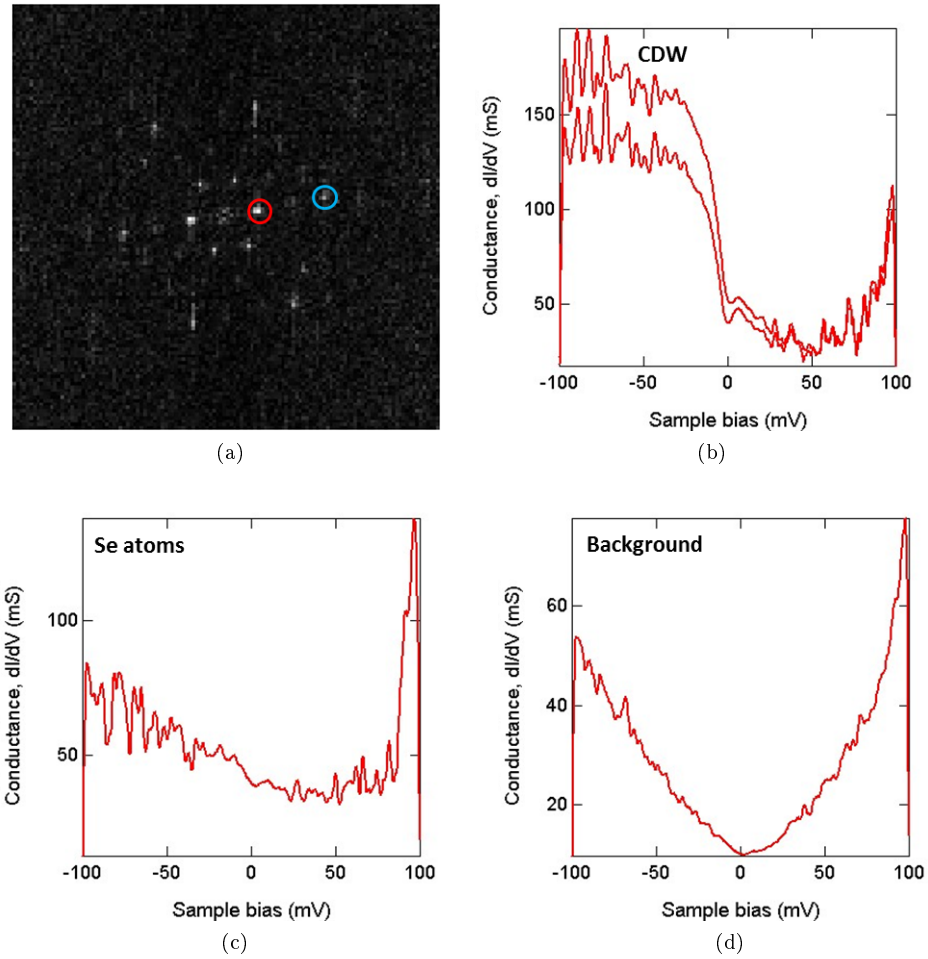

(a) (b) (c) (d)

Figure 4.8: FT-STS measurements of $NbSe_2$ recorded at +100 mV, 50 pA set point and 10 K. (**a**) $g(\overrightarrow{k}, 0)$ image with a peak located at the Se atom reciprocal lattice position, q_{Se}, marked by a blue circle and a peak at the CDW reciprocal lattice position, q_{CDW}, marked by a red circle. (**b-d**) Spectra $g(q_{CDW}, V)$, $g(q_{Se}, V)$ and $g(q_B, V)$ respectively, where q_{CDW} and q_{Se} are as indicated in (a) and q_B represents a set of random background vectors corresponding to dark areas in image (a).

Neither STM has a magnetic field, although the STM lab at UCL does also contain an Omicron cryo-STM with a base temperature of 2 K and a vector-field with a maximum magnetic field of 6 T. This instrument was not used for any of the experiments reported in this thesis, however, it is an important tool for future work. Naturally STM is highly sensitive to sources of noise. The Oxford STM uses a true sample bias system, whereby the voltage set point is applied to the sample and the tip is grounded. The LT-STM uses an effective sample bias system, whereby the sample bias is polarity reversed and applied to the tip and the sample is grounded. Therefore, in both cases when the voltage set point is quoted this can be considered the bias applied to the sample.

Vibrational noise can couple through the STM chamber to the STM head itself, lateral motion in the tip can interfere with high-resolution imaging and vertical motion can cause an exponential change in the tunnelling barrier which can ruin imaging or spectroscopy and in some cases even cause the tip to crash into the sample. In general low frequency noise is most damaging to STM measurements as things like atomic lattices and CDW have regular, low-frequency-like appearance in imaging and as such low frequency noise can obscure or warp measurements and can be difficult to distinguish or eliminate from real data. Consequently, great care is taken to minimise vibrational noise, not only throughout the lab but each STM also has its own vibration isolation system. At the time of the experiments reported the LT-STM was vibrationally isolated from the laboratory floor (the main source of vibrational noise) by means of four airlegs. In otherwords, during experiments the STM was floated on a cushion of high pressure (7 bar) air. This is particularly effective at minimising mid to high frequency vibrational noise. The Oxford STM has an active vibration isolation system consisting of springs and an active feedback system. Both of these systems are designed to minimise vibrational noise coupling to the STM chamber. In addition to this, the STM heads in both STMs are suspended by springs within the STM chamber in order to eliminate any vibrations coupling from the chamber walls to the head itself, particularly acoustic frequencies which could be picked up from the air in the lab.

Vibrational noise levels on the laboratory floor and the STM table were checked using an accelerometer before all important measurements, to ensure that the vibration isolation systems were working as well as possible. An example of such measurements in provided in Fig. 4.9. FT of a stable tunnelling current with a fixed bias can also be used to check noise levels, this can not only reveal any vibrational interference at the

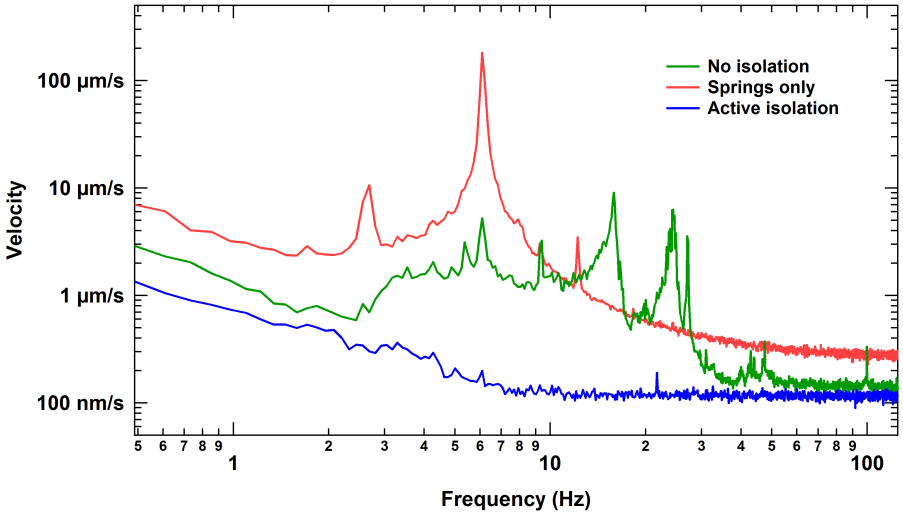

Figure 4.9: An example vibrational noise measurements recorded using an accelerometer. Note the dramatic reduction in noise between the unisolated (green) and fully isolated (blue) spectra, particularly the near-perfect elimination of mid to high frequency noise.

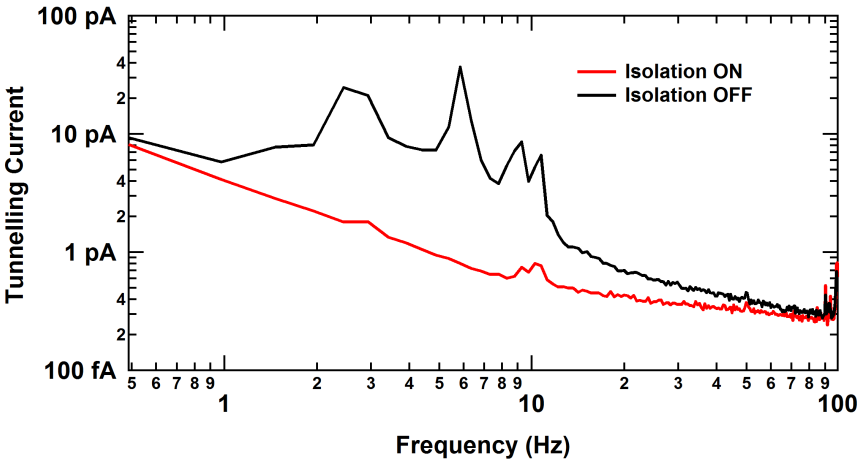

Figure 4.10: An example of vibration and electronic noise measurements recorded by FT of a stable tunnelling current. Note the dramatic reduction in noise with isolation on (red line) and that there is no peak at 50 Hz (mains frequency).

tunnelling junction but also any electrical noise which is leaking into the tunnelling signal, an example of this is provided in Fig. 4.10. Electrical noise is minimised in a number of ways; cables are shielded, any objects which could act as antennas are removed from the STM during experiments and the instrument ground is filtered to avoid 50 Hz noise picked up from the mains power supply.

4.3.2 Tip preparation procedures

Preparation of a sharp and stable probe is vitally important for effect STM and STS measurements. Broadly speaking there are three important considerations; probe shape, probe stability and the probe material. The material for the STM probe is chosen such that the DOS of the tip is featureless and constant (i.e. a perfect metal) in the desired energy range (0 - 10 eV) as discussed in Section 4.1.1. Many materials satisfy this criteria, both tungsten and platinum-iridium alloy (Pt-Ir) tips were used, each of which are very common choices in the STM community because they both show no notable features in their respective DOS close to the Fermi level. The preparation procedure for each material is slightly different but first it is important to consider the physical criteria of a good STM probe.

In order to resolve atom-scale objects on a surface the probe itself must be sharp such that the tunnelling junction always forms at the same point, namely the tip. The exact atomic configuration of the tip usually cannot be determined. However, so long as one single atom is closer to the surface than the rest then the tip can be considered atomically sharp. The macroscopic tip condition around this atom, namely the aspect ratio of the tip, can affect how well the tip is able to image sharp increases or decreases in topographic height, for example a step edge. If the tip is particularly broad, for instance shaped like a finger rather than a syringe, then one may expect tunnelling from the side of the tip when coming close to a step edge or other large feature and consequently the appearance of such an edge would become smeared and resemble a slope rather than a sharp step. Asymmetry in the structure surrounding the tip can also result in imaging abnormalities, most commonly these can be identified easily by comparing images recorded in left-to-right (forward) and right-to-left (backward) scan modes.

In addition to being sharp it is very important that the tip is stable. Namely that the atomic configuration of the tip does not frequently change and that the tunnelling junction always forms at the same point on the tip - the single atom closest to tip apex. Occasionally the tip will have more than one atom at the apex each equidistant

with the surface, consequently there are multiple tunnelling paths between the tip and the sample. If there are only a few such atoms (2 - 4) an image can still be resolved, however much of the data is meaningless as each surface feature or atom will be 'seen' multiple times. If there are many such atoms then the tip can be considered blunt and is unlikely to provide good data or resolve surface topography at the atomic scale. Changes in the tip condition are most common when the apex is not part of a large single crystal (i.e. not part of the Pt-Ir or tungsten). Frequently observed examples where this is not the case are oxidation of the tip (in the case of tungsten tips, Pt-Ir does not oxidise) or contamination by water. In the former case the conductivity of the tip is reduced which can either lead to tip crashes or oxide material dropping from the tip as a result of energy applied by the tunnelling current, in the latter case water adsorbed to the surface of the probe can crystallise at low temperature creating false water-crystal tips which are also very unstable. Furthermore, both of these scenarios present a problem for spectroscopic measurements as oxides and water crystals do not have the perfect-metal DOS desired for the STM tip. Another common cause of tip condition changes is contamination of the tip by the sample, with some samples the probability of this is low (e.g. samples with strong surface bonding and large crystal sizes, such as most metals) however graphitic samples in particular are susceptible to small flakes of graphite electrostatically adhering to the tip. Furthermore, GIC samples in particular are sometimes difficult to scan due to the propensity for intercalant material to become mobile on the sample surface and contaminate the tip causing frequent tip condition changes which play havoc with imaging and spectroscopy.

The best way to avoid these problems is through good tip preparation and maintenance. *Ex situ* tip fabrication varies depending on the material used for the tip. In the case of Pt-Ir tips the fabrication procedure is relatively simple, a Pt-Ir wire is clamped between pliers and a wire cutter and then cut and pulled such that the wire is stretched and broken, usually resulting in a sharp, pointed tip. Whilst this is an imprecise technique and frequently results in probes which look somewhat asymmetric on the macro-scale the success rate of such tips was found to be very high indicating a high probability of a clean and sharp tip at the micro-scale. The resilience of the Pt-Ir alloy precludes any other viable fabrication technique, whilst this could be seen as a disadvantage this same resilience is also useful in that Pt-Ir tips do not oxidise or react with air and, in the author's experience, contaminants from samples bind less readily to Pt-Ir tips than those made with other materials. The cutting method

can also be applied to the manufacture of tungsten tips, however the success rate was better when the tips were prepared by chemical etching. This is a common technique in STM [111], the method consists of a DC circuit made by placing a platinum cathode on the fluid surface of a beaker of 3 Mol KOH solution and submerging the end of the anode, a thin tungsten wire oriented vertically, 1 mm below the surface of the KOH solution. A DC voltage is then applied initiating the etching process. The voltage is maintained for two to three minutes until the wire is etched away from the surface of the KOH solution and the circuit is broken. The freshly-made tip is then submerged in deionised water in order to prevent any further etching. If successful the tip produced is extremely sharp and appears both shiny and syringe-shaped under an optical microscope.

Once the new tips are transferred to the UHV preparation chamber further *in situ* preparation is performed. The tips are heated by means of a resistive heater to approximately 250 ^{o}C in order to fully degas them and remove any water or oxygen. Typically this takes up to 12 hours after which time the pressure gauge should show no increased pressure in the preparation chamber due to the tip heating. After degassing the tips are transferred to the STM chamber and characterised by field emission (FE) [112] using a custom-made tip tool. This involves bringing the tip to with in a few mm of a grounded tungsten filament with the apex of the tip oriented towards the filament. The tip is then swept with a DC voltage from 0 V to -1.1 kV whilst the current flow from the tip to the filament is monitored. If FE from the tip is successful a small current is detected. The resultant FE $I(V)$ curve can be used to characterise the tip. A sharp tip should exhibit a well-defined onset voltage where current is first detected, the current should then increase exponentially with increasing negative voltage until saturation (1 μA). If a tip is blunt then either no FE will be seen, or saturation will not be achieved above -1.1 kV. If the tip has no single well defined apex (i.e. is a multiple tip) then switching between different FE profiles will be seen, these appear as small but spurious increases and decreases in current which do not follow the shape of the FE $I(V)$ curve. This process can also be used to assess the stability of the current tip configuration; a tip can be considered stable if the onset voltage is the same over a number of FE cycles and the $I(V)$ curves from each cycle have the same shape. An example of FE $I(V)$ curves taken from a sharp and stable tip are given in Fig. 4.11.

If any of these criteria is not met the tip is not considered suitable for STM it its current state. Most commonly blunt tips must be disposed of, but unstable or

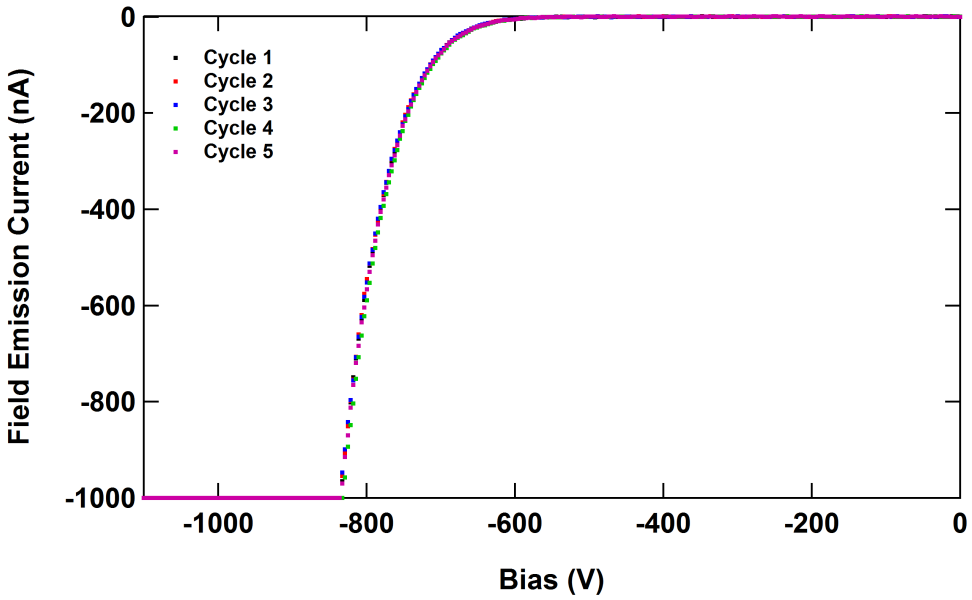

Figure 4.11: A sharp and stable single-tip STM probe as characterised by FE. Note that the onset voltage for FE and the shape of the $I(V)$ curve is consistent over five cycles and that the saturation current is achieved above -1.1 kV. In this case the tip was made from tungsten by the DC etching method and had undergone all *in situ* preparation including e-beam heating.

multiple tips can be e-beam heated in situ in order to reconfigure the apex of the probe. Furthermore, tungsten tips are always e-beam heated in order to remove any oxide material from the tip - this is not a problem with Pt-Ir tips as they do not oxidise. The e-beam heating is done using the same custom tip tool with tip and filament positioning as described for FE. The filament is resistive heated by a DC current in order to stimulate the release of thermally excited electrons, typically this requires between 3 and 5 A of current. The tip is then biased at +407 V with respect to the filament resulting in e-beam bombardment of the tip from the filament. Usually an e-beam current of 50 to 100 μA provides sufficient heating of the tip to reconfigure the apex and sublimate any tungsten oxide. Following e-beam treatment FE characterisation is repeated in order to assess the condition of the tip.

Whilst these processes may seem convoluted ultimately the goal is simple; to produce a well-characterised, clean, stable, sharp and single-tipped probe with a featureless LDOS which is suitable for high-quality and repeatable imaging and spectroscopy. Once this has been achieved the tip is loaded into the STM and used for taking measurements.

4.3.3 Presentation of STM data

Imaging data measured by STM commonly has large arbitrary tip height offsets, this is because the extension of the fine piezo is not always the same for all experiments due to the fact that sample heights and tip lengths vary. Furthermore, whilst great care is taken to make sure the plane of the sample surface is perpendicular to the STM tip it is inevitable that on an atomic scale there may be some slight slope. Consequently, all STM imaging data is flattened using a plane-wise correction (importantly line-wise and polynomial corrections are not used as these can greatly bias data regarding the tip height) and the topographic height is set to zero at the minimum point of the image. This is a valid correction since the STM records relative tip height not absolute tip height, as discussed in Section 4.1.1.

It is possible to filter STM data to remove high or low frequency noise post-recording. This can give STM images in particular a more noise-free and flat appearance. Furthermore, there are numerous ways of drift-correcting STM images such that thermal expansions and contractions between sample and tip, otherwise known as tip creep, can be accounted for. There are a number of ways to achieve this, in the most extreme cases data can be warped by a polynomial correction factor so as to match a measured lattice's size and symmetry to the known or expected structure. A simpler approach which can account for most types of thermal drift is to simple shear the image around its central point. This approach has the advantage of not introducing false symmetry or distortions to the lattices measured. However, unless specifically stated otherwise all data presented within this thesis is shown as recorded without filtering or drift-correction of any kind. In cases where data presented has been drift-corrected only the shearing method has been used as warping the image can create false distortions in atomic lattices and other such problems.

Chapter 5

STM studies of CaC_6

This chapter presents STM imaging and spectroscopy of the CaC_6 surface. Numerous surface types are seen, each of which is characterised by detailed topographic and FT-STM analysis. Most notably an unexpected stripe phase surface type is presented and crystallographically analysed in conjunction with complementary spectroscopic data. Evidence for the CDW nature of the electronic stripe phase is presented together with a detailed characterisation and discussion of this newly discovered phase.

5.1 Introduction to CaC_6 surface types

An extensive surface study of four different CaC_6 samples revealed a number of different surface types. Broadly these can be divided into surfaces which could be atomically resolved and those which could not. These two surfaces categories can be subdivided further based on the subtle differences in surface conditions and, in some cases, profound differences in the lattices observed. Each surface type is characterised and discussed in detail in its respective section. It should be noted that of the four CaC_6 samples scanned two exhibited no atomically resolved surfaces. This is likely due to unsatisfactory cleaving of the sample leading to the surface being too rough or containing too much loose surface material which prohibits a stable tunnelling junction. The remaining two samples exhibited the other reported atomically resolved surfaces. Furthermore, one sample exhibited every reported surface at least once. All data presented was taken at 78 K under UHV conditions.

5.2 Non-atomically resolved surfaces

5.2.1 Definition

Non-atomically resolved surfaces are defined as surfaces which, when scanned by STM, do not exhibit a measurable atomic lattice in imaging. This can be due to a number of reasons such as excessive roughness of the surface, or prevalence of weakly bound material (e.g. loose atoms, molecules and other contaminants) on the sample surface. Such material can interfere with the stability of the tunnelling junction or contaminate the STM tip causing it to become blunt or less metallic. In extreme cases the surface is considered unscannable, namely topographic images are incoherent or 'unreal' and show no discernable features of any kind. In over half of the instances of successful imaging a non-AR surface was revealed. In some cases the atomic lattice of the surface may be obscured but imaging still reveals large-scale features of the surface. Unlike other surfaces types presented in this chapter non-atomically resolved surfaces are not a class of surface but rather a collection of unclassified surfaces, some of which can exhibit quasi-unique qualitative (appearance) or quantitative (sizes of features and surface roughness) features. Surfaces of this type have previously been reported by Bergeal *et al.* [3] as part of a position-independent spectroscopic study of the superconducting state of CaC_6.

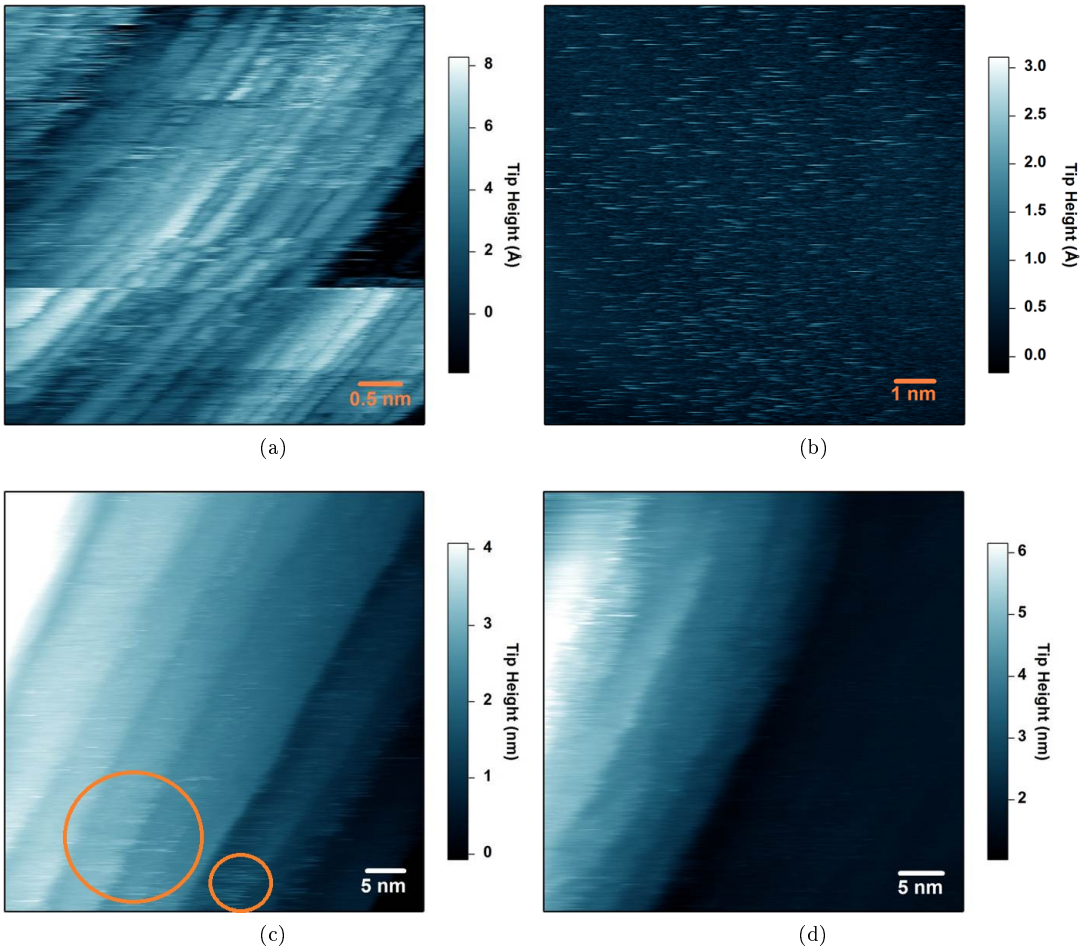

Figure 5.1: Non-atomically resolved CaC_6 surfaces as seen by topographic STM imaging. (**a**) Anomalous short range structures of indeterminant origin. (**b**) An extremely flat but unstable surface, image was recorded at +800 mV sample bias and 50 pA tunnelling current. (**c**) Unstable terraced surface, the orange circles highlight areas exhibiting significant surface mobility at terrace edges. (**d**) A second image taken to the bottom right of image (c). Images (b), (c) and (d) were recorded at +300 mV sample bias and 50 pA tunnelling current.

5.2.2 Topographic Imaging

A few examples of such CaC_6 surfaces, as seen by topographic STM imaging, are shown in Fig. 5.1. The first example, Fig. 5.1a, presents a surface which appears to show structure. However, the apparent stripe-like features are smaller in size than the in-plane carbon to carbon interatomic distance (approximately 1.42 Å), this indicates they are a scan artefact; a feature in the image which is generated as a result of noise in the tunnelling junction, a blunted or asymmetric tip, or other spurious scan effects. This kind of unreal surface is commonly seen when imaging GICs and is attributed to the propensity for GIC surfaces to exhibit high surface mobility and tip contamination caused by intercalant material or graphitic flakes which have become loosely bound as a result of the cleaving process. The high levels of noise in the fast scan direction

(see Chapter 4) which can be seen throughout the image, particularly in the top left, are also indicative of a rapidly changing tunnelling junction. This shows that there is material moving between the tip and the sample, either on the sample surface or on the end of the tip.

Fig. 5.1b presents a second type of unreal surface. This surface is extremely flat and one would usually expect to achieve atomic resolution on such a surface. However, there is a great deal of noise caused by a large number of changes in the tunnelling junction, these manifest as the 'spikes' seen throughout the image. One possibility is that this is a flat, successfully cleaved surface, however, instead of terminating in a graphene sheet the surface is terminated by a layer of calcium atoms. These atoms are no longer sandwiched between two graphene sheets as they are in bulk CaC_6, consequently they are weakly bound and move around on the surface. This movement causes rapid changes in the tunnelling barrier which prevents a stable scan of the surface, despite the flatness of the surface and the small amplitude of the noise spikes the random nature of the motion obscures the atomic lattice of the surface from being imaged.

Sometimes large scale features of the surface can be observed even if the atomic lattices are not. A good example of this is shown in Fig. 5.1c, a topographic image of a large area of highly terraced CaC_6 surface. The atomic lattice cannot be resolved but a number of steps are clearly seen. High surface (mechanical) mobility can be seen near the step edges, especially in the bottom right of the image. This effect is similar to that which is seen on various terraced surfaces, e.g. on the Cu(110) surface copper and oxygen atoms detach and reattach at step edges [113], the mobility of these atoms leads to a noise pattern qualitatively similar to that which is seen in Fig. 5.1c. If the features are indeed steps then this effect could be caused by intercalant atoms detaching and reattaching in a similar way and moving in and out of the galleries at these step edges. It is improbable that carbon atoms would be responsible for this effect as they are bound much more tightly to their lattice than the calcium atoms. [9, 91] It is interesting that so many step edges occur close together, this is probably due to the fact that individual crystals in HOPG samples can be significantly out of alignment with one another (Fig. 3.1) leading to some crystals being cleaved at an angle, not parallel to the ab-plane, thus creating more step edges at the surface. A second scan taken on the same surface is shown in Fig. 5.1d, displaying the surface region down and to the right of Fig. 5.1c. Note that the tip height values quoted in these two images are not absolute, the tip height value in each image is defined as zero

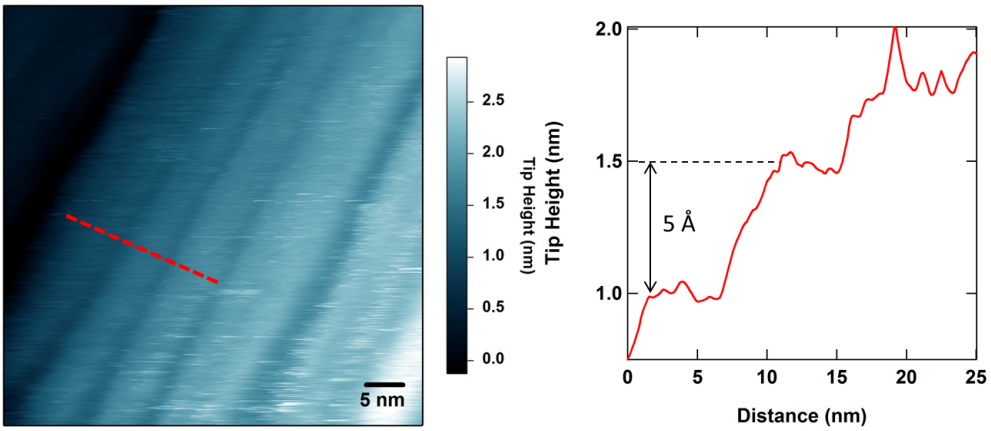

(a) (b)

Figure 5.2: Step edges on a CaC_6 surface. (**a**) A non-atomically resolved topographic STM image of a highly terraced region of the CaC_6 surface recorded at +300 mV sample bias and 50 pA tunnelling current. (**b**) A line profile corresponding to the red line seen in (a). An annotation illustrating the height of one of the step edges is also provided.

at their respective minimum heights. This second image shows that the terrace size can vary dramatically across the surface, and as before we see a significant amount of noise near the step edges. Although the large terrace which covers the right-hand side of the image is flat and noise-free it was not possible to resolve the atomic lattice. The important implication is that flatness alone is not sufficient to allow atomic resolutiom imaging and other properties of the surface have a significant effect. This is discussed further in section 6.1.

A second example of a highly terraced CaC_6 surface is presented in Fig. 5.2. The topographic STM image (Fig. 5.2a) is qualitatively very similar to Figs. 5.1c and 5.1d in that numerous terraces are observed, with significant surface mobility around the step edges. This is particularly apparent on the right side of the image. As a result of this effect most of the terraces do not have a well defined profile which makes determination of the step height difficult. In general the steps are measured to be 3 - 6 Å, a typical example is shown in Fig. 5.2b - a line profile taken as marked in Fig. 5.2a - in this particular case the step height is 5 Å. Whilst this is not a definitive identification of the surface the step heights observed are approximately consistent with what we would expect to see, namely the CaC_6 sandwich layer height of approximately 4.52 Å. [26] The small discrepancy between the expected value and those that are measured can be due to a number of effects. Firstly, if the tip is macroscopically blunt the exact position of the tunnelling junction can change near steep features of the surface, consequently features such as step edges can appear to be broader than they in fact are and the measured height can be slightly inaccurate. Secondly, partial

de-intercalation of galleries near steps, or mechanical damage to the step edges caused by cleaving, can result in an increase or decrease in the step height locally - this effect is a good example of a common problem with STM measurements, namely that local features do not necessarily always reflect the bulk or average structures.

Normally non-atomically resolved surfaces cannot be affected so as to reveal the atomic lattice, regardless of tunnelling parameters. However, occasionally such surfaces will spontaneously reveal atomic resolution without any specific stimulus. The reason for this is not fully understood, it is possible that the scanning action of the STM tip locally 'cleans' the surface of loosely bound material allowing the lattice to be imaged. A second possibility is that a particular tip condition change results in a tip which is sharper, more stable, or has stronger interaction with the atomic orbitals of the surface. Both of these explanations are speculative, but since it is not possible to independently observe the condition of the tunnelling junction one can only make an educated guess based on an understanding of how the STM works. That is, namely the principle that either the tip or the surface has become more conducive to high precision, stable tunnelling.

5.2.3 Spectroscopy

Non-atomically resolved surfaces are, as already discussed, a collection of different surface types characterised by the lack of AR imaging. Typically when the quality of imaging in insufficient to resolve atoms then spectroscopy is not attempted. The reason for this is that if the tip is too blunt, or contaminated, or the surface is too mobile then spectroscopy is likely to cause a tip crash and also will not yield reliable data. On the few occasions where, for completeness, spectoscopic measurements were attempted on surfaces for which atomic resolution had not been achieved measurements typically varied wildly between spectra and no characteristic shape or features could be determined for the LDOS. It is probable that most surfaces which cannot be resolved contain a significant amount of free calcium atoms or graphitic flakes which move in and out of the tunnel junction or contaminate the tip during spectroscopy rendering the current measured during the voltage sweep as meaningless. Bergeal *et al.* avoid this problem when studying the superconducting gap by performing only very small voltage sweeps. [3] However, this does not provide information about the LDOS significantly above or below the superconducting gap energy.

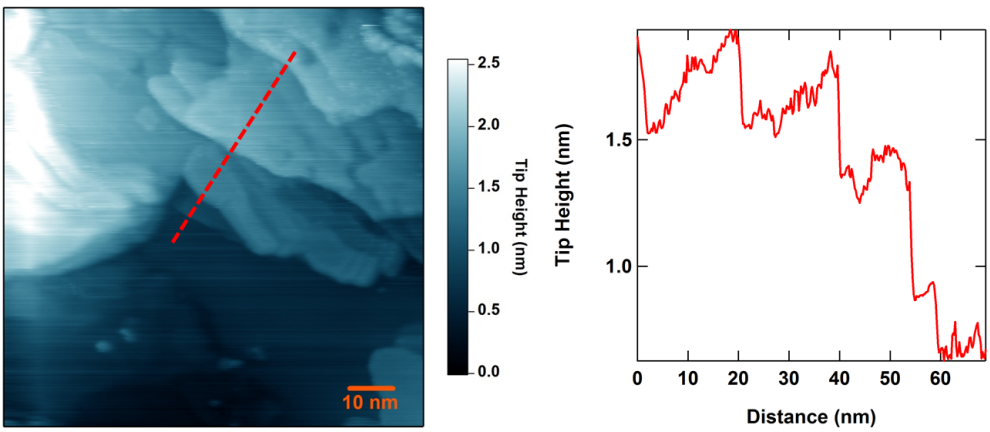

(a) (b)

Figure 5.3: A flat area of CaC_6 surface adjacent to an unusual formation of terraces. (**a**) A topographic STM image of the area recorded at +300 mV sample bias and 50 pA tunnelling current. (**b**) A line profile corresponding to the red line marked in (a).

5.3 Graphite-like surfaces

5.3.1 Definition

The samples used were very high purity (as discussed in Section 3.2), consequently one does not expect to encounter unintercalated surfaces. Nevertheless, in a small number of cases ($<$ 1% of surfaces scanned) the surface has an appearance which exactly matches graphite, with no discernable superlattice. This is attributed to a surface which has not fully intercalated, or has deintercalated, either by the mechanical stress of the cleaving process or deintercalation from exposed galleries as seen in section 5.2.

5.3.2 Topography and characterisation

Fig. 5.3a presents a topographic STM image of a flat area of the CaC_6 surface adjacent to a highly terraced region. Interestingly the terraces have an appearance akin to the formation of CaC_6 puddles on graphite when a partially-intercalated sample is imaged by SEM (see Fig. 3.5). Note that the surface exhibits far less mobility or noise than the surfaces presented in Section 5.2, this is an important factor in determining if atomic resolution can be achieved on a surface. A line profile across multiple terraces, as marked by the red line in Fig. 5.3a, is shown in Fig. 5.3b. The step heights observed are in the 3 - 5 Å range, on average this is slightly smaller than the expected height. Taking a closer look at the flat region shown in Fig. 5.3a with a smaller high-resolution scan reveals a hexagonal atomic lattice as seen in Fig. 5.4. Attempts to achieve atomic resolution imaging of the terraced area of the surface did not meet

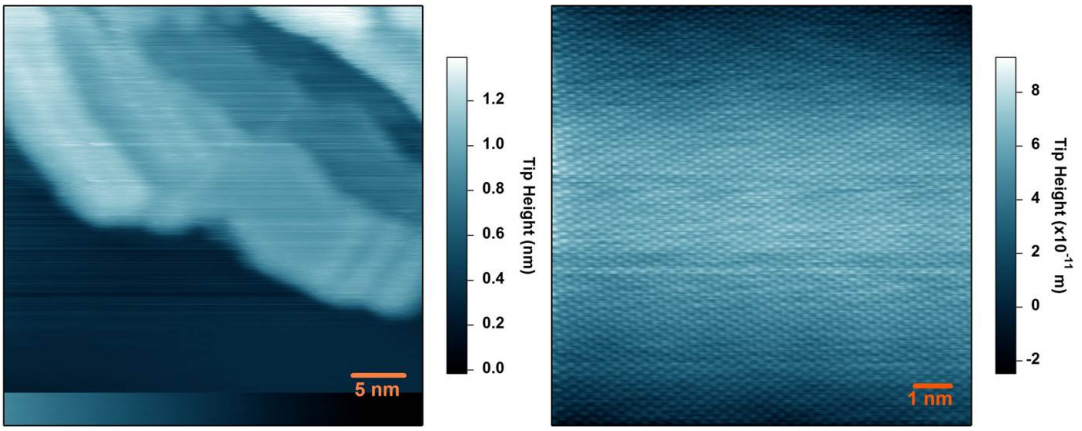

(a) (b)

Figure 5.4: Isolating a flat region of the sample to reveal a graphite-like surface. (**a**) Topographic STM imaging of progressively smaller area of the surface reveals (**b**) a hexagonal atomic lattice seen on the flatest area of the surface. (a) and (b) both recorded at +300 mV sample bias and 50 pA tunnelling current.

with success.

Close examination of this lattice (Fig. 5.5) reveals that it closely resembles the 2.46 Å hexagonal unit cell seen for graphite surfaces. Indeed, the phenomenon whereby only half of the carbon atoms are actually seen by the STM is also replicated. [114] No superlattice is evident, however, this can be confirmed by performing a FT as seen in Fig. 5.5b. The hexagonal lattice is present as expected but no other superlattice or periodicities can be seen. The size of the lattice can be determined most accurately by measuring and inversing the reciprocal lattice vector marked in red (see section 4.1.3). In this case we find the hexagonal lattice unit cell to be $a = 2.36 \pm 0.10$ Å in size.

It is therefore evident that the flat region seen in Fig. 5.3 is a graphite-like surface. It is possible that the terraced regions are either CaC_6, puddling around an area of unintercalated sample, in the same manner as seen in SEM, but at a smaller scale, or conglomeration of intercalant material which has deintercalated from the sample surface. Without measuring the atomic lattice it is impossible to be certain, and the step height alone is not conclusive - especially as it is not constant. In fact, some of the smaller steps could be argued to be closer to the 3.35 Å graphite interlayer distance than the CaC_6 sandwich layer size. [13]

5.3.3 Spectroscopy

An example of spectra recorded on a raw graphite surface is included in Fig. 4.5. However, whilst the imaging of these graphite-like surfaces very much resembles raw

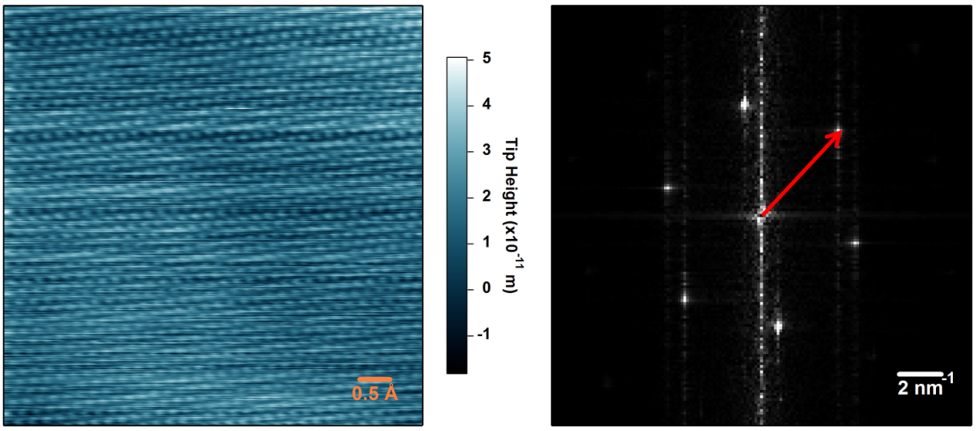

(a) (b)

Figure 5.5: A close examination of the graphite-like lattice discovered on the surface of CaC_6. (**a**) A real-space topographic STM image, recorded at +800 mV sample bias and 50 pA tunnelling current, in which a hexagonal atomic lattice can be seen. (**b**) a FT of the real-space image (a) in which the hexagonal reciprocal lattice vector is marked by a red arrow.

graphite there is no guarantee that the LDOS is the same as undoped graphite (Fig. 4.5). Indeed, even a small amount of doping could shift the Fermi level away from the Dirac point and the presence of unseen subsurface intercalant material or changes in the graphene to graphene layer spacing could have a significant affect on the phonon structure of the material and therefore also on the LDOS. Numerically differentiated spectra (average of 1024 measurements), which were recorded by CITS, from the same surface as Fig. 5.5 are presented in Fig. 5.6. The data were recorded at a set point of +300 mV and 50 pA, $I(V)$ curves were numerically differentiated over a sliding window of five data points in V, for which the data resolution is 1.17 mV, to give conductivity $g(V)$.

Although the atomic lattice was resolved clearly there is a lot of random noise in the topographic imaging (Fig. 5.5b), this same random noise is present in the spectroscopic measurements and appears to obscure any real LDOS features. One piece of information can be resolved, namely that the sample is metallic (non-zero conductivity at zero bias). Other than this there is little to distinguish this measurement from spectra recorded on graphite. However, the spectra is not sharp, nor perfectly symmetrical, so despite a local minimum in conductivity at 0 mV there is no reason to believe that the Fermi level is still at the Dirac point. Random changes in the topographic imaging and the spectroscopy are indicative either of high frequency changes in tip condition (e.g. flakes or atoms joining or falling from the tip, or a blunt tip for which the point of tunnelling constantly changes) or of small amounts of material (such as loose Ca atoms) moving on the surface into and out of the tunnel

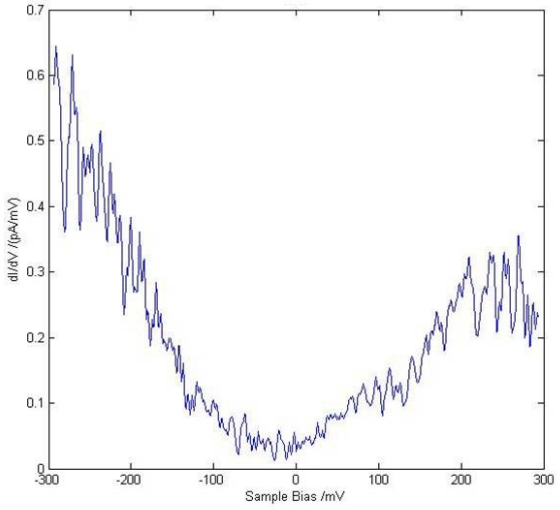

Figure 5.6: Spatially independent, numerically differentiated STS of a graphite-like surface of CaC_6. The spectra exhibits a lot of high frequency noise despite the fact that atomic resolution topographic imaging was achieved. The conductivity at zero bias is finite indicating a metallic surface.

junction. Since the tip is sharp and resolves atoms the latter explanation seems more plausible.

5.4 The expected surface

5.4.1 Definition

The 'expected' CaC_6 surface is identified in STM imaging by the presence of a graphitic lattice, as seen in section 5.3, superposed by an additional $\sqrt{3}a \times \sqrt{3}a$ hexagonal superlattice rotated 30^o from the primary lattice ($R30^o$), as one would expect for the first layer of calcium intercalant atoms. [9] There are also a number of unexpected variants of this CaC_6 surface whereby additional lattices or phenomena are seen. This family of surfaces are introduced and characterised individually in sections 5.5, 5.6 and 5.7. These CaC_6surfaces account for more than 95% of the instances of successful atomic resolution imaging of CaC_6 samples. In the author's experience the majority of these CaC_6 surfaces, by a margin of at least 25:1, are the expected phase. Additionally, just as with non-atomically resolved imaging it is often possible to see interesting surface features such as steps, defects and contaminants.

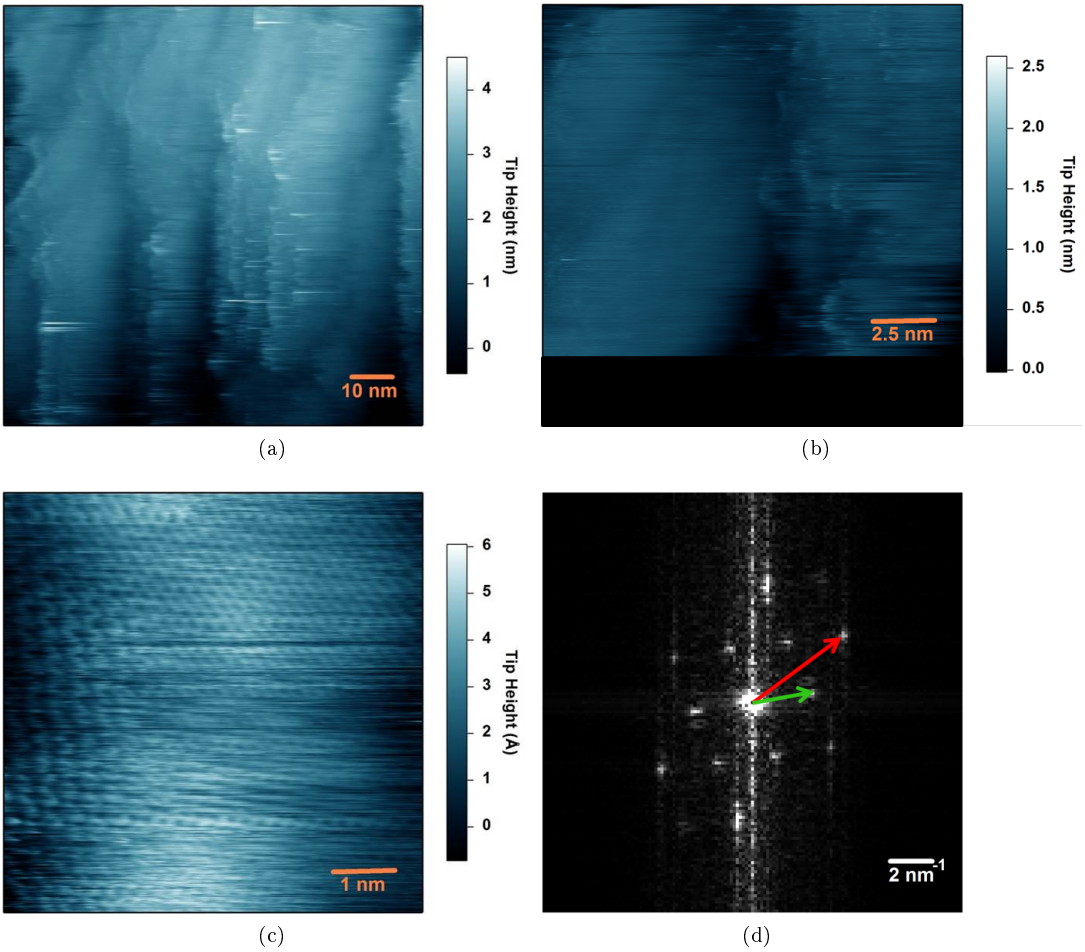

Figure 5.7: Revealing the expected CaC_6 surface by topographic STM imaging. (**a**) A large terraced area of the surface. (**b**) Focusing on one of the flatest terraces. Note that the blackened area of the image is due to a software error when the data was collected. (**c**) Continued reduction of the scan area reveals atomic resolution with an unusual Moiré-like pattern. (**d**) FT of (c) reveals the unusual appearance of the atomic lattice is due to the fact that there are two atomic lattices; a graphitic hexagonal lattice (red arrow) and a $\sqrt{3}$a x $\sqrt{3}$a R30^{o} superlattice (green arrow). All three STM images were recorded at +300 mV sample bias and 50 pA tunnelling current.

5.4.2 Topography and characterisation

An example of the expected phase surface is presented in Fig. 5.7. A large area scan of the surface revealed a number of terraces or flakes which have a flat appearance and a relatively low amount of noise (Fig. 5.7a). The appearance of this large area scan is typical of surfaces which, when imaged at higher resolution, reveal atomical resolution. Smaller scale images revealed the flattest area of the surface to be the flake shown on the left in Fig. 5.7b. Focusing on the flattest area reveals atomic resolution as seen in Fig. 5.7c. It is not entirely clear from the real space STM image what form the atomic lattice takes. The atomic structure appears hexagonal on the right side of the image, much like graphite. However, in the left part of the image the lattice appears larger and slightly perturbed from its hexagonal symmetry. Consequently, the image has the appearance of a Moiré distortion, caused either by interference between two different lattices or with the square lattice of data points recorded by the STM. Additionally, despite the low level of noise seen on the large scale images, at this small scale there is a significant amount of random noise. The true atomic structure is much clearer in the FT, Fig. 5.7d reveals that there are in fact two hexagonal lattices. The primary lattice (marked by the red arrow) is $a = 2.52 \pm 0.02$ Å and the secondary superlattice (marked by the green arrow) is 4.39 ± 0.06 Å R30°. In otherwords, the superlattice is a $\sqrt{3}a \times \sqrt{3}a$ R30° hexagonal lattice, as one would expect from a single layer of the intercalant calcium lattice. Furthermore, the graphitic lattice very closely matches the 2.5 Å spacing expected from bulk CaC_6. [26] Interestingly only half the carbon atoms are seen, as reported for graphite [40] and in section 5.3.2, this is noteworthy as this feature is often attributed to the Bernal stacking arrangement of graphite whereby only the A or B type atoms are imaged and not the others. [114] However, the graphene sheets in CaC_6 are AA-stacked, but similar imaging has been seen before in single-layer graphene [115] and other GICs with AA-stacking arrangements. [31, 32, 116, 117] It has been suggested that this imaging anomaly is in fact of CDW or SDW origin [118], although this has never been verified by experiment. In conclusion, this surface exhibits the correct atomic structure for the expected phase of CaC_6 as defined in section 5.4.1. This is the first reported instance of atomically-resolved imaging of the CaC_6 surface by STM, or indeed any real-space technique.

A second example of the expected phase is presented in Fig. 5.8. In this case AR was found immediately upon approaching the tip to the sample (Fig. 5.8a). Significant amounts of noise were seen initially, although not enough to obscure observation of

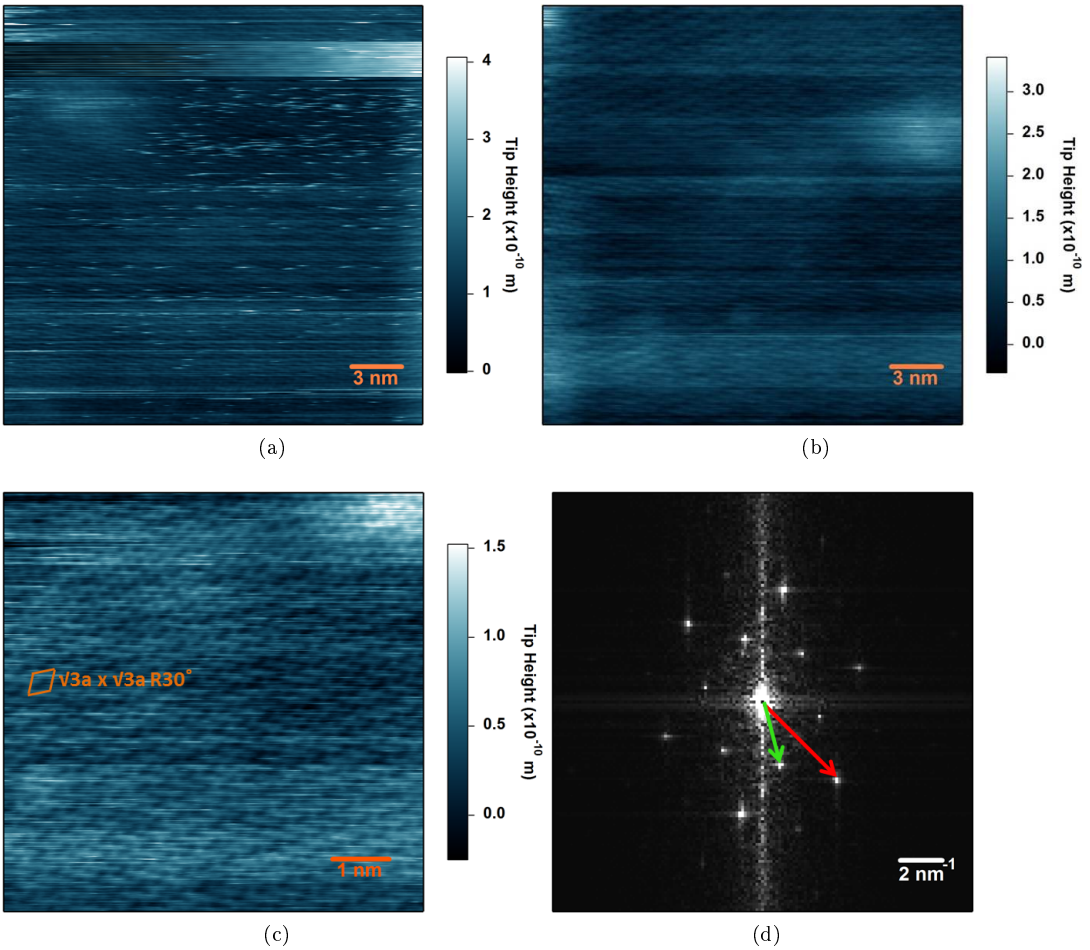

Figure 5.8: Atomically resolved imaging and characterisation of the expected phase CaC_6 surface. (**a**) A noisy topographic STM image of the surface which nonetheless exhibits atomic resolution. (**b**) Another image of the same surface taken at a later time. Significantly less noise is seen, the atomic lattice is still observed. (**c**) A smaller area scan of the same surface reveals that the atomic lattice has the appearance of the CaC_6 unit cell (as shown by orange overlay). (**d**) FT reveals that the surface structure matches the expected phase hexagonal lattice (red arrow) and $\sqrt{3}$a x $\sqrt{3}$a R30^{o} superlattice (green arrow). All images recorded at +300 mV sample bias and 50 pA tunnelling current.

the atomic lattice. The horizontal feature near the top of the image is likely due to a tip condition change, namely some loose material binding to the tip and then falling off or moving away from the tip apex. Over time the noise reduced significantly (Fig. 5.8b) indicating that either the tip or surface had become more stable. The precise nature of the atomic lattices are easier to determine with small area scan such as the one presented in Fig. 5.8c. This image reveals yet again a hexagonal atomic lattice which is clearly perturbed by a superlattice. However, unlike Fig. 5.7c there is no distortion, the image is uniform and consequently the parallelogram-shaped CaC_6 unit cell can be seen (illustrated by the orange overlay). The reason for this difference is not clear, it is possibly due to a difference in tip shape or perhaps a symptom of the fact that Fig. 5.7c was recorded on a highly terraced area of sample where the surface may be more corrugated resulting in the observed distortion. The FT presented in Fig. 5.8d confirms that the surface is indeed a hexagonal lattice with a $\sqrt{3}a \times \sqrt{3}a$ R30º superlattice as expected, consistent with Fig. 5.7d. Note that chronologically Fig. 5.8b was in fact recorded after Fig. 5.8c, in general images are presented in the same order as they were recorded unless otherwise stated.

5.4.3 Related statistics

As discussed, this surface type is the most commonly observed AR surface. The examples provided in Figs. 5.7 and 5.8 are not representative of every such surface encountered. In particular they depict sizable areas ($>$ 50 nm) of flat sample surface where the atomic lattice can be measured, in general this is not always the case. Indeed, in the majority (approximately 75%) of cases where the expected phase is encountered the total area of sample surface upon which atomic resolution is achieved spans less than $10 \times 10\,\mathrm{nm}^2$. A selection of images, each taken on a different surface wherein the expected phase is found, are presented in Fig. 5.9. As before the expected phase is identified by a $\sqrt{3}a \times \sqrt{3}a$ R30º superlattice in FT as seen in Figs. 5.9e and 5.9f. Note that the surfaces are small and noisy, and that distortions of the surface are commonly seen. For these reasons the drift error on the lattice parameters is very large, and the reciprocal space spots are also very broad, particularly for the superlattice, consequently the identification is almost qualitative only. For the purposes of accurately characterising the surface Figs. 5.7 and 5.8 provide a much clearer picture. However, Fig. 5.9 is a better representation of what one is statistically most likely to encounter when imaging the surface. Note that this surface type looks the same in both filled and empty state imaging. The appearance of the atomic lattices

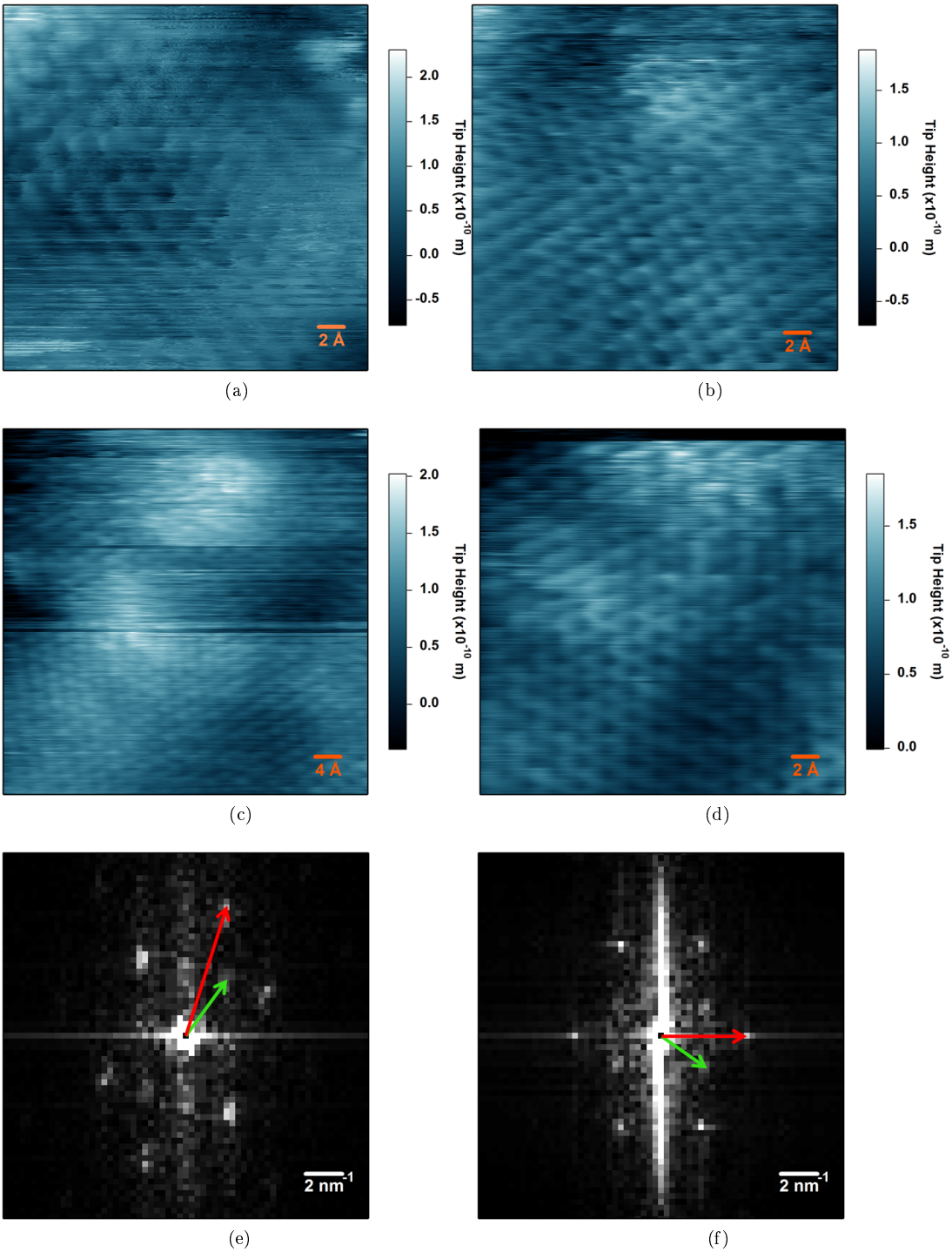

Figure 5.9: Topographic STM images of CaC_6 expected phase surfaces recorded at (**a**) -800 mV, (**b**), (**c**) and (**d**) +300 mV sample bias and 50 pA tunnelling current. Each image is from a different surface. In all cases the atomic lattice is visible but there are significant amounts of noise and distortions. (**e**) and (**f**) are FT images of (b) and (c) respectively. The carbon reciprocal lattice vector is marked by the red arrow and the calcium reciprocal superlattice vector is marked by the green arrow.

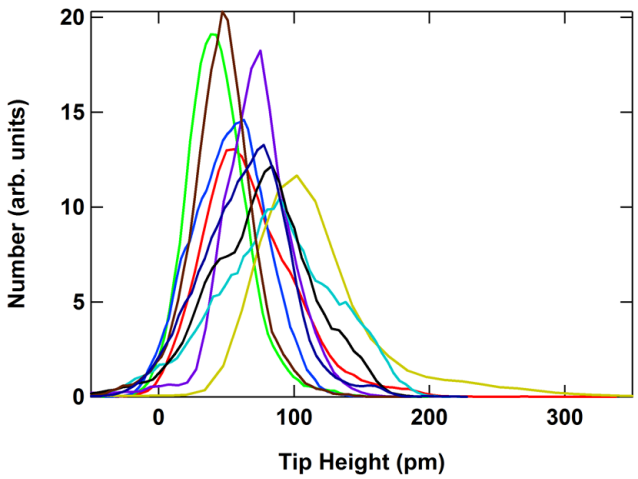

Figure 5.10: Tip height distributions for nine different CaC_6 expected phase surfaces.

do not change with bias or tunnelling current. Although the real-space appearance does vary somewhat from surface to surface indicating a high sensitivity to tip shape or surface flatness.

A graph of the tip height distributions from expected phase surfaces is presented in Fig. 5.10. Each plot is from a different surface and is normalised such that the integral of all the plots are equal. The topographic images selected had no terraces, puddling or other large random features, such that each plot is representative of the roughness of the surface region scanned. Since most of the plots are approximately Gaussian the FWHM value for each distribution is a good indicator of the surface roughness. The lower bound is approximately 75 pm and the upper bound is approximately 150 pm. The different surface conditions observed in Figs. 5.7, 5.8 and 5.9 are reflected in the wide range of roughnesses observed in the height distributions. This inconsistency is also shown in the spectroscopic data measured on this surface (see Section 5.4.4) No correlation was found between surface roughness and specific samples, nor was any correlation found between the appearance of the surface and bias except outside the range $\pm$(300 - 800) mV for which AR is lost and noise or other effects dominate the imaging.

5.4.4 Spectroscopy

Like the topographic imaging spectroscopic images taken on the expected surface type vary significantly from surface to surface. Typically spectra are very noisy and difficult to reproduce, as is reported for the topographic imaging. A selection of spectra, recorded on five different expected phase surfaces, are presented in Fig. 5.11.

All of the profiles presented are the average of 10,000 spectra taken by CITS mea-

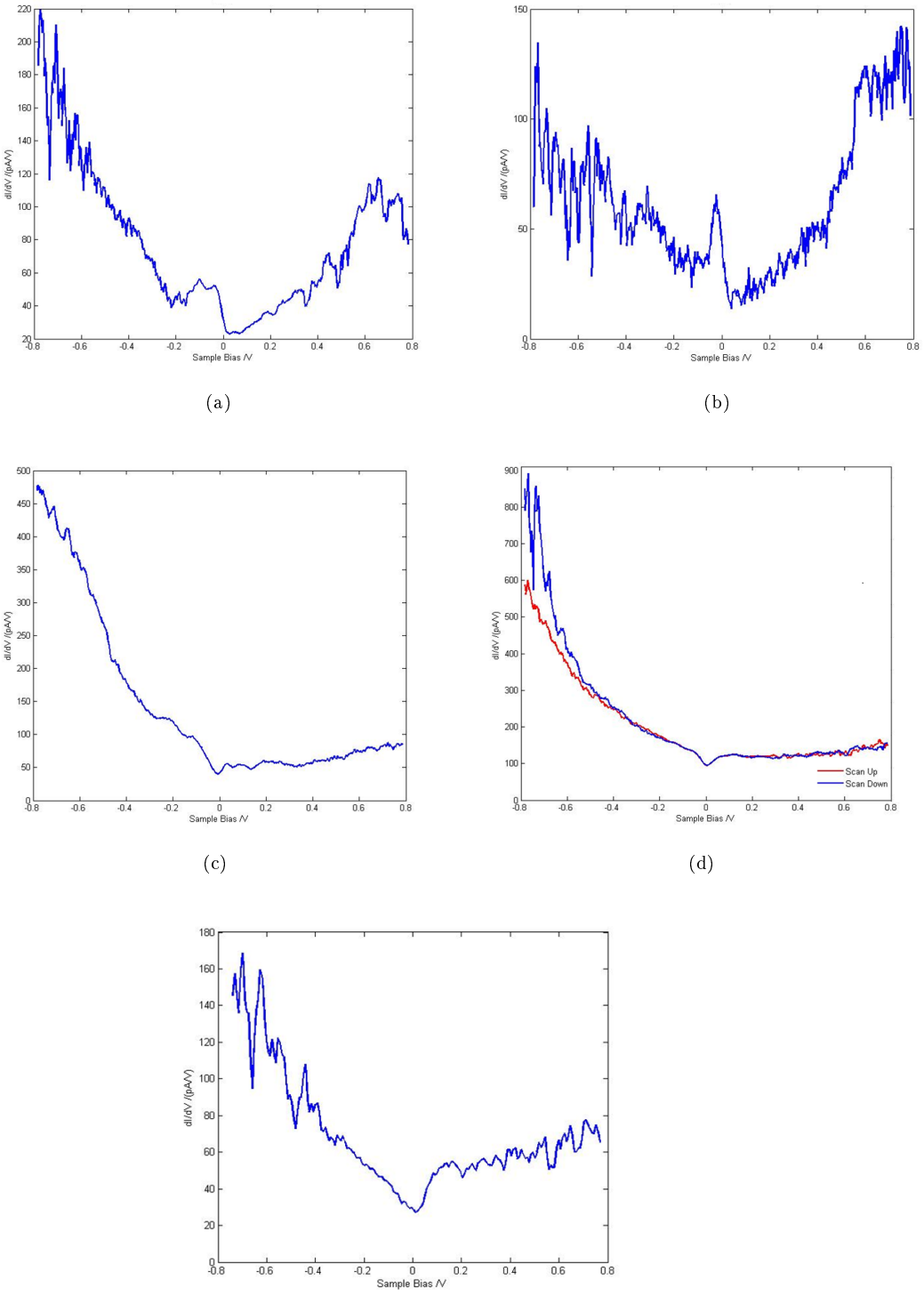

(a) (b)

(c) (d)

(e)

Figure 5.11: Spectra $g(V)$ of CaC_6 expected phase surfaces recorded on five different surfaces. All spectra were recorded by CITS as $I(V)$ with a set point of +800 mV sample bias and 50 pA tunnelling current and then numerically differentiated. It can be seen that the perceived electronic structure is both as noisy and variable in appearance as the topographic imaging for the expected surface type.

surement. In all cases the set point was +800 mV sample bias and 50 pA tunnelling current. Furthermore, all spectra were recorded with a voltage resolution of 3.125 mV (512 data points), with the exception of Fig. 5.11e which was recorded with a voltage resolution of 8 mV (200 data points), and were numerically differentiated over a sliding window of five data points. Note that Fig. 5.11d presents two spectra, these are for two different CITS data sets recorded on the same surface, each of which was recorded and analysed with the same tunnelling conditions and numerical methods.

The five averaged spectra have little in common, exhibiting the same noise and variability as topographic imaging does for this surface type. However, the spectra are universally metallic ($g(0) > 0$) as would be expected for CaC_6. The most reproduced spectra are those presented in Figs. 5.11c and 5.11d (up and down) which are very similar. In all of these cases the spectra is largely featureless except to say that the occupied states appear to have significantly more density than the unoccupied states. However, it is possible that this assymmetry is due to a specific type of tip contamination common to the CaC_6 surface which inhibits tunnelling out of the tip rather than an inherent feature of the surface. The only other feature which appears in more than one spectra is the peak just below the Fermi level (at approximately -100 mV) seen in Figs. 5.11a and 5.11b, and perhaps hinted at in Fig. 5.11c in the form of a shoulder or kink just below the Fermi level at approximately the same energy. This feature is large enough that it is unlikely to be due to noise, also it is clearly not present in raw graphite, as such it is reasonable to say that it may be part of the CaC_6 LDOS, however, it is not clear which states or real space features it is associated with nor why it does not appear in some of the other spectra.

5.5 Triple-superlattice surface

5.5.1 Topography and characterisation

The first surface type derived from the expected phase is the *triple-superlattice* phase. This particular surface type was encountered only once, therefore the data presented in this section is a near-exhaustive collection of all data collected from this particular surface. As the name suggests the defining characteristic of this surface type is that it exhibits an unusual superlattice whereby three superlattice peaks are seen in reciprocal space, rather than one. The apparent rarity of the surface might lead one to consider it a spurious, random anomaly. However, there is a striking similarity between this surface type and an unexplained CaC_6 phase measured by X-ray scat-

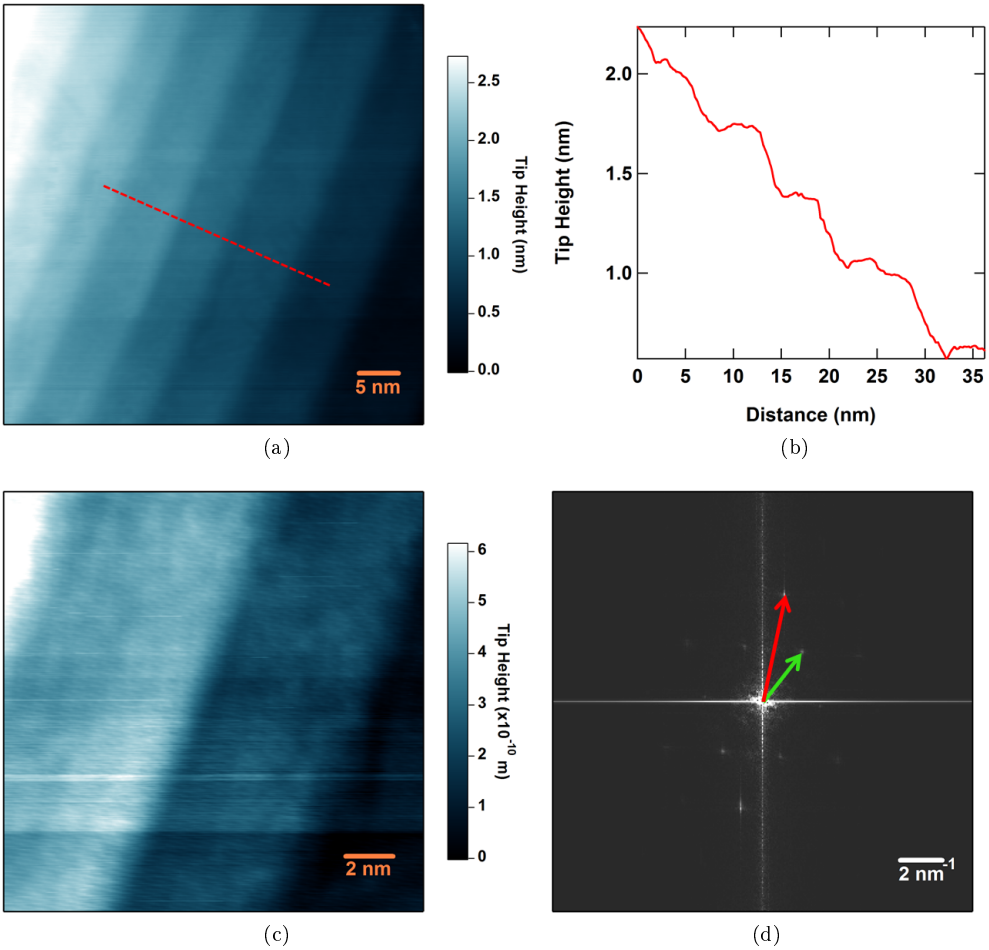

Figure 5.12: Discovering atomic resolution imaging on a terraced CaC_6 surface. (**a**) A highly terraced region of CaC_6 surface as seen in topographic imaging at +300 mV sample bias and 50 pA tunnelling current. (**b**) A line profile showing the step heights on the surface as marked by the red line in (a). (**c**) A topographic image taken in the middle of the region shown in (a), image recorded at +800 mV sample bias and 50 pA tunnelling current. Atomic resolution is dimly visible in this image and the terraces have a very low roughness. (**d**) A FT of image (c) reveals that both a graphitic lattice (red arrow) and a $\sqrt{3}a \times \sqrt{3}a$ R30^{o} superlattice (green arrow) are detected.

tering experiments. [119] In X-ray scattering the additional peaks associated with this phase have 1% of the intensity of the primary expected phase peaks, this may explain why this surface type was encountered only once.

Fig. 5.12a presents a highly terraced region of a CaC_6 surface. Unlike Figs. 5.1 and 5.2 this surface appears very stable and there is little noise, in particular there is no mobility or noise near, the step edges. A profile of the step edges, as marked by the red line in Fig. 5.12a, is shown in Fig. 5.12b. As with other surfaces the step heights fall in the 3 - 6 Å range. A second topographic image showing a closer view of two of the largest steps is given in Fig. 5.12c. This image once again shows the remarkably low level of noise and the flatness of the terraces is such that atomic resolution can be dimly seen, although the number of pixels per unit cell is low. Consequently, the

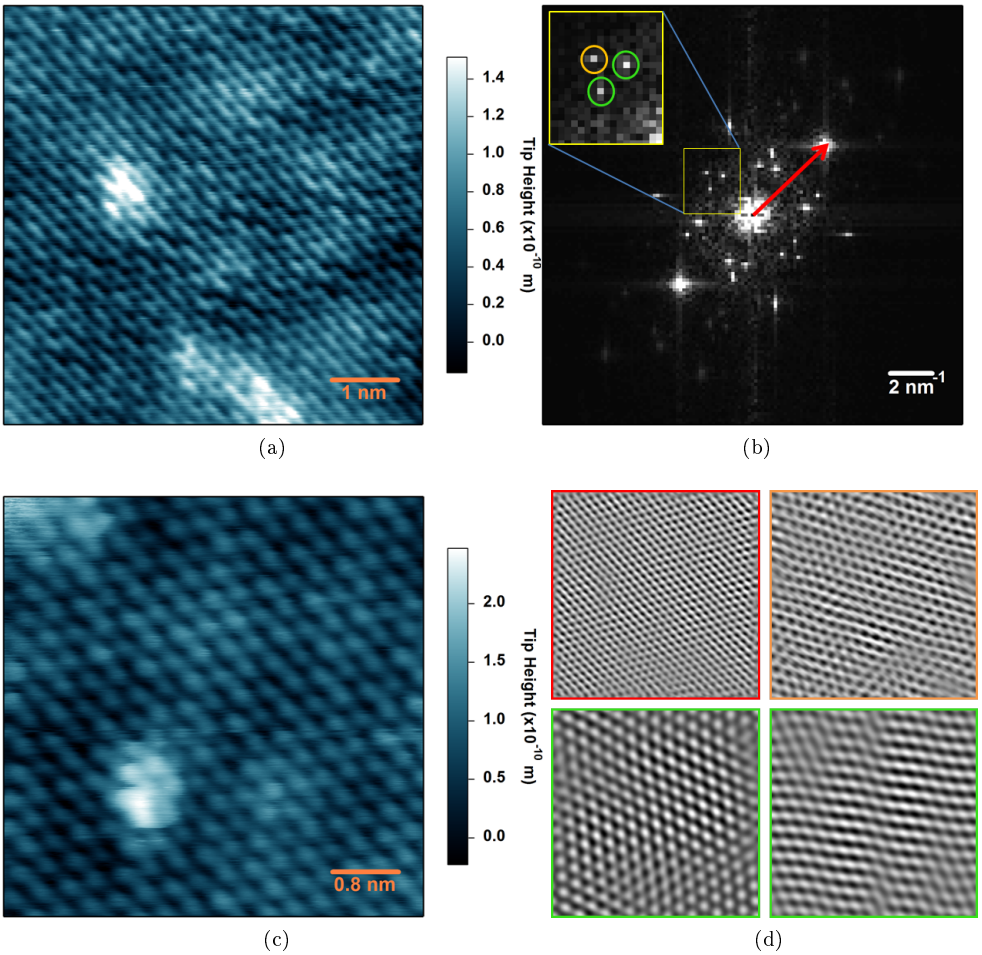

Figure 5.13: Revealing the triple-superlattice phase of CaC_6. (**a**) A topographic STM image. Initially the surface appears to match the expected phase. However, (**b**) FT reveals three superlattice spots instead of one, none of which exactly match the expected $\sqrt{3}a \times \sqrt{3}a$ R30^o intercalant lattice. (**c**) Upon closer inspection the carbon lattice is easily visible in real space, but the superlattices are not. Both STM images recorded at +300 mV sample bias and 50 pA tunnelling current. (**d**) Images filtered to show each of the four lattices marked in (b) only, colour co-ordinated to match the colours assigned in the FT image.

reciprocal lattice peaks are revealed in the FT image (Fig. 5.12d) but the signal to noise ratio is low. Nevertheless, a graphitic lattice (marked by the red arrow) is seen, as is a hexagonal superlattice (marked by the green arrow).

A closer look at the largest of the terraces reveals atomic resolution which is clear to the see, even in real space (Fig. 5.13a). Qualitatively this surface looks very similar to the expected phase surface seen in Fig. 5.8, although somewhat flatter and less noisy. However, FT reveals that the surface is in fact very different. Fig. 5.13b reveals that unlike the expected phase there is no visible $\sqrt{3}a \times \sqrt{3}a$ R30^o superlattice of Ca atoms. Instead we see the carbon lattice $a = 2.5 \pm 0.3$ Å, marked with the red arrow, and three hexagonal superlattices, marked in the inset. It is now apparent that the

single lattice appearance in Fig. 5.12d is due to the fact that the image the FT is calculated from is too large, i.e. there is insufficient spatial resolution to distinguish the three superlattices from each other. The two superlattices circled in green both measure 4.4 ± 0.1 Å, very closely matching the expected $\sqrt{3}a \times \sqrt{3}a$ superlattice. However, neither of the green superlattices have the correct R30° orientation. In fact, the third superlattice point, circled in orange, is at the R30° position. However, in this case the superlattice is much smaller than the expected phase superlattice, measuring 3.6 ± 0.1 Å.

A closer look at the surface topography shows that the visible structure is predominantly the carbon lattice (Fig. 5.13c), this (together with the very low noise levels) may indicate that the surface is terminated in a graphene sheet, rather than a (partial) intercalant layer. It is clear however that there has been some subtle tip condition change between Figs. 5.13a and 5.13c as the appearance of the atomic lattice in the former is slightly different between the two (i.e. the surface in Fig. 5.13a does not resemble the carbon lattice alone). There is a lot of anomalous contrast on the surface even though it is very flat, this may perhaps be some sort of interference between the many superlattices or an indication that there are defects below the surface which are not directly visible. In ordinary graphite it has been shown that defects can be seen up to ten layers below the surface. [120] The bright defect seen in both images is the same surface feature, in Fig. 5.13c it can be seen that it is exactly one hexagon of seven carbon atoms in size and appears to stand 1 Å above the surface. This may indicate that it is a very small island of atoms or that it may simply be a localised electronic effect whereby additional density of states are seen.

A reverse FT is performed on each reciprocal lattice in Fig. 5.13b in order to generate a real-space image of each of the four different lattices (see Fig. 5.13d). The carbon lattice (red bordered image) has the expected graphitic hexagonal appearance, closely resembling the surface as seen in 5.13c. The two large superlattices (green bordered images) both appear very much like a calcium lattice, i.e. a hexagonal lattice of atoms which are large compared with the carbon atoms, however, neither of these lattices is obviously visible to the human eye in the topographic images. The anomalously small superlattice (orange bordered image) is again hexagonal, however, the lattice does not have the appearance of atoms, but rather that of a network or web of points. The physical significance of this is not clear, but it may explain why Fig. 5.13a also shares this property. This tells us that the contribution of this superlattice or signal is significant to the appearance of the topographic image.

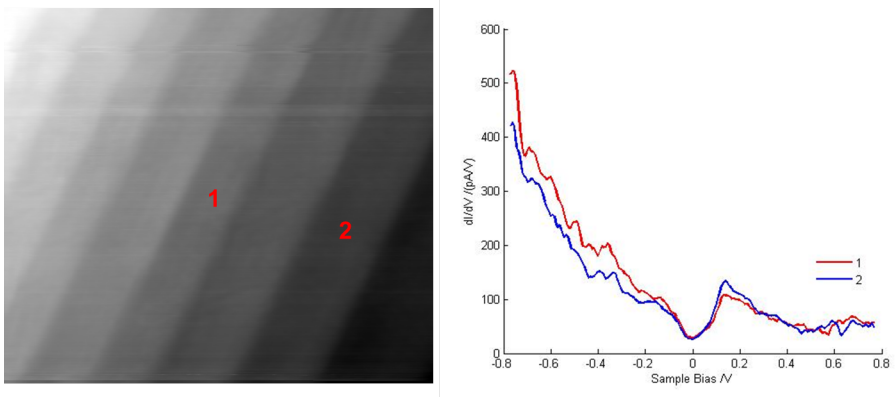

Figure 5.14: Numerically differentiated STS curves $g(V)$ recorded on two different terraces of the triple-superlattice surface. The spectra were recorded at +800 mV sample bias and 50 pA set point and averaged over 15 measurements for each terrace. Numbered spectra were recorded on the correspondingly numbered terrace.

5.5.2 Spectroscopy

The unique nature of the this surface was not apparent until Fourier analysis revealed the additional superlattice peaks. Consequently, only STS data was recorded for this surface type. The STS measurements were made on the highly terraced surface presented in Fig. 5.12, specifically measurements were made on two of the terraces as shown in Fig. 5.14.

Spectra from both terraces are approximately the same, each exhibiting metallic behaviour ($g(V) > 0$), greater density in filled states than empty states, a slight shoulder or kink in the LDOS at -100 mV, and a notable peak just above the Fermi level at approximately +175 mV. Terrace 1 exhibits greater density in filled states, whilst the small peak in LDOS present just above the Fermi level is more developed for terrace 2. Both of the spectra share similar characteristics to Fig. 5.11e, one of the CITS data sets recorded on the expected phase. In particular the general assymmetry of filled and empty states and the peak at +175 mV are reproduced. However, the kink in LDOS seen at -100 mV is shared with Figs. 5.11a and 5.11b.

This indicates that spectroscopically the triple-superlattice surface matches the expected phase very closely. Given the fact that topographic imaging was considerably more stable and less noisy for the triple-superlattice surface than for the expected phase one may consider the spectra given in Fig. 5.14 to be a more reliable indication of the true LDOS for the CaC_6 surface. Indeed, the triple-superlattice surface LDOS appears to unite the different features of the spectra presented in Fig. 5.11 for the expected phase. It appears that the poor tunnelling conditions typically encountered for the expected phase obscure features of the LDOS. Were one able to record spectra

without such interference one may expect to see a combination of all of the features shown in Fig. 5.11 in the expected phase LDOS, as seen here for the triple-superlattice phase.

5.5.3 Origin of superlattices

It is difficult to reconcile this apparent surface structure with any meaningful CaC_6 structure. In particular, the small superlattice, marked in orange, does not form any commensurate structure with the known CaC_6 unit cell. It is clear that the graphene layer displays no phase boundary, however it is possible that the intercalant lattice has some sort of interface which is not readily apparent in the topographic image. For example, we are already aware that during the intercalation process calcium atoms enter the graphite host via galleries and defects forming puddles of CaC_6 which expand across the host (see Section 3.2.3 and [91]), therefore it is possible that a single graphite crystal layer may be intercalated from multiple points during this process. Consequently, once the crystal is fully intercalated the various puddles which are formed must eventually connect. If two such puddles have different lattice configurations (namely α, β or γ) then perhaps the interface where puddles meet exhibits structural mismatches which have modulated interatomic distances or orientations (e.g. as seen for Si(111) in Fig. 4.1). If the surface area shown in Fig. 5.13a were above such an interface it could explain the superlattice anomalies. A second possibility is that one or more of the superlattices are an artefact caused by proximity to a step edge, such effects are reported in topographic imaging of many samples, including unintercalated HOPG. [121]

5.6 Stripe phase surface

5.6.1 Introduction and Topography

The second type of surface derived from the expected phase is the *stripe phase*. This surface exhibits the expected phase structure, with an additional 1D charge modulation superposed upon it. The topographic appearance of this surface type was found to be highly bias-dependent, in stark contrast to all the other surface types reported thus far. The data presented will also show the remarkable flatness, stability, low noise and repeatability of spectroscopic measurements on this surface type. The high stability of this surface meant that tip condition changes were very rare, indicating a very low level of loose surface material interacting with the tip or tunnelling junction.

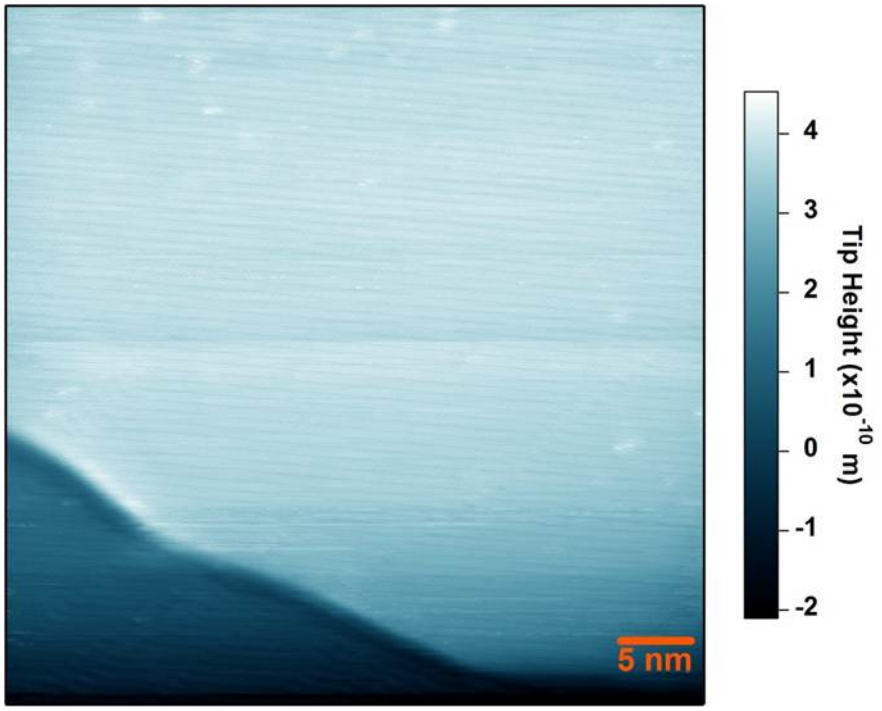

Figure 5.15: A topographic STM image of CaC_6 recorded at +300 mV sample bias and 50 pA tunnelling current. The image reveals a large surface covered with horizontal stripes both above and below a step edge.

A single tip condition change was observed and a note will be made to distinguish data recorded before and after this change. Data will be presented in the chronological order in which it was recorded unless otherwise stated.

The stripe phase was first encountered in topographic STM imaging directly following a new tip-to-sample approach. The first topographic STM image recorded can be seen in Fig. 5.15. This particular image is too large to distinguish atomic structure, however, a number of interesting features are immediately apparent. Stripes can be seen running horizontally across the image, importantly these stripes differ from those shown in Fig. 5.1a in that they are larger that atom-scale (they appear 1 - 2 nm in size from this image) and are remarkably well defined and noise-free. Furthermore, the stripes are seen above and below the step edge seen near the bottom of the image, and importantly the stripes do not cross through the step, which is what one would expect for a noise effect. Whilst the stripes are mostly linear and continuous there are a few instances of discontinuities which look a little like waves, the most visible examples can be seen below the step edge. Note also that many bright spots can be seen scattered throughout the image. Interestingly these appear to be very stable, no noise or switching is seen, nor do they appear to cause tip condition changes or interfere with the tunnelling junction. Therefore it is unlikely that these are contaminant atoms on the surface, as it is clear that loose intercalant atoms cause a lot of noise,

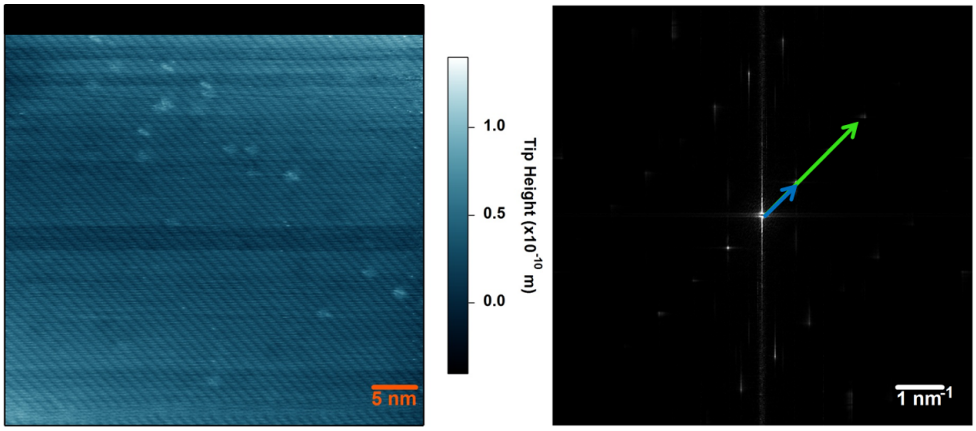

(a) (b)

Figure 5.16: The remarkable flatness of the stripe surface shown in (**a**) topographic STM imaging recorded at +300 mV sample bias and 50 pA tunnelling current. Atomic resolution is faintly visible, as are a number of bright spots or defects. (**b**) A FT reveals reciprocal lattice peaks for the stripe (blue arrow) and calcium lattice (green arrow).

as seen in Section 5.4. These defects are only seen on this surface type raising the possibility that they are either a requirement for the formation of the stripe phase, or that they are symptomatic of it. In this instance stripes were found to cover at least 300 nm of the surface in both x and y directions, with no significant change in the surface properties over this region. It is possible that the stripe surface extended significantly beyond the region scanned but in the interests of not risking tip contamination this was not checked.

In order to ensure the stripes are not a scan artefact the scan direction was rotated 45° such that the stripes are not parallel to the fast scan direction.. This also moved the tip away from the step edge, the resultant image is shown in Fig. 5.16a. The stripes are once more visible and are rotated as expected, but in this image some texture caused by imaging of the atomic lattice at the limit of resolution can be seen. Furthermore, the bright spots and defects are seen once again, as are darkened or depressed areas throughout the image. Note the remarkable flatness of the surface, even across a relatively large area for STM imaging. Fig. 5.16b presents the FT image for which a hexagonal lattice measuring 0.4 nm is marked by a green arrow. At this image size the sampling rate is one pixel per 0.1 nm, therefore a large error is expected, the green arrow likely matches the intercalant lattice. In order to resolve a lattice critical sampling of four data points per unit cell in x and y is required, consequently it is not surprising that the carbon lattice is not seen in this image. Additional reciprocal lattice peaks can be seen throughout Fig. 5.16b, these correspond to the stripe. The primary reciprocal lattice vector of the stripe is marked by the blue arrow.

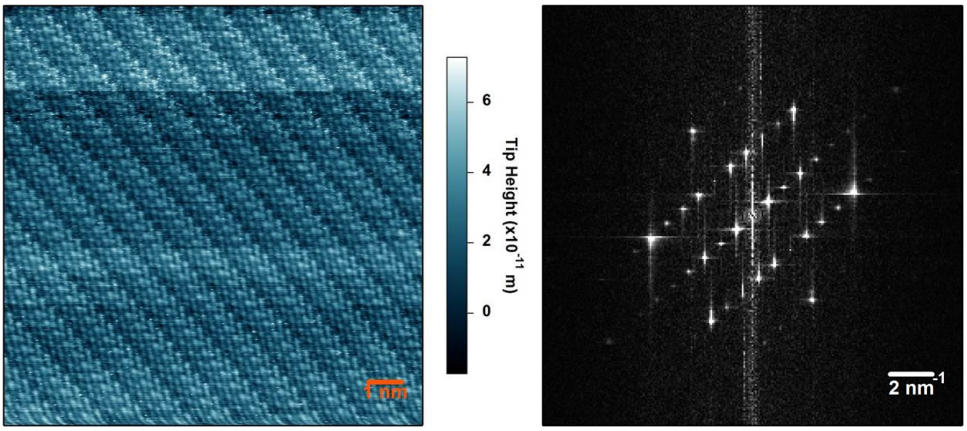

(a) (b)

Figure 5.17: Closer examination of the stripes reveals the presence of both the carbon and calcium lattices. (**a**) A topographic STM image of the stripe phase recorded at +300 mV sample bias and 50 pA tunnelling current. (**b**) A FT image revealing the carbon lattice, calcium lattice and the stripe periodicity are all present.

The other additional peaks are satelite peaks of the stripe periodicity around the calcium lattice peaks, i.e. $\pm nq_{Ca} \pm mq_{Stripe}$ where q_{Ca} and q_{Stripe} are the reciprocal lattice vectors of the calcium superlattice and stripes respectively and $n, m \in \forall\mathbb{N}$. As discussed in Section 4.1.3, the hexagonal Bravais lattice is rotated 30°. This means the stripe periodicity in real space is orientated at 30° to one of the calcium superlattice directions, this means that the periodicity of the stripes share one of the carbon lattice directions in real space.

A second, smaller topographic STM image of the same area is provided in Fig. 5.17a. This image has sufficient spatial resolution to reveal the carbon lattice and calcium lattices, as well as the stripe periodicity. The carbon lattice and calcium superlattice have comparable topographic height, consequently the atomic structure of the surface is somewhat confusing to look at by eye. This also results in a very complicated FT (Fig. 5.17b) where the reciprocal lattice vectors for all three periodicities are seen, in addition to numerous satelite peaks $\pm nq_{Ca} \pm mq_{Stripe} \pm lq_C$ where q_C is the reciprocal lattice vector for the carbon lattice and $n, m, l \in \forall\mathbb{N}$. A more detailed analysis of the surface structure is made in the next subsection (5.6.2).

5.6.2 Characterisation and crystallography

This subsection includes a detailed analysis of the physical nature of the stripe phase surface. In order to properly characterise the surface it is important to select data which is self-consistent. Tip condition changes can have a significant impact on the qualitatitive appearance of a surface and changes in the surface appearance with

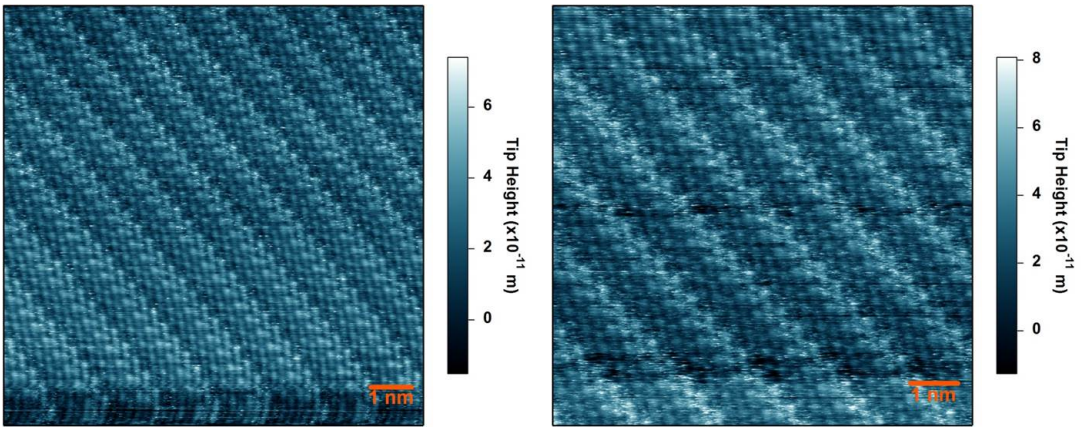

(a) (b)

Figure 5.18: CaC_6 stripe phase as seen in topographic STM imaging (**a**) before and (**b**) after a tip condition change. Both images recorded at +300 mV sample bias and 50 pA tunnelling current.

changing tunnelling conditions (see Section 4.3.2). An example of this effect is given in Fig. 5.18. In this figure the CaC_6 stripe phase is shown as seen in topographic STM imaging before and after a tip condition change. Both images are recorded at identical tunnelling conditions, 300 mV sample bias and 50 pA tunnelling current, therefore all differences between the two images are due only to the change in tip condition. All data is presented in the chronological order in which it was recorded, therefore all data presented thus far was recorded using the tip configuration shown in Fig. 5.18a and all data presented from this point on, including all the CITS measurements, were recorded with the tip in the configuration shown in Fig. 5.18b. The primary difference between the two tip states is the difference in energy at which the Ca lattice becomes visible in real space topography. Before the change the Ca lattice is fully visible in real space at +300 mV, however, after the tip change the Ca lattice is no longer easily visible at this energy and one must increase the sample bias to +400 mV in order to see the Ca lattice as clearly. The fact that the carbon lattice is always visible at all voltages, but the superlattice can be tuned out of the topographic image by changing sample bias is an indication that the Ca superlattice atoms are below the surface, i.e. that the surface is terminated in a graphene sheet. This would also be consistent with the fact that the surface appears stable and tip condition changes are extremely rare. If the Ca lattice occupied the top surface of the sample one would expect Ca atoms, which are loosely bound, to hop on and off of the tip resulting in changes of tip shape and conductivity which would manifest in continuous changes in imaging, and noise caused by extension and retraction of the tip by the feedback loop.

This bias dependence of the appearance of the Ca lattice can also be seen in Fig.

5.19. The first panel, Fig. 5.19a, presents the CaC_6 stripe phase surface as recorded at 300 mV sample bias and 50 pA tunnelling current. At these tunnelling conditions only a single hexagonal lattice of atoms can be seen by eye, namely the carbon lattice, superposed by a long-range 1D stripe modulation. When the sample bias is increased to +400 mV, as seen in Fig. 5.19b, a second hexagonal lattice of atoms also becomes visible. This second lattice has a larger period and the atoms themselves are also larger in size, furthermore the lattice is rotated 30° with respect to the carbon lattice. This matches the expected appearance for the Ca superlattice: the covelant radius of carbon is 77 pm and the ionic radius for Ca^{2+} is 100 pm - note that the Ca atoms may not in fact be in a full 2+ ionic state, as only 1.2 electrons per unit cell are known to be donated from the Ca atoms to the graphitic π^* bands [35, 34], but 100 pm is a decent approximation of the expected ion size and is consistent with what is seen in the image. In short, at +400 mV sample bias the surface appears to match the expected phase surface structure but with an additional long-range 1D stripe. Fig. 5.19c presents an FFT of the stripe surface recorded at +300 mV sample bias. Despite the fact that the superlattice is not distinguishable by eye in the real space topographic image q_{Ca} is clearly present in the FFT image as indicated by the blue arrow. The primary lattice reciprocal vector q_C and the reciprocal vector for the stripe period q_{Stripe} are also indicated by red and green arrows respectively. The chosen q directions match the respective coloured lines in Figs. 5.19a and 5.19b, in the case of hexagonal lattices FT causes a rotation of 30º, this is important to note when comparing symmetries in Fourier space. The remaining unlabelled peaks belong to the group $\pm nq_{Ca} \pm mq_{Stripe} \pm lq_C$ where $n, m, l \in \forall\mathbb{N}$ as explained in Chapter 4. Importantly this establishes that the superlattice does not disappear at +300 mV sample bias, but that its topographic contribution is finite and extremely small.

The stripes have a periodicity of 1.125 nm in one of the carbon lattice directions and are commensurate with both the carbon and superlattice. In Fourier space $q_{Stripe} = \frac{1}{3}q_{Ca}$ as such the unit cell for the stripe phase is tripled in one of the Ca lattice directions with respect to the expected phase unit cell. Consequently, the new unit cell is $3\sqrt{3}a \times \sqrt{3}a$ R30° (1.299 nm × 0.433 nm) where the carbon lattice unit cell $a = 0.25$ nm. This new stripe phase unit cell is overlayed in orange in Fig. 5.19b.

The final panel, Fig. 5.19d, presents topographic line profiles recorded from carbon symmetry directions, as seen in the correspondingly coloured lines in Fig. 5.19a, and superlattice symmetry directions, as seen in Fig. 5.19b. The superlattice atomic corrugation for the stripe phase is approximately 0.020 nm that is much lower than

the X-ray-measured C–Ca distance of 0.226 nm [26] and the Ca^{2+} ionic radius of 0.100 nm, providing further evidence that the Ca atoms are sub-surface and that the surface is graphene-terminated as discussed earlier. The modulation of the stripe can be seen in all of the line profiles with the exception of the line measured parallel to the stripes (yellow), in all cases the peak to trough amplitude of the stripe period is less than 0.040 nm which, together with its sine-wave shape, indicates an electronic nature rather than a physical one. The stripe phase surface is in general extremely flat, especially when compared to the other surface types reported in this chapter. It is believed that this remarkable flatness and low noise indicating low levels of contaminants and surface materials and a graphene-terminated surface may be crucial for stabilising the stripe phase. In other conditions the stripe may simply not exist. These stringent conditions for formation and/or observation of the stripes may explain their relative scarcity when compared to the expected phase surface type. The difference in surface roughness between the two surface types is also evident from the height histograms presented in Fig. 5.20. The stripe phase exhibits FWHM surface roughnesses of less than 50 pm, but the expected phase typically has at least double the FWHM surface roughness. Furthermore, the roughness of the stripe phase does not change significantly between different areas, but the expected phase shows significantly more variation for different surface regions, as already observed. Also, the appearance of the stripe surface varies with bias (for example, Figs. 5.19a and 5.19b), but this has a negligible effect on the surface roughness observed. In addition to this, it should also be noted that in all cases the stripe phase had a finite lifetime. On all surfaces for which the stripes were observed, the stripe phase eventually transformed into the expected phase. This was a one-way process and the stripe phase had a life span of 4–36 hours. In the event of this transformation, STM resolution was lost for a short period (about 5 mins) after which the expected phase was resolved and the topographic height variation of the surface approximately doubled. The reason for this finite lifespan is not evident but the possibility that STM scanning destabilises the surface is not discounted, e.g. as seen in 1T-TaS_2. [122] The profiles along the carbon lattice directions show no observable in-plane distortion from the ideal lattice configuration and no out-of-plane modulation of the atomic corrugation other than the stripe itself. Similarly, the Ca lattice exhibits no unexplained out-of-plane modulation. However, the profile taken in the Ca symmetry direction crossing the stripes (marked in green in the figure) shows some in-plane anomalies, this motivated a more detailed structural analysis of the atomic lattices.

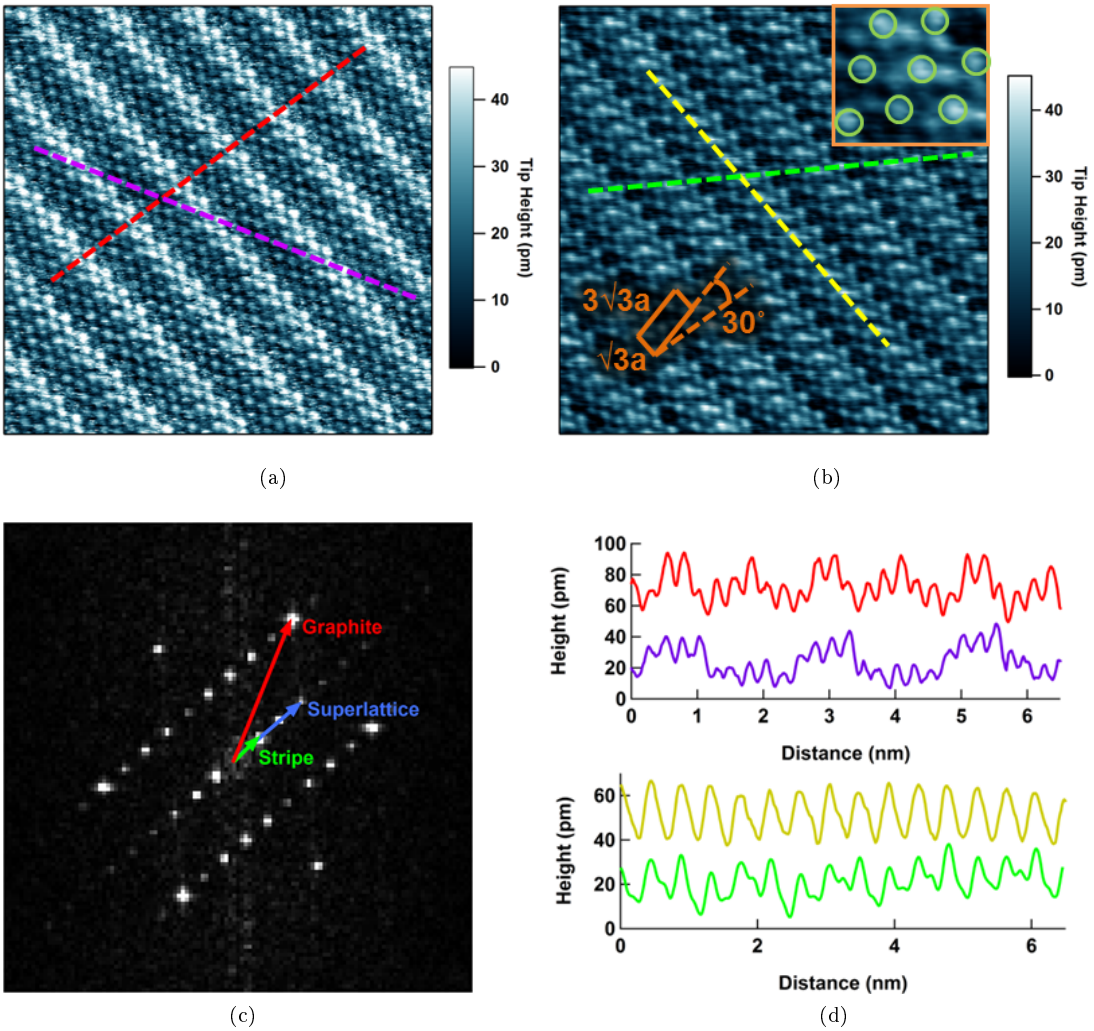

(a) (b)

(c) (d)

Figure 5.19: Preliminary analysis of the stripe surface using 7 nm × 7 nm topographic STM images recorded at (**a**) +300 mV and (**b**) +400 mV sample bias and 50 pA tunnelling current. Both images display a stripe surface with one-dimensional, 1.125 nm period, modulation. In image (a) only the hexagonal carbon lattice ($a = 0.25\,\text{nm}$) is visible whereas in image (b) both the hexagonal carbon and a hexagonal superlattice ($\sqrt{3}a \times \sqrt{3}a$ R30^o) can be seen. In each image two lines are marked, these lie along carbon lattice directions (red and purple) and superlattice directions (green and yellow). Inset in image (b) is the stripe phase unit cell marked in orange, which is triple the size of the standard CaC_6 unit cell, and inside the orange square a zoomed area with the Ca atoms circled in green, uncircled atoms are carbons. (**c**) FT image computed from (a) demonstrating that despite the low real-space contrast the superlattice is detectable, as is the primary carbon lattice as well as numerous satelite peaks rising from the stripe and the superlattice. The reciprocal space vectors for the stripe, carbon and superlattice (q_{stripe}, q_C and q_{Ca}) are marked by green, red and blue arrows respectively. (**d**) Line profiles colour-matched to the lines marked in images (a) and (b). The orange overlay in parts (a) and (b) represents the new stripe phase unit cell.

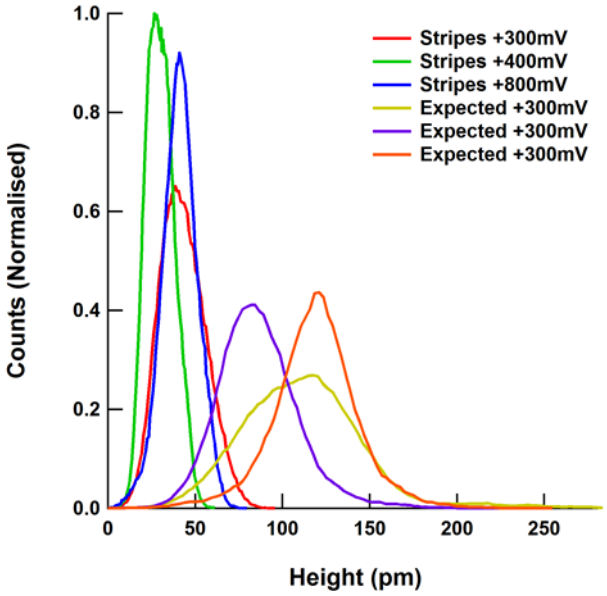

Figure 5.20: Topographic height distributions for STM images recorded on stripe phase surfaces and expected phase surfaces. The type of surface and sample bias used for the measurements are indicated in the legend.

Structural characterisation of the superlattice and graphene lattice are presented in Figs. 5.21 and 5.22 respectively. As already discussed the superlattice is less prominent in real-space topographic imaging at 300 mV than it is at 400 mV, this allows the two lattices to be identified and analysed individually with real-space images. Fig. 5.21a is a drift-corrected (see Section 4.3.3 for details) version of Fig. 5.19b. An overlay (shown in yellow in Fig. 5.21a) connects a set of Ca atoms. The distortion of this overlay from the ideal hexagonal shape illustrates the perturbation of the Ca lattice from its ideal configuration as detected by the line profiles. The perturbation is due to a systematic distortion of the Ca lattice whereby every third row of Ca atoms parallel to the stripes is shifted in the positive x-direction. To quantify this, three distinct rows of Ca atoms are labelled: A, B and C which correspond to atoms below, coincident with and above the bright region of the stripe, respectively. By cross-correlating matching line profiles taken from these positions, as shown in Fig. 5.21b, a 0.06 $\pm$ 0.02 nm shift in the positive x-direction of the B Ca atoms, that is, those co-incident with the peak of the stripe, from their ideal lattice position with respect to the A and C atoms is found. The distortion of the Ca lattice is an in-plane transverse wave only. Fig. 5.21c is a schematic illustrating the new structure, the B Ca atoms can be seen to be shifted in the positive x-direction away from the centre of the graphene hexagons.

Similar analysis did not reveal any distortion in the carbon lattice: Fig. 5.22 presents a cross-correlation analysis of the carbon atom positions in the stripe direc-

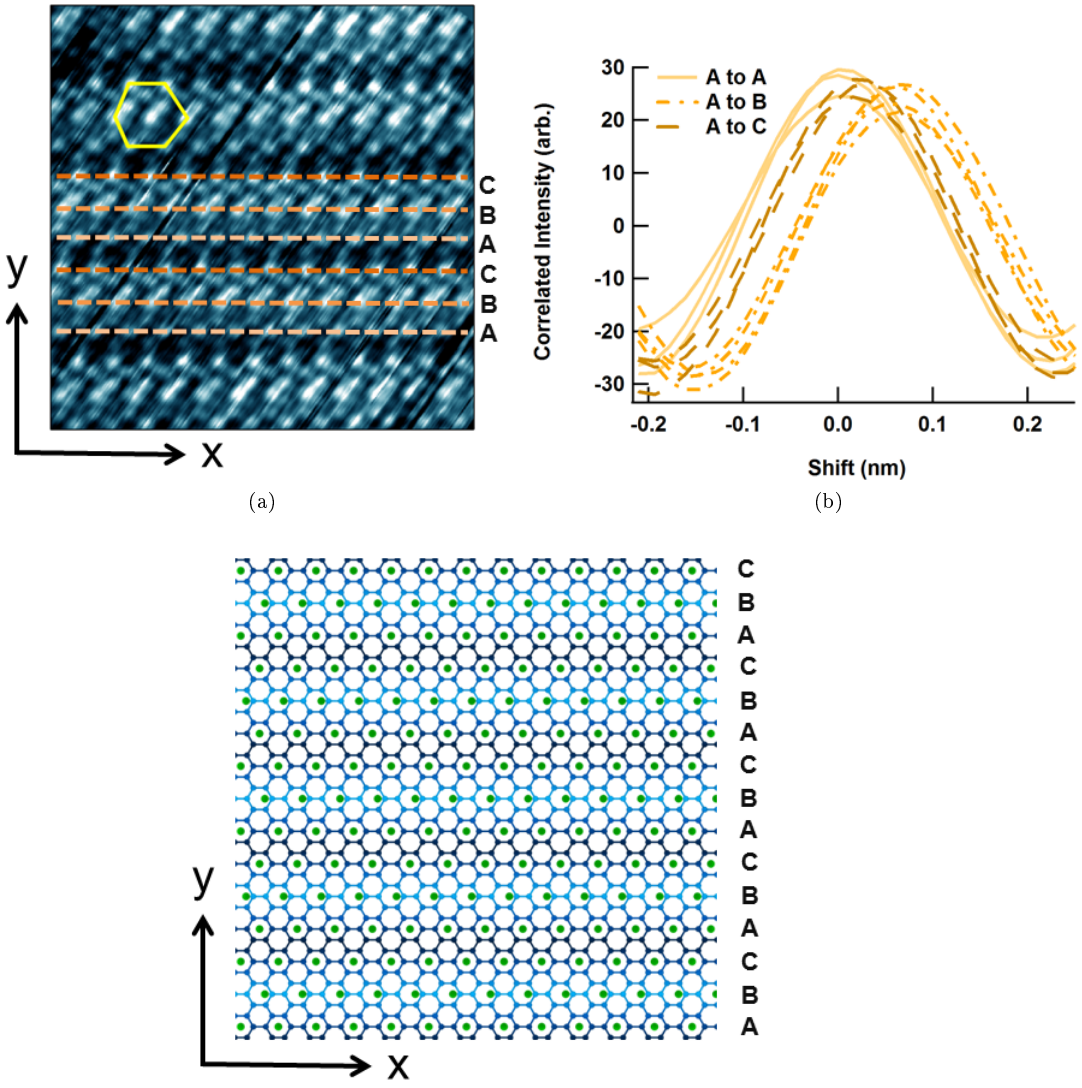

(a) (b)

(c)

Figure 5.21: Analysis of the surface structure and broken symmetry of the Ca superlattice. (**a**) 5 nm × 5 nm drift-corrected topographic STM image with line profiles in the Ca-parallel-to-stripe symmetry direction marked on [B] and off [A, C] the stripe apex. (**b**) Correlation of line profiles shown in (a) demonstrate a 0.06 ± 0.02 nm perturbation of the Ca atoms on the stripe apex. (**c**) A schematic illustrating the distortion of the Ca lattice (green) and the resultant stripe modulation (blue scale) on the graphene sheet as seen in positive sample bias imaging oriented to match (a).

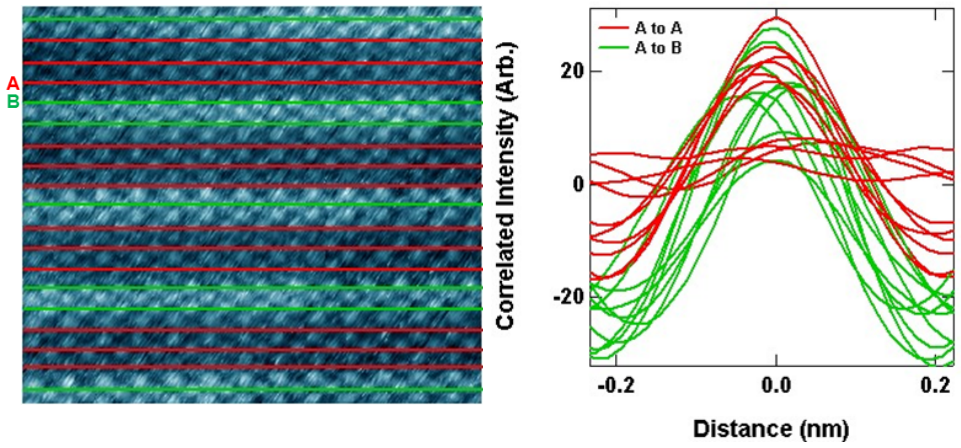

(a) (b)

Figure 5.22: Structural analysis of the carbon lattice. (**a**) Drift corrected and reorientated topographic STM image recorded at +300 mV with off-stripe [A] and on-stripe [B] line profiles marked in the graphitic (110) direction . (**b**) Cross-correlation of line profiles shown in (a) displaying no systematic distortion in the graphite lattice.

tion, analogous to that of the Ca atom positions in Fig. 5.21. A topographic STM image taken at +300 mV sample bias was used for this purpose since the Ca atoms are topographically small at this bias. The image was drift corrected in exactly the same way as the image used for analysis of the superlattice structure. The stripe direction is not parallel to any of the STM-visible graphite directions so the line profiles are taken in the graphitic (110) direction as illustrated in Fig. 5.22a. Fig. 5.22b displays the correlations of the off-stripe (A) and on-stripe (B) profiles. No systematic distortion of the carbon lattice away from its ideal configuration is measured. The data are noisier than those in Fig. 5.21b, which follows because the interatomic spacing in the graphite (110) direction is greater than in the (100) or (010) directions and also because there are fewer data points per carbon atom than per Ca atom since carbon atoms are closer together and smaller (meaning that there is a lower signal to noise ratio out of plane as well). In short, close examination of the carbon lattice by line profiles, lattice overlays and cross correlation of line profiles (as shown here) reveals no longitudinal or transverse distortions to within the STM in-plane resolution of 0.01 nm. The significant, systematic modulation of the Ca atomic positions is in sharp contrast to the lack of distortion detected in the carbon lattice. However, one certainly cannot rule out modulations smaller than the in-plane instrumental resolution of 0.01 nm. Higher resolution momentum-space techniques, such as X-ray or neutron scattering, could be used to detect smaller average modulations. However, at time of writing no such distortions have been reported.

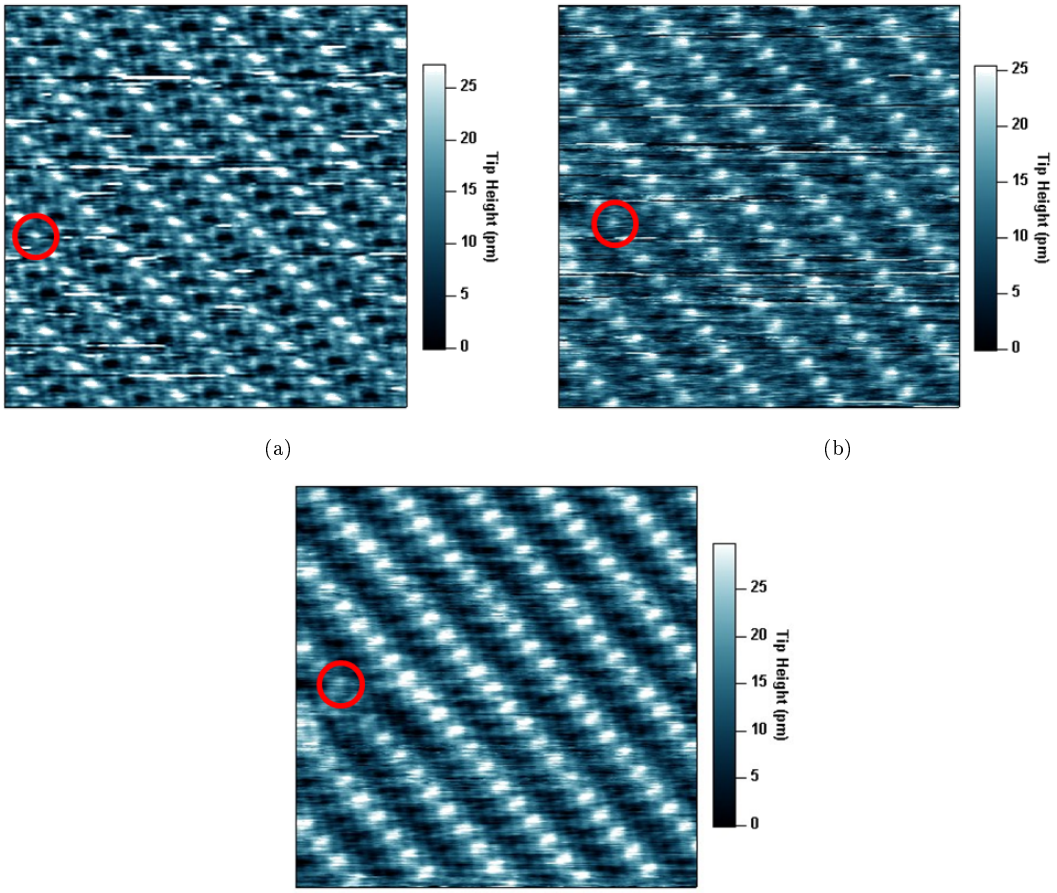

Figure 5.23: Bias dependence of the stripe phase topography. 7 nm × 7 nm constant current STM images of the CaC_6 stripe phase at (**a**) +600 mV, (**b**) +700 mV and (**c**) +800 mV sample bias. All three images were recorded at 50 pA tunnelling current at approximately the same surface location (a spatial reference point has been marked by a red circle in each image).

The broken crystallographic symmetry of the superlattice is also reflected in the electronic behaviour of the Ca atoms, as observed in bias-dependent topographic imaging. Fig. 5.23 shows that the topographic height of the perturbed superlattice position dominates the image above 600 mV, indicating a significantly greater density of unoccupied states at this position. This lends further evidence to the fact that the distortion of the superlattice is strongly linked to the existence of the stripes, although whether it is a cause or an effect of the stripes is not yet clear.

Fig. 5.24 shows the behaviour of the stripes with bias inversion, as seen by topographic STM imaging at ±700 mV. The same two defects are circled in both images; at negative bias (Fig. 5.24a), the positions of both defects coincide with the peak of the stripe modulation and the Ca lattice is centred on the middle of the stripe troughs. At positive bias (Fig. 5.24b), the two defects coincide with the trough of the stripe

modulation and the Ca lattice is centred on the middle of the stripe peaks. The stripe contrast inverts with change in bias polarity (Fig. 5.24c) while the Ca lattice contrast does not (Fig. 5.24d). It would appear, therefore, that the superlattice remains in the same relative configuration in either bias polarity, much as one would expect, but the registry of the stripe shifts by exactly π radians. In otherwords the filled and empty states of the stripe wavefunction are exactly out of phase with one another, producing a quasi-perfect inversion of stripe contrast with bias polarity inversion, and this separation of filled and empty states affects only the stripe and not the superlattice. The remarkable implication is that the stripe contrast involves only the electrons in the graphene planes. Note that the data presented in Fig. 5.24 was recorded during a different set of measurements than the other topographic measurements presented in this section, the tip configuration was slightly different resulting in the qualitative differences seen in topographic surface appearance at +700 mV for Figs. 5.23 and 5.24.

5.6.3 Spectroscopy and spectroscopic imaging

STS, CITS, FT-STM and FT-STS spectroscopic techniques, as detailed in Chapter 4, are used to explore the LDOS and electronic features of the CaC_6 stripe phase. Fig. 5.25a presents a topographic image compiled whilst recording one of six CITS datasets from which all CITS, FT-STM and FT-STS data in this section are derived. The topographic image is recorded at the CITS set point, which in this case is +800 mV sample bias and 50 pA tunnelling current. The spatially averaged conductivity $g(V)$ of the striped CaC_6 surface, the average of all six datasets of 10,000 spectra each, is shown in Fig. 5.25b. The spectra show some similarity to graphite, in that there is a local minima around 0 mV. However, it is important to remember that CaC_6 is doped by 1.2 eV [34] with respect to raw graphite and that therefore the Fermi level is shifted by 1.2 eV and there is in fact no overlap between the spectra presented and the graphitic Dirac cone-like spectra one sees for unintercalated graphite. This does not mean that important information cannot be derived, firstly the most notable feature is a gap of 2Δ 475 mV at the Fermi level, symptomatic of an apparent depletion of states around the Fermi energy. The total zero bias conductance is non-zero, which confirms the bulk transport data (Chapter 3) showing the material to remain metallic in this phase.

CITS $g(\overrightarrow{r}, V)$ and FT-STM $g(\overrightarrow{k}, V)$ images of CaC_6 stripe surface derived from one of the six CITS datasets are presented at energy intervals of 0.1 V in Figs.

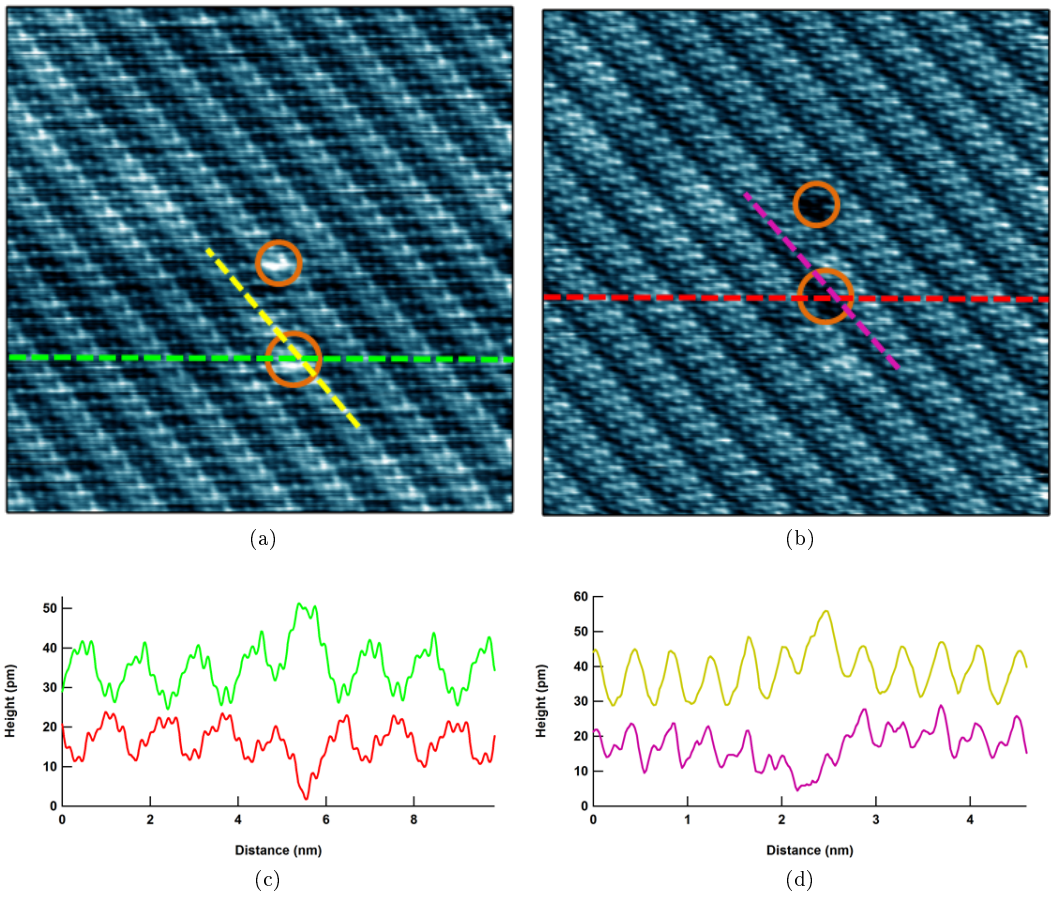

Figure 5.24: Near perfect inversion of stripe contrast with bias polarity. Comparison of defect positions (circled) on 10 nm × 10 nm topographic STM images recorded at (**a**) −700 mV and (**b**) +700 mV sample bias, demonstrate stripe modulation shifts π out of phase with bias polarity change. (**c**) Line profiles marked in (a) (green) and (b) (red) demonstrate contrast inversion of defects and stripe modulation with change of bias polarity. (**d**) Line profiles marked in (a) (yellow) and (b) (purple) showing that Ca lattice contrast does not invert with bias. This can also be seen by comparing the lines marked in images (a) and (b) with the relative position of the stripe modulation. Both images were recorded at 50 pA tunnelling current.

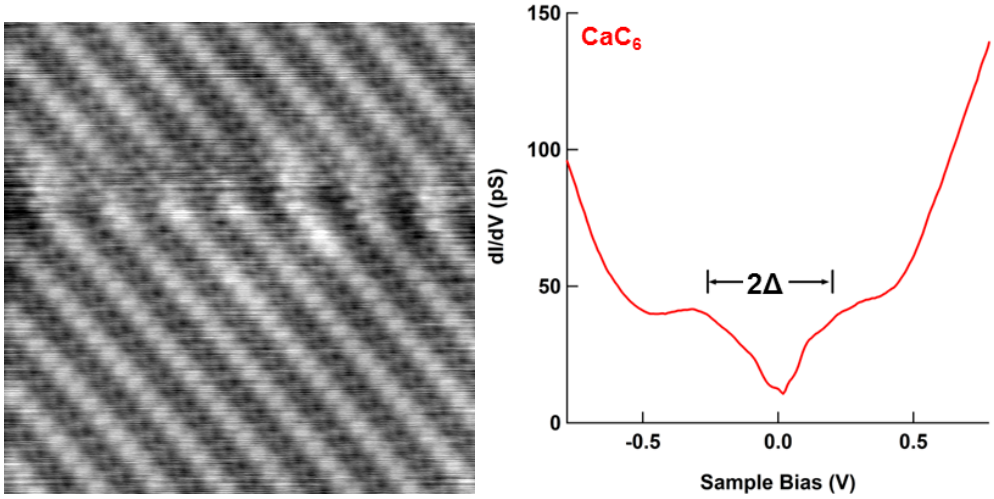

(a) (b)

Figure 5.25: CITS measurements of CaC_6stripe phase: (**a**) Topographic image, recorded at the CITS set point +800 mV, 50 pA, shows the surface area where CITS data was collected. (**b**) CaC_6 stripe phase LDOS presented as a spatial averaged (60,000 spectra), numerically differentiated CITS measurements $g(V) = \frac{\mathrm{d}I(V)}{\mathrm{d}V}$ exhibiting a significant depletion of states around the Fermi level.

5.26 and 5.27. Note that because CITS data is recorded with a much lower spatial resolution the graphite lattice does not appear, the data does not contain the critical four datapoints per unit cell required for the graphite to be seen. Presenting the data in this form has many limitations; firstly only a relatively small number of energies are shown whereas the data was recorded with an energy resolution of 8 mV (at 78 K this is the approximate energy of thermal smearing k_BT), secondly noise in the data is amplified considerably by the numerical differentiation and FFT techniques which makes it difficult for the human eye to accurately find the energy at which certain features appear, disappear or change in intensity. However, in spite of this it is apparent that the relative intensities of the stripe and superlattice peaks change significantly with energy, as does the background. At low energies near 0 mV the background noise is extremely low and the stripe and superlattice reciprocal lattices are easily visible. Most importantly it can be seen that throughout the whole energy range the stripe and superlattice spots always appear in the same reciprocal space location, in otherwords the stripe is a dispersionless feature.

The lack of dispersion is important in helping to identify the nature of the stripes. Electron standing waves are extremely common on metallic surfaces, appearing similar to CDWs at any given energy, but these features are highly dispersive whereas mass density waves are typically static. Fig. 5.28 presents an intensity plot for the stripe (blue in figure) and superlattice (green) reciprocal peaks demonstrating that they do

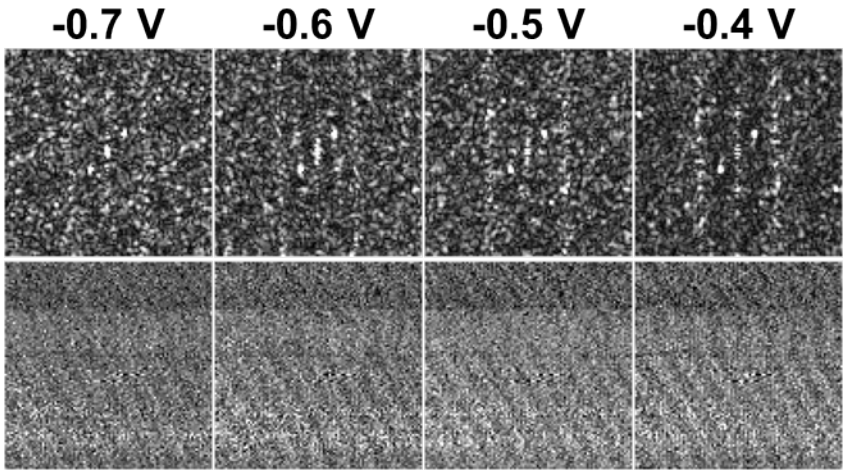

(a)

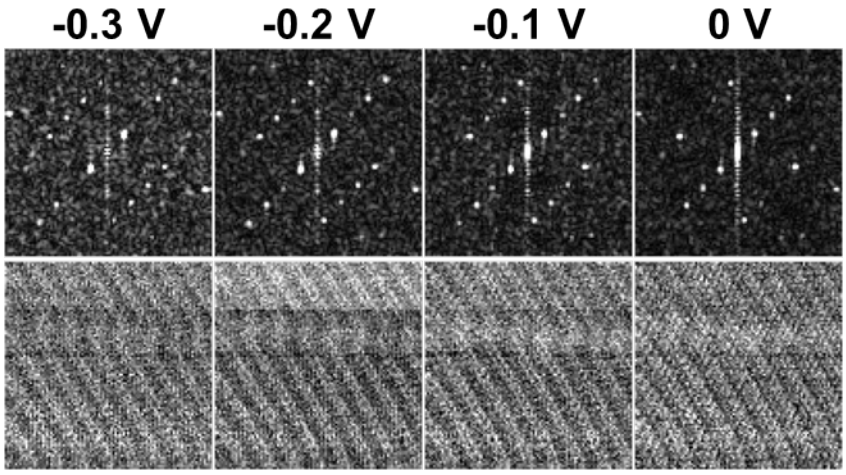

(b)

Figure 5.26: CITS $g(\overrightarrow{r}, V)$ and FT-STM $g(\overrightarrow{k}, V)$ images of CaC_6 stripe surface (part one). Each CITS image is numerically differentiated and plotted at the energy indicated in the figure. Each FT-STM image is a 2D FFT of the CITS image at the corresponding energy. Images are plotted with the FT-STM image on top and the corresponding CITS image below.

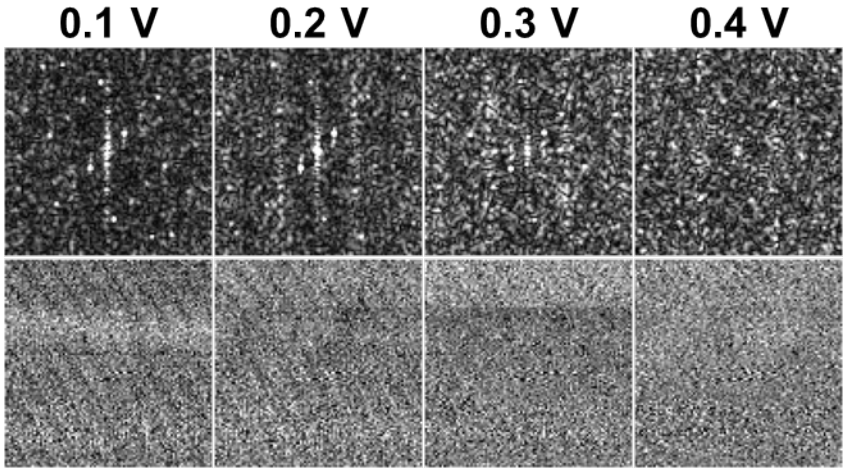

(a)

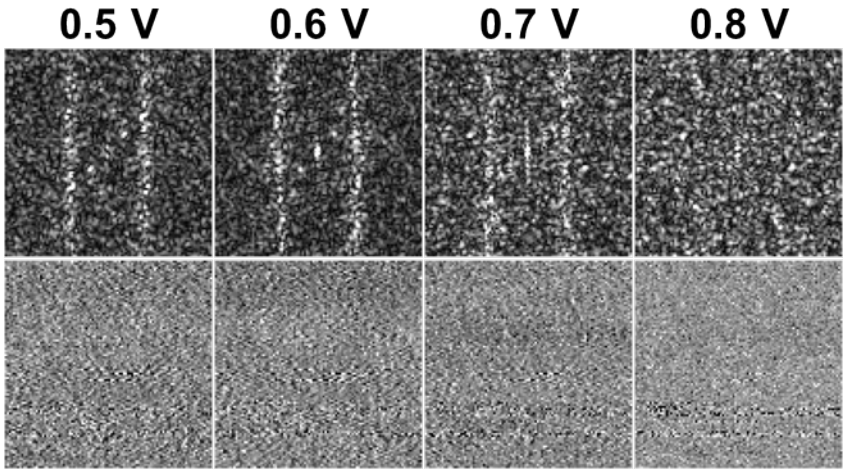

(b)

Figure 5.27: CITS $g(\overrightarrow{r},V)$ and FT-STM $g(\overrightarrow{k},V)$ images of CaC_6 stripe surface (part two). Each CITS image is numerically differentiated and plotted at the energy indicated in the figure. Each FT-STM image is a 2D FFT of the CITS image at the corresponding energy. Images are plotted with the FT-STM image on top and the corresponding CITS image below.

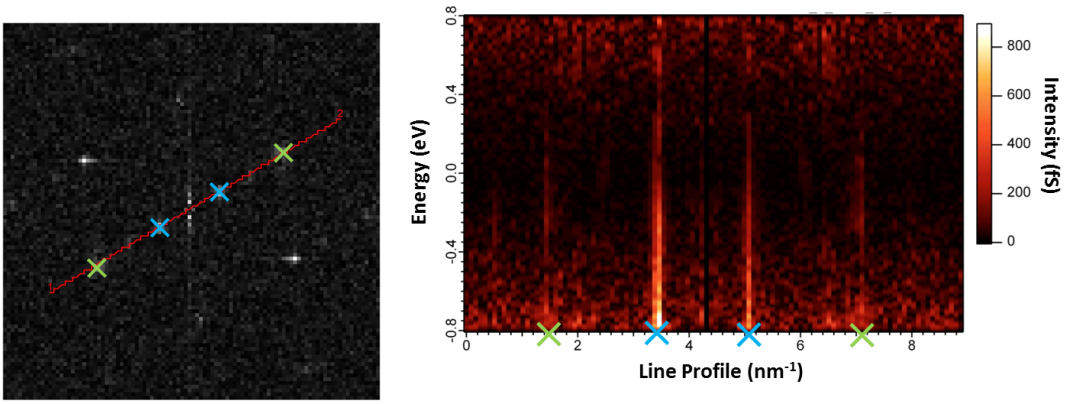

(a) (b)

Figure 5.28: An intensity plot $I(\overrightarrow{k}, E)$ for the stripe and superlattice reciprocal lattice peaks. (**a**) The position of the line profile used for the intensity plot is indicated by the red line in this FFT image, the stripe and superlattice peaks are marked by blue and green crosses respectively. (**b**) The intensity plot shows no dispersion in any of the reciprocal peaks, i.e. neither the stripe peaks (blue crosses) nor superlattice peaks (green) change position with energy $E = eV$.

not disperse at any energy, in otherwords that for all energies q_{CDW} and q_{Ca} are constant.

Another important question is whether the stripes slide, in otherwords whether they change phase gradually as the bias is changed or whether the quasi-perfect inversion of contrast with bias seen in Fig. 5.24 has a discrete transition. Looking at the real-space frames$g(\overrightarrow{r}, V)$ in Figs. 5.26 and 5.27 one can, with sufficient study of the relative positions of the stripes with the edges of the image, determine that the stripes do not slide (this is easiest to see when looking at the position of the stripes at the top of the image, it is clear they are not moving in energy). However, a much better way of determining the phase behaviour of the stripes is to take the conjugate of the FT $I(\overrightarrow{k}, V)$. Ordinarily FFT images are plotted as amplitude retaining all the information about the frequency and intensity but losing phase information. When the conjugate is plotted then one is left with information about frequency and phase but losing intensity information. The undifferentiated CITS$I(\overrightarrow{k}, V)$ is used rather than differentiated CITS $g(\overrightarrow{k}, V)$. This is because in conductivity the phase of the stripes should stay the same; increasing filled states and decreasing empty states (and vice versa) appear the same, so no change of phase could be seen. However, current relates directly to what is seen in topography and as such any change in phase or sliding of the stripes should be observable. Fig. 5.29 presents the phase $\phi(\overrightarrow{k}, V)$ for the stripes ($k = q_{CDW}$, blue in the image), superlattice (q_{Ca}, green) and background

(red). Due to the many stages of numerical analysis required these data are extremely susceptible to noise, consequently the absolute values for phase may be meaningless so are plotted as arbitrary units. However, relative changes in phase still have meaning. The superlattice and background both have similar spectra, namely noise with no discernable transitions in phase, this is unsurprising as one would not expect the background to change phase with energy and topographic imaging has given us no reason to believe the superlattice changes phase with energy either. However, there is a distinct change in phase close to 0 mV seen for the stripes, the exact value is hard to determine because of noise. The phase is approximately constant in negative sample bias, but close to the Fermi level as the sample bias is increased the phase increases dramatically. In a perfect measurement the author believes one should see a transition between two different constant phase values at, or close to, 0 mV. The real data deviates from this because of noise, in particular the signal to noise ratio in positive sample bias is lower (i.e. the stripes are less prominent positive bias, the difference in topographic or spectroscopic intensity on the stripe peak and inside the stripe trough is smallest in high positive bias, e.g. see Fig. 5.27) which is why at high positive bias the spectrum for the stripe phase begins to resemble the background. In short this demonstrates that the stripes do not slide and that the inversion of stripe contrast happens at, or close to, the Fermi level. Logically one would expect the transition to occur at exactly 0 mV, however, whilst the data in no way contradicts such a proposition it also cannot prove it.

The superlattice and stripe reciprocal lattice vectors are marked in the $g(\overrightarrow{k},0)$ FT-STM image presented in Fig. 5.30a. The stripe vector q_{CDW} is marked in blue, whilst two separate vectors are marked for the superlattice reciprocal vector, q_A marked in green and d, q_B marked in yellow. Because of the 30 ^{o} rotation seen for hexagonal lattices when performing a FT q_A corresponds to the superlattice symmetry direction that intersects the stripes in real-space and q_B corresponds to the superlattice lattice direction that runs parallel to the stripes in real-space. FT-STS $g(q,V)$ plots for $\overrightarrow{k} = q_{CDW}$, q_A and q_B are presented in Figs. 5.30b, 5.30c and 5.30d respectively. These plots allow one to link features in the LDOS, namely the overall spatially averaged CITS spectra, to specific features in k-space, features such as the reciprocal lattice spots for the superlattice and stripes. The stripe spot exhibits two main peaks, separated by approximately 475 mV, around the Fermi level, where there is a minimum in the density of states. This analysis strongly associates the gap shown in Fig. 5.25b with the stripe vector q_{CDW}. The broken Ca symmetry seen

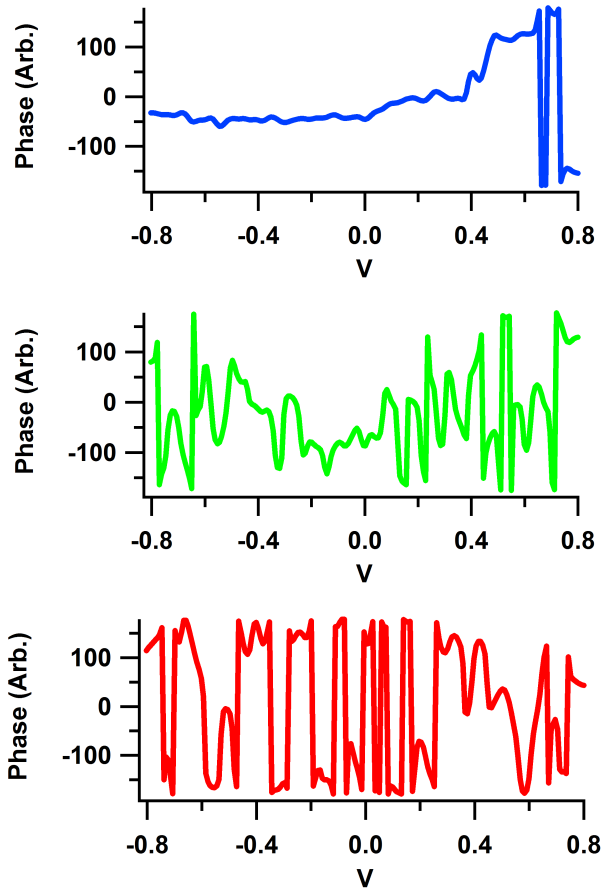

Figure 5.29: Phase $\phi(\overrightarrow{k}, V)$ for the stripes (blue), superlattice (green) and background (red) showing no phase transitions for the superlattice or background (true phase value is constant all that is seen is noise) but a significant phase transition is seen for the stripes very close to the Fermi level.

in Fig. 5.21 is also reflected electronically, each of the two superlattice vectors q_A and q_B exhibit slightly different, but similar, LDOS contributions. The true stripe-independent Ca contribution is seen for superlattice B, this is because this is the Ca symmetry directions which, in real space, runs parallel to the stripes and consequently for which there is no overlap with the contribution from the stripes. The predominant feature in this spectra is a peak at 0 mV, otherwise the spectra is largely flat as one would expect for a metal, and importantly no minima is seen at 0 mV and there is no gap. This reinforces the stipulation made earlier that the stripes would appear to involve the graphene sheets rather than the Ca atoms. Superlattice A, however, corresponds to the Ca atom direction which cuts across the stripes in real space, consequently one would expect to see some involvement from the stripe contribution to the LDOS, furthermore in this direction $q_A = 3q_{CDW}$ and as such the third harmonic of the stripe reciprocal lattice spot coincides with q_A and as such one would further expect a superposition of the stripe FT-STS spectra with that of the superlattice. As expected Fig. 5.30c appears very much as a convolution of Figs. 5.30b and 5.30d wherein the 475 mV gap is slightly visible, as is the peak at approximately 0 mV. Further to this it can also be seen that Superlattice A has a much greater contribution to the LDOS in negative bias than Superlattice B. This is consistent with Fig. 5.24 wherein the topographic contrast between atoms on and off of the stripe is much greater in negative bias imaging. Note that the faint lines in the FT-STS plots represent the six individual CITS datasets recorded, and the bold lines represent the average of the six datasets - this helps with distinguishing noise from real features, in particular because noise is greatly amplified by the calculations required to derive FT-STS and using only a single dataset it can be difficult to distinguish real features from false ones. The red line plotted on each graph is the background Fourier intensity, which has already been subtracted from all of the presented data.

As discussed in Chapter 2 no substantiated measurements of CDWs in graphitic systems have been made. However, CDWs are suggested as a possible origin for various unexplained features seen in GICs and graphite [30, 31, 32, 39] However, the important difference is the availability of electronic structure measurements which can be used to differentiate the stripes other effects with similar appearances including Moiré patterns [40], electron standing waves [41], and surface reconstruction or lattice depletion. [4, 32] It is therefore important to consider these phenomena when examining the data. In Section 5.6.2, it is demonstrated that the stripes coexist with the predicted carbon and Ca lattices. This precludes the possibility that the stripe

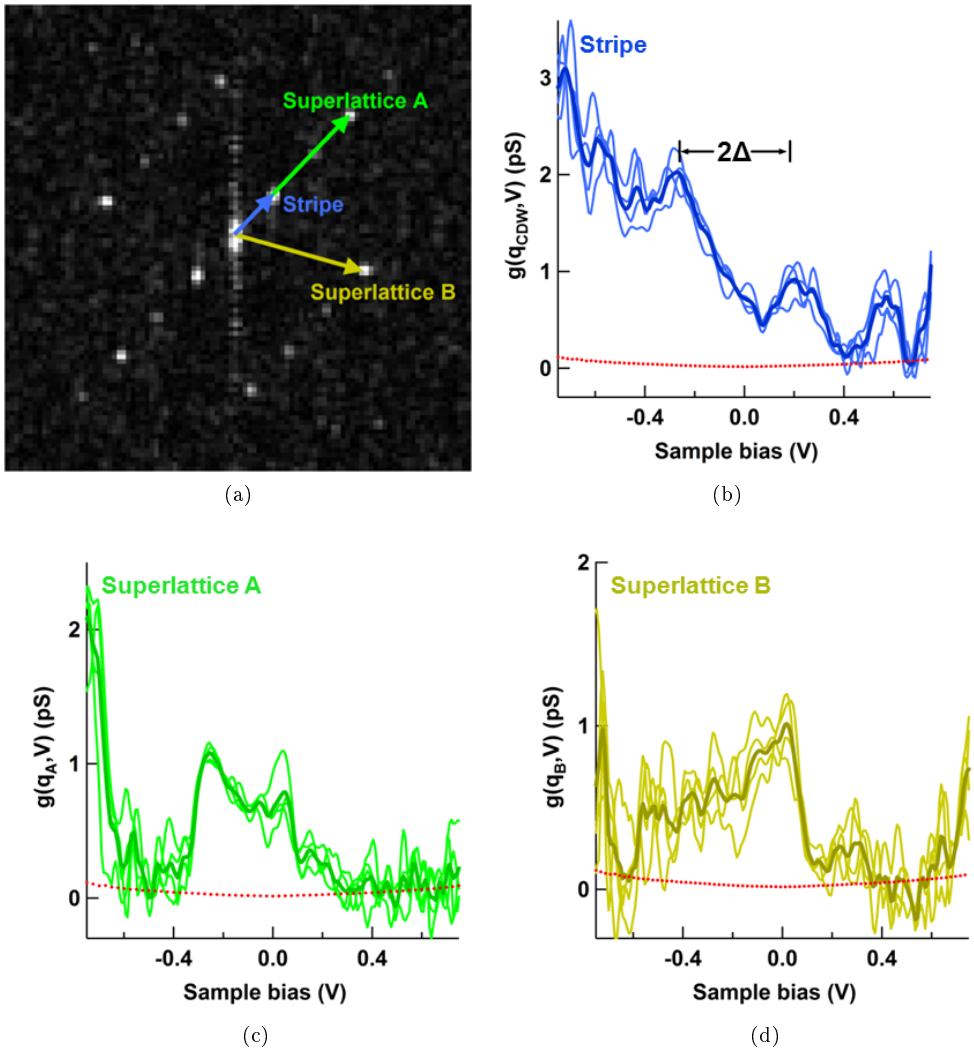

Figure 5.30: FT-STS of the CaC_6 stripe phase: (**a**) $g(\overrightarrow{k},0)$ FT-STM image of CaC_6 stripe phase at 0 mV. (b–d) FT-STS $g(q,V)$: Fourier intensity plotted as a function of energy for the stripe (b, q_{CDW} marked in blue) and Superlattices A and B (c, q_A marked in green and d, q_B marked in yellow) spots as indicated in (a) respectively. Faint lines represent individual datasets, bold lines represent the average of all datasets. Red dotted line is the background intensity (already subtracted from all lines presented).

phase is a surface reconstruction, that is, it results from a depletion or reorganization of the intercalant or carbon lattice. Second, a Moiré pattern could not lead to a gap in the LDOS such as that which has been observed in Fig. 5.25b. Finally, it is shown that the stripe period does not change with bias (Figs. 5.26, 5.27, 5.28 and 5.29), thus ruling out electron standing waves and Friedel oscillations that are dispersing effects. However, our observations are consistent with a CDW. In fact, the direct association of a gap (Fig. 5.30) with the stripe periodicity provides strong evidence that this is a CDW gap associated with the depletion of states around the Fermi level. [65] The near-perfect inversion of contrast with bias polarity seen in Figs. 5.24 and 5.29 is also characteristic of a true CDW [67, 79] as is the fact that stripes do not slide. The large gap size indicates a significant modification of the FS, but is consistent with that seen in other lamellar materials. For example, for $NbSe_2$, $2\Delta = 68\,\text{meV}$ with a transition temperature $T_{CDW} = 33.2\,\text{K}$ [54], which gives a ratio $2\Delta/k_B T_{CDW} = 23.9$ similar to that which has been measured for CaC_6 $2\Delta/k_B T_{CDW} = 22.1$ (with $T_{CDW} = 250\,\text{K}$ as indicated in Chapter 3). The stripes themselves share a very similar appearance to numerous other striped CDW phases imaged by STM techniques [79, 73, 123] and satisfy all of the criteria discussed in Chapter 2. One may contend that SDWs and CDWs have somewhat similar characteristics, however, all data presented for the stripe phase was recorded using chemically etched tungsten STM tips which have no spin polarisation and as such are not sensitive to magnetic effects or SDWs. The proposed mechanism and implications of the CDW phase are discussed at length in Chapter 6, as are the important differences between this surface phase and the others reported.

5.7 Two-striped surface

The final surface type discovered on CaC_6 was the *two-striped surface* phase. This surface type was encountered only once and persisted for less than three hours. For this reason the depth of the data available is limited, and whilst this surface is extremely interesting it is difficult to draw conclusions regarding its nature from the current pool of data. The surface has an appearance akin to the chiral CDW surface reported for $TiSe_2$ [78] in that a number of stripes are seen. One stripe at the surface, and then others that are subsurface and rotated to a different symmetry configuration. A first glimpse of the two-striped surface is presented in Fig. 5.31. Much like the single stripe surface the striped surface area was discovered immediately upon tip approach.

However, whilst the single stripe surface was found to extend for many 100 nm in each direction, the two-stripe surface only extended over an area of approximately 20 nm by 40 nm, scanning outside of this area caused a loss of AR imaging and greatly increased the noise seen in topography. This indicates that the small island of clean surface upon which the two-stripe surface is observed was surrounded with significant amounts of loose material or damaged surface (e.g. loose graphitic flakes or weakly bound surface intercalant material). Fig. 5.31a presents a topographic STM image of the two-stripe phase in which one can see at least two hexagonal atomic lattices, a strongly-visible uni-directional stripe running almost vertical throughout the image, and a second dimly-visible uni-directional stripe running just off horizontal across the image. In addition to these features the topographic height variation can be seen to be very low compared with the expected phase of CaC_6, but perhaps not as low as that which is seen for the stripe phase. FFT of the topographic STM image (Fig. 5.31b) reveals a complex superposition of numerous lattices and stripes.

The simplest lattice to identify is the graphitic lattice (q_C), which is circled in red in the figure, this lattice measures the expected 0.25 ± 0.01 nm. The superlattice appears to split into two reciprocal lattice peaks, which are marked with green circles, but the splitting is not the same in all three superlattice symmetry directions. If there were two superlattices one would expect to see two hexagonal sets of reciprocal lattice peaks centred on the origin of the image, however what is actually seen is two hexagonal patterns which are translated with respect to each other in one of the reciprocal lattice directions (in the direction of the green circles). The reason for this is due to a structural abnormality in the superlattice which will be analysed in greater detail later in this section.

The blue circle denotes the reciprocal lattice peak for the primary stripe (q_{stripe}). The splitting of the superlattice means that it is difficult to determine whether the stripes are commensurate. However, comparing the stripes to the graphitic superlattice peaks reveals that the stripes are not commensurate (i.e. q_{stripe} is not a rational multiple of q_C) with the CaC_6 unit cell. Furthermore, the stripe peak does not lie at 30^o rotation from q_C as with the one stripe phase, but rather it is out of alignment by 4^o. The stripe period lies between 1.60 nm and 1.69 nm, the upper and lower bounds are due to pixelation of the data and each quoted value has a precision error of 0.01 nm associated with the STM limit of resolution. The remaining peaks which form a six-fold symmetry around the origin with q_{stripe} relate to the other (sub-surface) stripes and lie within the same upper and lower values quoted the primary peak.

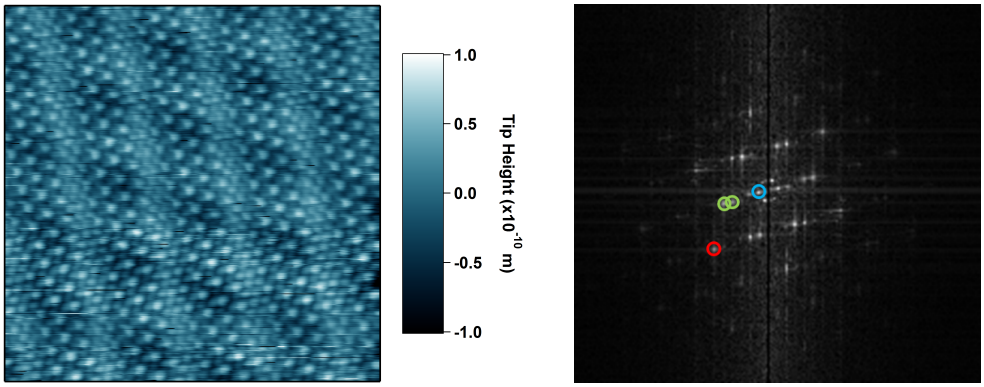

(a) (b)

Figure 5.31: The two-stripe CaC_6 phase as seen in (**a**) a 7 nm by 7 nm topographic STM imaging recorded at -400 mV sample bias and 100 pA tunnelling current, and (**b**) a FFT image of (a) with the graphite reciprocal lattice marked with a red circle, the surface stripe reciprocal lattice vector marked with a blue peak and two superlattice peaks marked in green. The surface has a similar appearance to the one-stripe phase, however the stripe symmetry is slightly different, including a small misalignment between the stripe and superlattice, and there appear to be hints of subsurface stripes which are also rotated 60^o. Note also a six-fold feature in the FFT at very low momentum which represents the hexagonal lattice formed at by the intersections of the surface and subsurface stripes.

Fig. 5.32 presents line profiles taken from a topographic STM image (the same image presented in Fig. 5.31) of the two-stripe surface in two superlattice symmetry directions; one cutting across the primary stripe (red) and one approximately parallel to the primary stripe (green). The green line profile reveals that the superlattice has a regular, undistorted signal. Furthermore, a subtle sine-wave distortion can also be seen in this profile, this is due to the presence of a second sub-surface stripe which can be dimly seen in the topographic image itself. The red profile reveals a very interesting property of the surface; the superlattice appears to be interrupted and distorted at the position of the surface stripe. The profile itself (interpreted left to right) can be seen to intersect three calcium atoms, then part of the surface stripe for which there are no calcium atoms, then the profile misses three calcium atoms as the atomic registration appears to have changed, before yet again intersecting part of the stripe for which there are no calcium atoms, and finally intersecting three more calcium atoms as the superlattice registry appears to have returned to its original position. This can be seen either by studying the position of the red line on the topographic image, or by observing the fact that the strong superlattice atom shape can only be seen for two parts of the line profile graph (between approximately 1 nm and 2.5 nm, and between approximately 4.5 nm and 6 nm).

The alternating registry of the superlattice on either side of each surface stripe

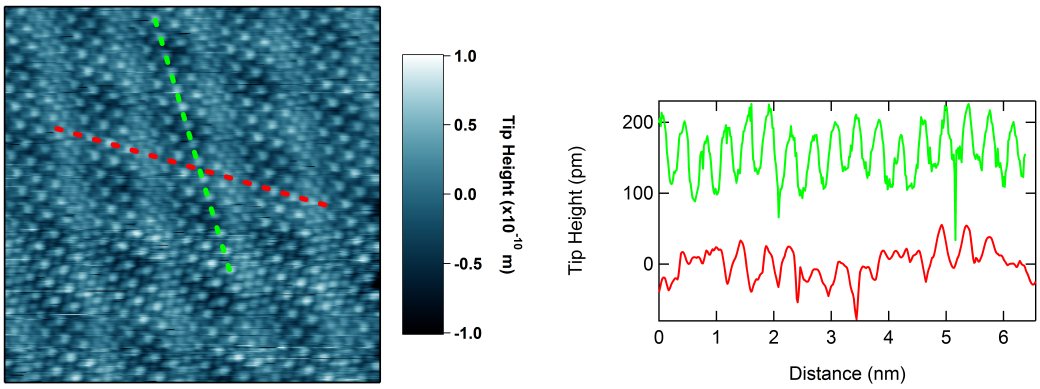

Figure 5.32: Topographic line profiles in superlattice symmetry directions (right) parallel to the stripe (green) and across the stripe (red) as marked in the topographic STM image (left). Note the subtle periodic influence of the subsurface stripes in the green profile and the misalignment of the Ca lattice between the surface stripes evident in the red profile.

is best illustrated in Fig. 5.33: a ball-and-stick schematic of a single graphene layer with $\sqrt{3}a \times \sqrt{3}a$ R30° superlattice, in otherwords the surface layer of the CaC_6 expected phase, superposed upon a noise-filtered topographic STM image. The two red lines denote the position of the peak of the surface stripe. Outside the red lines the schematic overlay can be seen to match the topographic structure of the surface with the blue superlattice atoms resting on the recorded superlattice positions. There are small discrepancies due to drift in the data, but it is clear that the structure matches. Between the red lines the registry of the recorded superlattice has changed such that the schematic and surface do not match. In simple terms it would appear that outside the red lines the superlattice has α registry and between the lines it has β registry where the superlattice has the same symmetry but is translated by one graphene hexagon. This shift in registry happens at every stripe, with the superlattice alternating between the two different structures. Furthermore, the superlattice is not influenced in the same way by the sub-surface stripe. This implies that either the surface stripe is different to the ones below, or that the superlattice is only affected by the stripe which is found at the same surface depth. It is important to note that superlattice layers below the surface cannot be seen and therefore from STM measurement alone one cannot know if the unusual behaviour which is evident at the surface persists within the bulk, nor whether the sub-surface stripes have any particular effect on the superlattice structures below. However, it is worth noting that there is no reported evidence in bulk measurements (XRD, neutron scattering etc.) of such abnormalities in the superlattice. The yellow line denotes the superlattice symmetry direction which most closely matches the direction of the primary stripe and the red line follows the angle of the stripes themselves, the difference is approximately 4° as

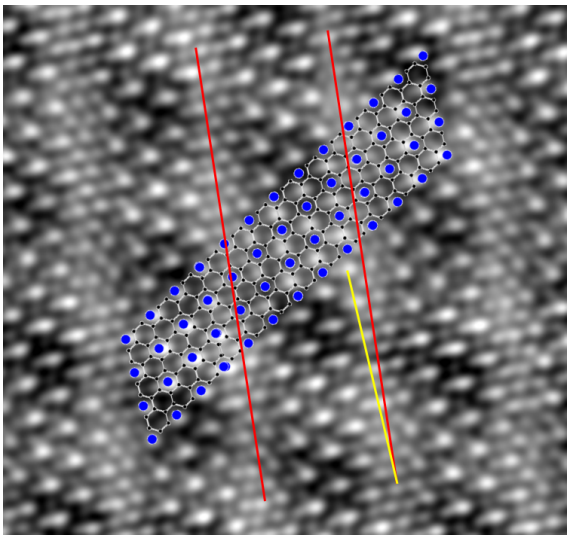

Figure 5.33: Analysing the superlattice of the two-stripe phase: A noise-filtered topographic STM image of the two-stripe CaC_6 phase with superposed schematic of a single graphene layer with Ca superlattice. Note that between the red lines, which also highlight the angle of the surface stripes, the Ca atom positions do not match the schematic, but outside the two red lines the Ca atom positions are coincident with the expected structure. The yellow line marks the superlattice symmetry direction closest to the angle of the stripes, the difference between the red and yellow lines is approximately 4 ^{o}.

expected from the FFT image in Fig. 5.31b. The sub-surface stripe is weakly defined and as such it is difficult to determine, from topography, if the stripe shares a superlattice direction or whether it is also angled slightly differently to the lattice. The FFT also does not answer this question definitively since an error of even one pixel in the FT image taken at the position of q_C gives an error in the angle equal to the size of the expected misalignment, this means the question of whether stripes below the surface share the surface stripe misalignment cannot be answered with the data available.

Fourier filtering (Fig. 5.34) helps to illuminate both the stripe and superlattice structures. The red-bordered image displays the results of a selective filtering as indicated by the red circles in the FT image. This image displays a perfect graphene layer; a hexagonal lattice of atoms with $a = 0.25\,\mathrm{nm}$ as expected. There are no defects and none of the lattice is obscured or warped. The complete graphene layer is also observed in Fig. 5.35, another topographic STM image of the two-stripe phase recorded with a different tip condition and at +300 mV sample bias. In this alternative appearance the superlattice cannot be seen, except as a perturbation of the carbon atoms, and the presence of a full defect-free graphene layer is evident. The fact that an change in tip configuration and tunnelling conditions can hide the superlattice, together with the fact that unlike the superlattice the graphitic lattice is always

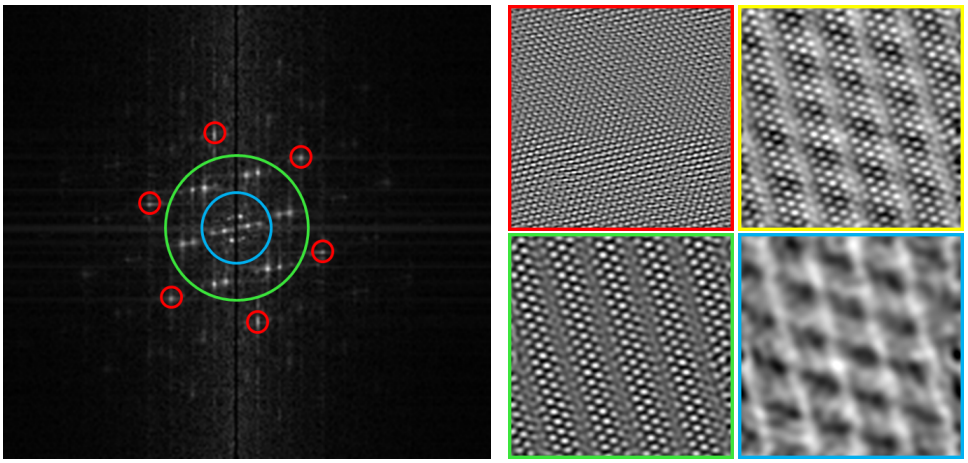

(a) (b)

Figure 5.34: Fourier filtering reveals stripe structure and superlattice abnormalities. (**a**) An FFT image of the two-stripe phase. (**b**) Filtered topographic images of the two-stripe surface. The red-bordered image shows the graphitic lattice, a 0.25 nm hexagonal lattice, selectively filtered from the red-circled spots in (a) only. The remaining parts of the topography (i.e. everything except the graphite lattice) are shown in the yellow-bordered image. The green-bordered image shows a band-pass image including only frequencies between the blue and green lines in (a); in this image the superlattice can be seen. The blue-bordered image shows a low-pass filtering which includes only the low-frequency features within the blue circle in (a); in this image only the stripes are seen. The surface stripe is still present, a sub-surface stripe running from the top left to the bottom right of the image is readily visible, also faintly visible is a third stripe running from the top right to the bottom left of the image.

visible and free of defects or obscuration, indicates that the surface of the two-stripe phase is graphene terminated. The remaining topography in Fig. 5.34 after filtering out the graphitic lattice is shown in the yellow-bordered image. This image clearly shows the presence of the sub-surface stripe. Furthermore, the registration switching of the superlattice is much easier to see without the graphitic lattice complicating the image; the lattice can be seen to switch registry on either side of each of the surface stripes and at the stripe itself rather than the superlattice being absent it appears to be obscured or warped.

The green-bordered image displays the topography after band-pass filtering of frequencies between the blue and green circles marked on the FT image. In this image only the superlattice can be seen. Even with the stripe contribution removed one can see that the superlattice is interrupted by the stripe. Somewhat unusually instead of an absence of calcium atoms at the stripe position the imaged atoms appear to be partially obscured or absent. This is very unusual and consequently makes it difficult to determine whether there is an abundance of calcium atoms, or a deficit. If there were too many atoms perhaps this would explain the unusual switching of registry coupled with overcrowding of the superlattice at the position of the stripes

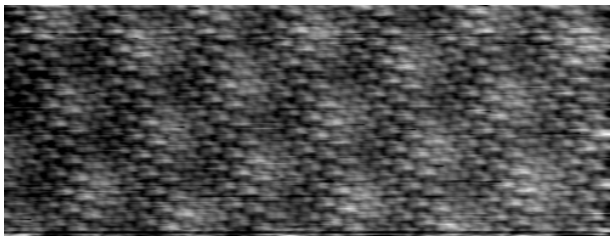

Figure 5.35: A cropped and noise-filtered topographic STM image of the two-stripe phase recorded at +300 mV and +50 pA. Note that a tip configuration change means that in this particular image the superlattice is not imaged directly, a full graphene sheet is seen and the superlattice contribution manifests as a manipulation in the appearance of the carbon atoms between the surface stripes.

which results in the atoms not being imaged correctly. Alternatively it could be that the lattice is depleted, in this case the alternating registry is a new relaxation of the lattice and the partial/obscured atoms which are imaged could be weak tunnelling from layers below the surface. In either case the presence of the stripe appears to have negatively impacted the ability of the tip to image exactly what is happening to the superlattice at the position of maximum stripe intensity. Having studied the superlattice more closely the reason for the splitting of the superlattice peak in the FT image becomes clear: The two different registries of the superlattice which are present within the image are translated by one graphene hexagon with respect to one another, this effectively means that there are two superlattices each acting as satelites of their average position. This means that the peaks which are seen in the FT image are in fact each satelite peaks around an invisible (zero intensity) average peak which should sit at the ideal superlattice position. If the average is taken for each pair of superlattice peaks in the FT image then they form a hexagonal lattice measuring 0.43 nm as seen for the expected phase. This interpretation also explains why the superlattice splitting occurs in only one direction which is also the direction of the stripe period.

Finally the blue-bordered image (in Fig. 5.36) presents the results of a low-pass filtering for which only frequencies within the blue circle marked in the FT image. In this image only the stripes are visible, together with some low frequency noise. Two stripes are immediately visible; the primary surface stripe which is very strongly defined in the image, and a second more diffuse, lower intensity stripe rotated approximately 60^o with respect to the primary stripe. Careful observation also reveals a low intensity third stripe orientated at approximately 60^o with respect to both of the other stripes. The three stripes intersect at the same point forming a hexagonal lattice of increased intensity where the stripes overlap, in certain tip configurations

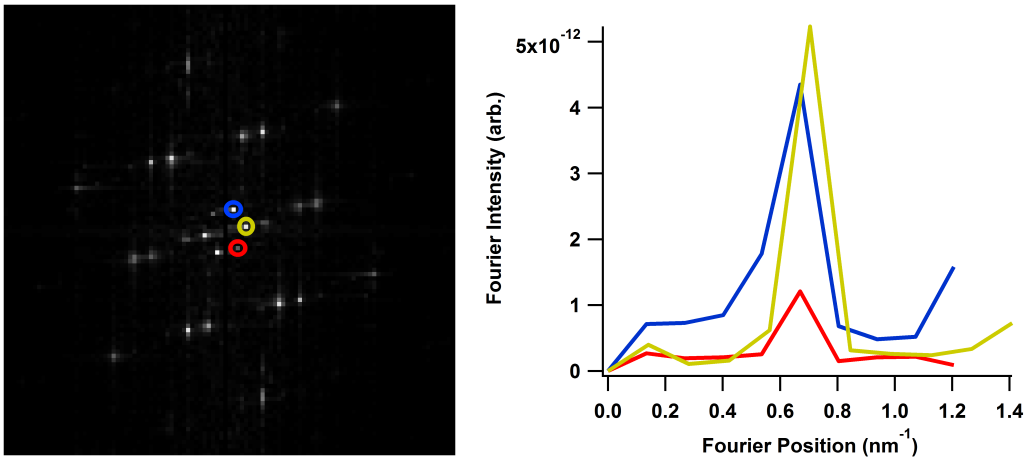

(a) (b)

Figure 5.36: Fourier analysis of the sub-surface stripe structure. (**a**) An FFT image of the two stripe phase with the reciprocal lattice peaks for the surface and sub-surface stripes circled in blue, yellow and red. (**b**) The relative Fourier intensities of the three peaks marked in (a).

the hexagonal lattice formed by the overlap of the stripes is easier to see than the stripes themselves, for example as seen in Fig. 5.37a. An FT image of the largest topographic STM image recorded (Fig. 5.37a) is presented in Fig. 5.36, because of the increased number of stripe unit cells the stripe peaks (circled in blue, yellow and red) are sharper and satelite peaks for the stripes are visible around the superlattice ($q_{Ca} \pm q_{Stripe}$) and graphite lattice ($q_C \pm q_{Stripe}$) peaks. The relative Fourier intensities for each of the stripe peaks, indicated by matching colour, are plotted in Fig. 5.36b. The largest peak (yellow) corresponds to the primary surface stripe. Peak intensity can be seen to drop rapidly with increasing surface depth for the remaining peaks, as one would expect for increasing sub-surface depth. The decreasing yellow-blue-red Fourier intensity indicates that the stripes rotate anti-clockwise with increasing sample depth. Since only one surface is measured there is no way to know whether this is always the case or whether other scenarios are possible, such as random ordering or clockwise ordering. Note that both clockwise and anti-clockwise ordering are observed for $TiSe_2$ [78], the most qualitatively similar system reported.

If random ordering were possible then it could be possible for two consecutive layers to have stripes in the same direction. Since all three stripes share an intersection this indicates that the stripes may be pinned by some feature(s) of the sample, otherwise one would not expect all three stripes to pass through the same points despite their differing orientations. If this is indeed the case then one may expect that for two consecutive layers with stripes orientated in the same direction the second sub-surface stripe would not be visible since it would be entirely coincident with the

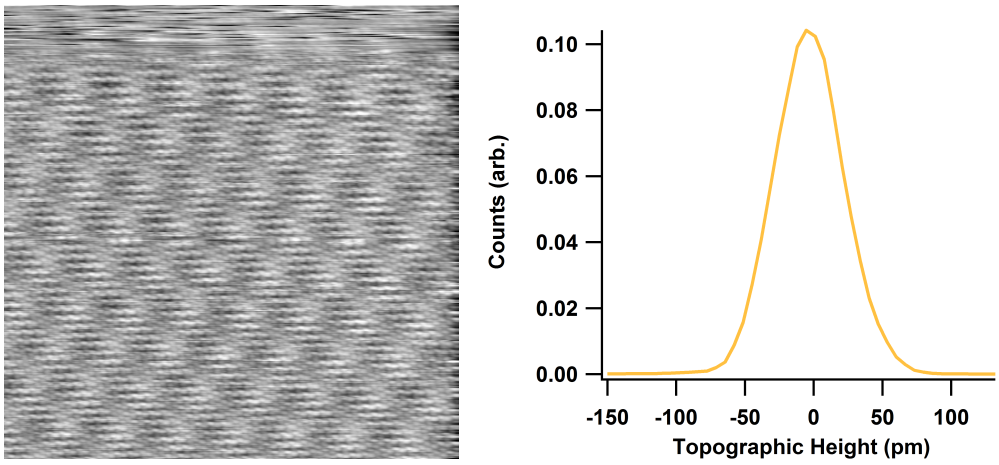

(a) (b)

Figure 5.37: Large scan topographic measurements of the two-stripe surface. (**a**) A 15 nm by 15 nm topographic STM image recorded at +300 mV sample bias and 50 pA tunnelling current. A tip condition change can be seen at the top of the image. (**b**) A histogram of heights for (a) discounting the upper segment of the image containing the tip condition change. FWHM surface roughness is approximately 80 pm.

surface stripe. Unfortunately there is no data available to demonstrate this is possible, but were it to be possible it would go some way to uniting the one and two-stripe surface types. Indeed these two surface stripes share a number of similarities which set them apart from the other surface types: the two-stripe phase is also remarkably flat, as shown in Fig. 5.37, for which the FWHM topographic height variation is approximately 80 pm. Furthermore, both striped surfaces show changes in topographic appearance with changing tip condition and/or scan bias in a way that is not seen for the expected phase surface type. This indicates that the two-stripe surface may also have a complicated LDOS, much as the one stripe phase does, but unfortunately all attempts to make spectroscopic measurements met with dramatic changes in tip condition and ultimately a loss of AR imaging.

Much like the one stripe surface, the two-stripe phase also had a finite life span (of just under 3 hours) after which imaging was lost temporarily. When AR imaging was re-established approximately 5 minutes later only the structure for the expected phase, with no detectable abnormalities in the superlattice structure, was observed. All measurements on the two-stripe phase were made with a mechanically cut Pt-Ir STM tip, as opposed to all other data presented in this chapter which were recorded using chemically etched W STM tips (as discussed in Section 4.3.2). In conclusion this two stripe phase has a interesting structure and draws attention to the fact that not only can the CaC_6 play host to a stripe phase but so can sub-surface layers of the material. This is important in interpretation of the two different striped phases as it alludes

to possible existence of such features within the bulk of the sample. Furthermore, if this second striped surface also has a CDW nature then the possibility for a change in lattice registry and incommensurability of the CDW phase is indicated. The limits of the data make hard conclusions difficult but nevertheless the measurements do highlight some tantalising possibilities regarding the ground states of CaC_6 above the superconducting transition. It would appear that a flat, graphene-terminated surface plays an important part in stabilising the stripes.

5.8 A brief summary of surface types

This section presents a brief summary of the various phases discovered on the CaC_6 surface. The basic characteristics are listed as are any noteworthy features, for detailed quantitative information about each surface refer to the appropriate section in Chapter 5. For further discussion of the surface conditions or physics behind each surface see Chapter 6.

Non-atomically resolved surfaces: These surfaces are those for which AR imaging was not achieved. In general little additional information is available. These surfaces are characterised by high noise, surface mobility and frequent tip condition changes. Of all surfaces measured this surface category was encountered most frequently. However, unlike the other surface types the loose definition means that not all surfaces categorised as non-atomically resolved necessarily share the same nature.

Graphite-like surfaces: These surfaces are those for which AR imaging is successfully achieved. However, only the expected 0.25 nm carbon lattice is observed and no superlattice can be found. These surfaces were rare, constituting a total of only two measured surfaces. Spectroscopically these surfaces appear to resemble unintercalated graphite and imaging is usually of moderate to good quality in terms of noise and surface flatness.

Expected phase surface type: This surface type resembles exactly what one would expect to see for a single layer of graphene and one Ca lattice layer. Namely a hexagonal 0.25 nm lattice with a 0.43 nm hexagonal superlattice of slightly larger atoms. Spectroscopically these surfaces vary significantly and exhibit moderate to high levels of noise in both imaging and spectroscopy. The most notable feature other than the atomic lattices is that the surfaces are universally metallic with a significant conductivity at 0 mV sample bias. Of all AR-imaged surfaces this type was by far the most frequently imaged.

The triple-superlattice surface: Encountered only once. This surface resembles the expected phase. However, two additional superlattice peaks are visible in FT-STM. These are tentatively ascribed to a crystal structure defect from the puddling seen during the intercalation process. Spectroscopically this surface appears to unit the disperate spectra seen for the expected phase leading the author to conclude that the spectra seen for this phase is perhaps the best LDOS measurement of the CaC_6 normal phase. Additionally this surface type was imaged with very low noise or mobility despite proximity to a step edge, indicating a high level of stability compared with some of the other surface types.

The stripe phase surface: The underlying atomic structure exactly matches that of the expected phase. However, an additional 1D sinusoidal surface modulation is seen superposed and commensurate with the expected structure. This feature is shown to be dispersionless with a period of three Ca atoms and shares real-space symmetry with one of the graphitic lattice directions. The small modulation amplitude, perfect inversion of contrast with imaging bias polarity and associated 15% superlattice distortion provide strong evidence that the stripe is a CDW. Spectroscopic measurements and imaging support this conclusion as a significant depletion of states is seen near the Fermi level and by FT-STS is found to associate with the stripe period. Additionally the stripe surface is much more stable and flat than the expected phase. Typically less than half the topographic height variation and significantly less surface mobility or ad-atoms are seen when compared with the expected phase. Furthermore, the stripe phase was the only surface type to be successfully measured over large (above 200 nm) areas of the surface. It is not clear whether these superior surface conditions are caused by or are the cause of the stripes. The stripes had a limited lifespan after which the expected phase was recovered.

The two-stripe surface: Similar to the stripe phase, however, the stripes in this case are shown to be incommensurate. Furthermore, additional sub-surface stripes are measured and shown to rotate anti-clockwise in successive sub-surface layers. Each stripe ties closely to a symmetry direction of the underlying atomic lattices, but is incommensurate by approximately 4^o unlike the single stripe phase. Significantly less data is available for this surface, including less topography and no spectroscopic measurements. Consequently, conclusions are extremely speculative at this stage. Note also that the stripes spread over a relatively small area of 40 nm or so and the topographic images recorded were noisy and significant movement of material on the surface is suspected. The two stripe phase had a particularly short life span of only

a few hours after which the expected phase was recovered.

Chapter 6

Discussion and Conclusion

This chapter includes a summary of the key findings reported in this thesis and discussion of the potential mechanisms behind some of the interesting phenomena observed. The impact of the newly discovered striped CDW phase is explored. The novelty of the research is discussed and new ideas for research and ways of carrying forward the results reported are presented. Possible reflection on the bulk properties of CaC_6 is also included.

6.1 Key findings

This section presents a summary of the results reported within the thesis. A number of the discussions in Chapter 5 are expanded, with further insight and speculation regarding the mechanisms behind the phenomena which have been measured.

6.1.1 Atomic resolution imaging of the CaC_6 surface

Reported in this thesis is the first successful real-space AR imaging of the CaC_6 surface structure. The expected structure is revealed (Section 5.4) as are a variety of non-AR surfaces (Section 5.2) and surfaces reminiscent of non-intercalated graphite (Section 5.3). [14] Achieving AR on cleaved materials is non-trivial [109], including previous studies on this material. [3] Importantly a number of previously undiscovered phases of the CaC_6 surface are revealed; a triple-superlattice surface (Section 5.5), the stripe phase (Section 5.6) and the two-stripe phase (Section 5.7). Each of the surface types possess the underlying structure of the expected phase but are superposed with additional superlattices or stripe orders. This wide range of surface types highlights the importance of knowing what is being measured. In the case of the work reported by Bergeal *et al.* no AR was achieved. [3] This raises questions regarding which of the surface types their measurements apply to and whether the presence of the stripe phase would influence the superconducting properties.

In the case of the triple-superlattice surface, the spectroscopic similarity to the expected phase (Figs. 5.11 and 5.14) implies that the surface is a perturbation or anomalous presentation of the normal CaC_6 structure, rather than an exotic electronic phase. In this case the suggested intercalation anomaly detailed in Section 5.5 appears to fit best.

It is natural to ask why so many different surface types are seen. This is likely due, at least in part, to the cleaving process used for preparation of the sample surface (see Chapter 3). Logically surfaces may be graphene-terminated, Ca-terminated, or terminated by partial lattices of Ca atoms. The polycrystallinity of the samples (Chapter 3) suggest that if sufficient measurements are made all of these scenarios will be encountered. Evidence presented in Chapter 5, including measurements of surface roughness (Figs. 5.10, 5.20 and 5.37) and the fact that for the stripe surface the appearance of the superlattice could be tuned out by altering the scan bias (Figs. 5.19a and 5.19b), indicate that the stripe and two-stripe surfaces are terminated by graphene layers. Other surface types, which exhibit much greater noise in imaging and

spectroscopy, appear to be terminated in Ca lattices. This leads to greater surface roughness, tip contamination rates and surface mobility. This ultimately leads to inferior imaging and spectroscopy as observed in Sections 5.2, 5.3 and 5.4. The further implication is that striped surfaces have optimal doping, whereas other surfaces have an uncontrolled amount of additional dopant atoms at the surface.

6.1.2 Discovery of a striped CDW phase

The stripe phase is shown to be a commensurate CDW phase with a period three times that of the Ca lattice. A superlattice distortion of 0.06 ± 0.02 nm is observed (Fig. 5.21) which shares the CDW wavevector $q_{CDW} = \frac{1}{3}q_{Ca}$. The LDOS for the expected and triple-superlattice surfaces (Fig. 5.14) are believed to be the same, the reasons for this are discussed in detail in Section 5.5. This expected phase LDOS does indeed resemble the calculated DOS reported by Calandra *et al.* [35] However, there are very significant electronic differences between the LDOS of the expected CaC_6 surface and of the stripe CDW phase (Figs. 5.11 and 5.25). In particular the $2\Delta \approx 475meV$ CDW gap arising from the depletion of states around the Fermi level seen for the stripe phase, which is not predicted by DFT calculations. Phase inversion of filled and empty states, which is characteristic of a 1D CDW (Section 2.2.2), is observed in both imaging (Fig. 5.24) and spectroscopic measurements (Fig. 5.29). Finally, the use of FT-STS in the analysis of a CDW is a first and provides crucial evidence connecting the stripe wavevector with the LDOS gap (Fig. 5.30).

One may also ask if the two-stripe surface also shares the same nature. Unfortunately the data available is not sufficient for an adequate answer, certainly the stripes appear qualitatively similar to other CDW systems, in particular the chiral rotation of the sub-surface stripes [78] and this is suggestive of the potential bulk nature of the CDW phase. It is also possible that given the sensitivity of graphitic materials to doping [9] and the variable surface conditions already discussed in this section that the two-stripe surface is a subtle manipulation of the normal one stripe surface. Indeed there are other systems which exhibit both commensurate and incommensurate CDWs within the same material. [83, 124] Other qualitative similarities between the two stripe surfaces are also seen, namely that both surfaces are particularly flat and appear graphene-terminated, and that both phases exhibited a finite lifespan, something which was not observed for any of the other surface types reported.

6.1.3 A note on the bulk nature of the stripe phase

STM is a local and surface sensitive probe, the behaviour of the bulk cannot necessarily be extrapolated from the appearance of the surface. This is particularly important for HOPG-based samples, reports from Li *et al.* demonstrate that both graphene and graphite behaviour are exhibited at the surface of HOPG when measured by STM and STS. [125] This behaviour is explained as areas of the surface for which the top-most graphene sheet is electronically decoupled from the bulk of the sample. Since the samples measured are HOPG-based this may suggest some of the differences measured for the various surfaces of CaC_6 arise from changes in the coupling between the surface layer and the bulk of the material, i.e. some of the surfaces may be the result of highly-doped graphene and others of highly-doped graphite. In either case the data presented, including the CDW phase, are important for understanding CaC_6 and, perhaps even more interestingly, important for the study of doped graphene. Since neither the coupled nor decoupled regime are already independently characterised for a highly-doped system, differentiating between the two at this stage is not possible.

One potential scenario is that the bulk structure of the material matches the stripe phase and that the CDW and distortion are both seen throughout the sample below the transition temperature of 250 K. However, in other similar systems where CDWs have been observed by STM subsequent confirmation of the CDW in the bulk structure by X-ray scattering has not always been trivial, e.g. in the case of some cuprates. [45, 89] Another scenario is that the CDW in the bulk is of different character to that which has been seen at the surface. For example, this is the case in $NbSe_3$ [126], $NbSe_2$ [127], and $Bi_xCa_{1-x}MnO_3$. [109] The bulk CDW could differ in a number of ways; for example the symmetry, length scale or temperature dependence. It has been shown that the stripes in $TiSe_2$ [78], whilst apparently uni-directional at the surface, in fact rotate between successive layers of the sample, and furthermore that the rotation can occur clockwise or anticlockwise. Such an argument may support the proposition that the two-stripe phase is also CDW-related.

6.1.4 Potential mechanism of the CDW

Based on the measurements of the stripe phase seen in Section 5.6, namely the demonstrations of quasi-perfect imaging contrast inversion with bias polarity, association of the CDW wavelength with gapping of the LDOS, a lattice distortion of the of Ca superlattice, and the symmetry-breaking charge redistribution seen in imaging, the conclusion of a CDW is strong. Furthermore, the CDW contrast is shown to exist

on the graphene sheets (Fig. 5.24) whilst the CDW is compensated by distortion of the Ca lattice (Fig. 5.21) but no distortion is seen in the graphene (Fig. 5.22). The remarkable implication is that the graphene sheet hosts the ideal electrons-only CDW. Figs. 3.3 and 3.4 suggest that negative thermal expansion is important in stabilising the 250 K transition, which is likely associated to the CDW phase. Considering all of the above information, the following CDW mechanism is proposed. As the material is cooled, the negative thermal expansion of the graphene sheets flattens the planes, making an in-plane distortion of the Ca lattices between the graphene sheets (as observed) energetically favourable. The distortion is transverse and results in motion of charge on the graphene sheet immediately adjacent to the perturbed Ca atoms, leading to the observed stripe phase. Hence the coincidence of the distorted atom with the stripe peak in positive bias and the stripe trough in negative bias (Fig. 5.24). The hysteretic behaviour seen in magnetization is consistent with the one-way stripe decay observed in STM. This indicates that the stringent flat, high-purity sample conditions required to maintain the CDW cannot be recovered if the sample transforms out of the CDW phase, where the sample crumples to raise the surface roughness as shown in Figs. 5.10 and 5.20. These requirements also explain why below the CDW transition, the sample behaves as a better metal than when it is in its normal high-temperature state (Fig. 3.3).

It is natural to ask whether FS nesting drives the CDW formation in CaC_6 (see Chapter 2). There are several reported FS, determined both experimentally [34, 61] and theoretically [35, 58, 59]. These all exhibit the potential for nesting, namely that they have high symmetry, extended parallel portions of FS and significant density of states around the Fermi level. In spite of this, no nesting vectors matching the q-vector of the stripes are found. However, given various discrepancies between the candidate FS, such as missing or extra bands and differing values of charge transfer, together with the difficulties assigning the correct nesting vector for similar systems (for example, $NbSe_2$ [67, 68, 85]), one cannot discount this mechanism.

6.2 Impact of research

This section presents discussion of the impact of the research, in particular the significant impact in two fields: that of graphitic systems and in the field of superconductivity in 2D layered systems. Each is important, graphitic systems are believed to be extremely technologically important and a comprehensive understanding of their elec-

tronic behaviour and capabilities is vital for the realisation of such ambitions (Chapter 2). The results are indicative of shortcomings in existing theoretical models, which fail to predict a CDW, and of potential issues with published surface-sensitive measurements. The hitherto absence of a CDW in a superconducting graphitic system was a conspicuous gap in theories revolving around the ubiquity of these two phenomena (see Section 2.2.3). Furthermore, the application of FT-STS analysis to the study of a non-dispersing CDW feature is an innovative new demonstration of the analytical power of STM for characterising CDWs and other similar ground states.

The implications for graphitic systems and superconductivity follow from the fact that this is the first measurement of the CDW state in the highly-doped graphitic superconductor CaC_6. [1] The cleanliness and simplicity of this material compared with other layered superconductors makes it ideal for the study of the apparent ubiquity of CDWs and superconductivity in quasi-2D materials. In particular this material does not exhibit SDWs, quasi-particle scattering or strong Coulomb interactions which complicate the study of other high temperature superconducting systems which also exhibit CDWs. [80] The new results call in to question the completeness of DFT calculations used to model the electronic and phonon structures of CaC_6 [35, 58, 59] and other GICs [128], as these do not predict a CDW or striped phase. The results also highlight potential reasons for discrepancies between different ARPES studies [34, 61] - also a surface-sensitive technique - given the variety of surface scenarios encountered. Better understanding of these measurements and the true nature of CaC_6 will in time lead to a better understanding, and more universally accepted description, of the phonon and electron bands involved in the superconductivity of this class of materials.

6.3 Future directions

6.3.1 Further research in CaC_6

Additional research is required into both the bulk nature of the CDW phase, as discussed in Section 6.1, and the relationship between the CDW and superconductivity. It remains to be seen if the stripes continue to persist below the superconducting transition as shown for $NbSe_2$ in Chapter 4, or if the phases are competitive as discussed in Section 2.2.3. Furthermore, a number of new avenues of research into related materials, namely similar GICs and doped graphene, are suggested.

6.3.1.1 Non-STM and bulk measurements

Hydrostatic pressure is known to enhance superconductivity in CaC_6 [11], so it would be interesting to see if the same conditions enhance or suppress the CDW phase, this would be best achieved using a bulk measurement such as XRD through a diamond anvil cell. XRD would also present an opportunity to see if the symmetry, period and superlattice distortions observed in STM also occur in the bulk. Preliminary work has already begun for such a search, but successfully finding the CDW is not a trivial task. Difficulties arise from the fact that CDW peaks in XRD can have very low intensities, as low as 10^{-6} with respect to the the peaks for the primary structure. [89] Consequently, extremely high X-ray intensities are required. Matters are further complicated by the air sensitivity of the samples and the low temperature requirements.

Developing a better understanding of the surface is also vital to measuring the superconducting properties. Existing measurements not withstanding [3], it is natural to ask whether superconducting properties measured in STM on these materials convey valid information about the material's properties or whether they are influenced by the eccentricities of minority surface phases. Renewed studies of the FS, in particular by ARPES, may also reveal the portions of the FS which nest the CDW instability. [68]

6.3.1.2 STM studies

The temperature dependence of the stripe phases have not yet been documented, in order to confirm that the transition temperature is 250 K one would need to start from 78 K, following a detailed characterisation, and then increase the temperature of the system to document the transition temperature accurately. Likewise, in order to study the interaction with superconductivity one would need to observe the stripe phase as the temperature is reduced down to, and below, 11.5 K. A number of scenarios are possible, not only co-existence and competition, but also commensurate to incommensurate transitions. [83] It has been suggested that the relationship between superconductivity and CDWs is subtly different for commensurate and incommensurate systems. [69, 70] In particular early work on CDWs expected that incommensurate CDWs were a much stronger indication of potential superconductivity. [65] Similar to the use of pressure, magnetic fields can be applied to suppress the superconducting phase in order to search for associated enhancement or inhibition of the stripe phase. [89] Low temperature STM studies may be used to find the

behaviour of the stripes close to the superconducting phase, and magnetic field STM studies are also possible (e.g. in the UCL cryo-STM).

It remains to be confirmed, through the same detailed STS and SI-STM characterisation, if the two-stripe phase is indeed a CDW and if so what the relationship is to the single stripe phase. Ultimately the study of the two-stripe surface may link somewhat to the study of the bulk, or it may turn out to be an eccentricity of the sample surface. An important fact to note is that the tips used for the study of the two-stripe surface were made from Pt-Ir, whereas the tips used in the other studies reported were made from W (see Section 4.3.2). Tips are chosen to have a featureless DOS near to the Fermi level. However, there is a possibility that certain tip types interact with, or overlap differently with, the surface differently. For example, the ground state of Ir is $5d^7\ 6s^2$, Pt is $5d^9\ 6s^1$, and W is $5d^4\ 6s^2$. [129] This implies that each of these materials has a different d-orbital shape. This could in turn lead to differences in overlap between the tip and the surface states (Chapter 4), in particular sub-surface states such as stripes below the topmost layer. For this reason in the event of further STM studies the effect of tip material is worth exploring.

Having achieved successful AR imaging of the CaC_6 surface, and comprehensive characterisation of a number of surface types, it would be interesting to see if the different surface types exhibit differences in the superconducting phase. This may also be a way for STM, which has a somewhat surface-driven viewpoint, to reveal which surface type most closely reflects the measured bulk superconducting properties. [62, 130]

6.3.2 Further research in other GICs

The results are also suggestive of other avenues of research in the donor GIC class of materials. Recall from Chapter 2 that uni-directional stripe phases are reported in CsC_8 and RbC_8. [32] These stripes appear qualitatively similar to the stripes reported for CaC_6 perhaps warranting further study, in particular spectroscopic measurements. Note also that the authors reported the stripes had a finite lifetime of approximately 20 minutes, whilst this is somewhat low it is nevertheless indicative of yet another similarity to the stripe phase of CaC_6. The measurements reported by Anselmetti *et al.* were made at RT, which may explain the short lifespan, also if the stripes are CDW in origin then T_{CDW} is above RT, as reported for some other systems. [83] This may also suggest an avenue for enhancing the superconducting properties, by suppression of the stripe phases, of these materials and indicates important electronic

information about the entire class of donor GICs. Indeed a number of other GICs, such as YbC_6, share extremely similar structural and superconducting properties to CaC_6 [2, 9, 128] and logic would suggest that, much like other similar classes of materials, other striped or similar CDW phases may be discovered. Depending on whether such phases were co-operative or competitive with superconductivity new avenues to higher superconducting temperatures in donor GICs may be revealed.

Another important material in this class is BaC_6. This material shares a similar structure as the hexagonal phase of CaC_6 (Chapter 2). However, BaC_6 has not been shown to superconduct to 80 mK. [131] Given that Ba shares the same number of valence electrons as Ca, and that DFT predicts similar charge transfer, predicting superconductivity at low temperatures, it is surprising that this has not been found. [128] Furthermore, no successful real-space probe of the BaC_6 surface is reported. For these reasons it will be valuable to study the BaC_6 surface structure and electronic behaviour in the search of CDWs, superconductivity, and answers regarding the differences in the bulk properties of BaC_6 and CaC_6. Further to this, BaC_6 has a particularly large interlayer graphene-to-graphene spacing (greater than 0.5 nm) [9] implying maximum surface decoupling from the bulk. This suggests that it would be an excellent system for studying the effects of charge donation to graphene sheets in STM, in a similar manner to graphene-on-graphite STM studies. [125] In this vein one may also try to magnetically decouple the surface layers by applying a magnetic field in-plane inside a vector-magnet STM, enabling measurements of the surface graphene layer which is electrically isolated from the bulk graphitic material. Studies with similar techniques are performed on multi-layer metallic systems where 3D and 2D material behaviour can be controlled by the incident field. [132]

6.3.3 Further research in graphene

The data also represent a new demonstration of the remarkable rigidity of graphene—even with the very large density of mobile carriers donated by the Ca dopants, [34, 61] the large spectroscopic gap (Fig. 5.25) and other electronic manifestations of the CDW, no distortion of the carbon nuclei is detected (Fig. 5.22). Importantly this suggests that, within the graphene sheets, the dominant interaction is the electron–electron (e–e) repulsion and not the electron–phonon coupling that is clearly important for the Ca planes. The recent discoveries of the fractional quantum Hall effect, and hints of an insulating Wigner crystal phase in graphene [5, 15] also indicate that the e–e interaction has a more significant role in graphene than previously thought. The re-

sults hold out the tantalizing possibility that eventually a graphene-based field-effect transistor might allow sufficient electron-doping (1.5 eV shift of DOS in CaC_6 [34] typical maximum values in graphene through the field effect is currently 0.8 eV [133]) to induce a CDW and even superconductivity. Recent calculations [134] have demonstrated that it should be possible to reproduce the doping conditions of the graphene sheets in CaC_6 in isolated graphene, and indeed work towards such a goal is ongoing with successes reported in doping potassium monolayers onto graphene sheets. [135]

In closing, the CDW reported herein suggests new avenues of research for inducing CDWs and superconductivity in graphene, enhancement of superconductivity in GICs and presents a new class of 2D layered superconductors for the study of the interactions between these two ground states. Further study into the bulk nature of the stripes are necessary, as is study into the interactions between the stripe and superconducting phases.

Bibliography

[1] K. C. Rahnejat *et al.* Charge density waves in the graphene sheets of the superconductor CaC_6. *Nature Commun.*, 2:558, 2011.

[2] T. E. Weller, M. Ellerby, S. S. Saxena, R. P. Smith, and N. T. Skipper. Superconductivity in the intercalated graphite compounds C_6Yb and C_6Ca. *Nature Phys.*, 1:39 – 41, 2005.

[3] N. Bergeal *et al.* Scanning tunneling spectroscopy on the novel superconductor CaC_6. *Phys. Rev. Lett.*, 97:077003, 2006.

[4] X.-Q. Wang. Phases of the Au(100) surface reconstruction. *Phys. Rev. Lett.*, 67:3547 – 3550, 1991.

[5] X. Du, I. Shachko, F. Duerr, A. Luican, and E. Y. Andrei. Fractional quantum hall effect in insulating phase and dirac electrons in graphene. *Nature*, 462:192 – 195, 2009.

[6] K. S. Novoselov *et al.* Electric field effect in atomically thin carbon films. *Science*, 306:666 – 669, 2004.

[7] A. K. Geim and K. S. Novoselov. The rise of graphene. *Nature Mater.*, 6:183 – 191, 2007.

[8] A. H. Castro Neto. The electronic properties of graphene. *Rev. Mod. Phys.*, 81:109 – 162, 2009.

[9] M. S. Dresselhaus and G. Dresselhaus. Intercalation compounds of graphite. *Adv. Phys.*, 51:1 – 186, 2002.

[10] N. B. Hannay *et al.* Superconductivity in graphitic compounds. *Phys. Rev. Lett.*, 14:225 – 226, 1965.

[11] A. Gauzzi *et al.* Enhancement of superconductivity and evidence of structural instability in intercalated graphite CaC_6 under high pressure. *Phys. Rev. Lett.*, 98:067002, 2007.

[12] Y. Kaburagi, A. Yoshida, and Y. Hishiyama. Microtexture of highly crystallized graphite as studied by galvanomagnetic properties and electron channeling contrast effect. *J. Mater. Res.*, 11:769 – 778, 1995.

[13] J. D. Bernal. The structure of graphite. *Proc. R. Soc. Lond. A*, 106:749 – 773, 1924.

[14] G. Binnig *et al.* Energy-dependent state-density corrugation of a graphite surface as seen by scanning tunneling microscopy. *Europhys. Lett.*, 1:31, 1986.

[15] K. I. Bolotin, F. Gharhari, M. D. Shulman, H. I. Stormer, and P. Kim. Observation of the fractional quantum hall effect in graphene. *Nature*, 462:196 – 199, 2009.

[16] S. Bae *et al.* Roll-to-roll production of 30-inch graphene films for transparent electrodes. *Nature Nanotech.*, 5:574 – 578, 2010.

[17] T. Ihn *et al.* Graphene single-electron transistors. *Mater. Today*, 13:44 – 50, 2010.

[18] A. Lovell. *Tuneable graphite intercalates for hydrogen storage.* PhD thesis, University College London, 2007.

[19] E. J. Freise. Structure of graphite. *Nature*, 193:671 – 672, 1962.

[20] F. Maeda *et al.* Unoccupied-electronic-band structure of graphite studied by angle-resolved secondary-electron emission and inverse photoemission. *Phys. Rev. B*, 37:4482, 1988.

[21] M. Posternak *et al.* Prediction of electronic interlayer states in graphite and reinterpretation of alkali bands in graphite intercalation compounds. *Phys. Rev. Lett.*, 50:761, 1983.

[22] V. N. Strocov *et al.* Three-dimensional unoccupied band structure of graphite: Very-low-energy electron diffraction and band calculations. *Phys. Rev. B*, 61:4994, 2000.

[23] J.C. Slonczewski and P.R. Weiss. Band structure of graphite. *Phys. Rev.*, 109:272 – 279, 1958.

[24] A. Hagen. *Ladungsträgerdynamik in Kohlenstoff-Nanoröhren*. PhD thesis, Freie Unversität Berlin, 2005.

[25] L. Pietronero and S. Strässler. Bond-length change as a tool to determine charge transfer and electron-phonon coupling in graphite intercalation compounds. *Phys. Rev. Lett.*, 47:593, 1981.

[26] N. Emery *et al.* Superconductivity of bulk CaC_6. *Phys. Rev. Lett.*, 95:087003, 2005.

[27] X. r. Qin and G. Kirczenow. Theory of scanning-tunneling-microscopy images of intercalated graphite surfaces. *Phys. Rev. B*, 41:4976 – 4985, 1990.

[28] S. P. Kelty, Z. Lu, and C. M. Lieber. Scanning-tunneling-microscopy investigations of ternary graphite intercalation compounds. *Phys. Rev. B*, 44:4064 – 4067, 1991.

[29] T. Kinno, M. O. Watanabe, and K. Mizushima. Clean-surface study of stage-1 alkali-metal graphite intercalation compounds by scanning tunneling microscopy. *Phys. Rev. B*, 52:R11669 – R11671, 1995.

[30] H. P. Lang, R. Wiesendanger, V. Thommen-Geiser, and H.-J. Güntherodt. Atomic-resolution surface studies of binary and ternary alkali-metal-graphite intercalation compounds by scanning tunneling microscopy. *Phys. Rev. B*, 45:1829 – 1837, 1992.

[31] D. Anselmetti, R. Wiesendanger, and H. J. Güntherodt. Surface structure of donor graphite intercalation compounds by scanning tunneling microscopy. *Phys. Rev. B*, 39:11135 – 11138, 1989.

[32] D. Anselmetti, V. Geiser, G. Overny, R. Wiesendanger, and H. J. Güntherodt. Local symmetry breaking in stage-1 alkali-metal-graphite intercalation compounds studied by scanning tunneling microscopy. *Phys. Rev. B*, 42:1848 – 1851, 1990.

[33] G. A. Lindsell. *Structure and dynamics of graphite intercalation compounds*. PhD thesis, Australian National University, 1998.

[34] T. Valla *et al.* Anisotropic electron-phonon coupling and dynamical nesting on the graphene sheets in superconducting CaC_6 using angle-resolved photoemission spectroscopy. *Phys. Rev. Lett.*, 102:107007, 2009.

[35] M. Calandra and F. Mauri. Theoretical explanation of superconductivity in C_6Ca. *Phys. Rev. Lett.*, 95:237002, 2005.

[36] A. Hebard *et al.* Superconductivity at 18 K in potassium-doped c_60. *Nature*, 350:600, 1991.

[37] M. J. Rosseinsky *et al.* Superconductivity at 28 K in Rb_xc_60. *Phys. Rev. Lett.*, 66:2830 – 2832, 1991.

[38] Y. Iye *et al.* High-magnetic-field electronic phase transition in graphite observed by magnetoresistance anomaly. *Phys. Rev. B*, 25:5478 – 5485, 1982.

[39] D. D. L. Chung, G. Dresselhaus, and M. S. Dresselhaus. Intralayer crystal structure and order-disorder transformations of graphite intercalation compounds using electron diffraction techniques. *Mater. Sci. Eng.*, 31:107 – 114, 1977.

[40] J. Xhie, K. Sattler, M. Ge, and N. Venkateswaran. Giant and supergiant lattices on graphite. *Phys. Rev. B*, 47:15835 – 15841, 1993.

[41] M. F. Crommie, C. P. Lutz, and D. M. Eigler. Imaging standing waves in a two-dimensional electron gas. *Nature*, 363:524 – 527, 1993.

[42] Y. Takada. Unified model for superconductivity in graphite intercalation compounds: Prediction of optimum T_c and suggestion for its realization. *J. Phys. Soc. Jap.*, 78:013703, 2009.

[43] M. Laguës, J. E. Fischer, D. Marchand, and C. Fretigny. Angle resolved photoemission spectroscopy of CsC_8: Evidence for a charge density wave located at the surface. *Sol. State Commun.*, 67:1011 – 1015, 1988.

[44] C. Howald, H. Elsakl, N. Kaneko, and A. Kapitulnik. Coexistence of periodic modulation of quasiparticle states and superconductivity in $Bi_2Sr_2CaCu_2O_{8+\delta}$. *Proc. Natl. Acad. Sci.*, 100:9705 – 9709, 2003.

[45] W. D. Wise *et al.* Charge-density-wave origin of cuprate checkboard visualized by scanning tunnelling microscopy. *Nature Phys.*, 4:696 – 699, 2008.

[46] J. Singleton and C. Mielke. Quasi-two-dimensional organic superconductors: a review. *Contemp. Phys.*, 43:63 – 96, 2002.

[47] A. H. Castro Neto. Charge density wave, superconductivity, and anomalous metallic behaviour in 2D transition metal dichalcogenides. *Phys. Rev. Lett.*, 86:4382 – 4385, 2001.

[48] Gerald Burns. *Solid State Physics*. Academic Press, 1985.

[49] H. K. Onnes. The resistance of pure mercury at helium temperatures. *Commun. Phys. Lab. Univ. Leiden*, 12:120, 1911.

[50] H. K. Onnes. Further experiments with liquid helium. *Commun. Phys. Lab. Univ. Leiden*, 13:1093 – 1113, 1911.

[51] N. W. Ashcroft and N. D.Mermin. *Solid State Physics*. Saunders College Publishing, 1976.

[52] W. Meissner and R. Ochsenfeld. Ein neuer effekt bei eintritt der supraleitfähigkeit. *Naturwissenschaften*, 21:787 – 788, 1933.

[53] J. Bardeen, L. N. Cooper, and J. R. Schrieffer. Theory of superconductivity. *Phys. Rev. B*, 108:1175, 1957.

[54] C. Wang, B. Giambattista, C. G. Slough, R. V. Coleman, and M. A. Subramanian. Energy gaps measured by scanning tunneling microscopy. *Phys. Rev. B*, 42:8890 – 8906, 1990.

[55] J. G. Bednorz and K. A. Müller. Possible high T_c superconductivity in the Ba-La-Cu-O system. *Z. Physik B*, 64:189 – 193, 1986.

[56] D. Pines. *The spin fluctuation model for high temperature superconductivity: Progress and prospects*. NATO ASI. SpringerLink, 2002.

[57] G. Csányi, P. B. Littlewood, A. H. Nevidomskyy, C. J. Pickard, and B. D. Simons. The role of the interlayer state in the electronic structure of superconducting graphite intercalated compounds. *Nature Phys.*, 1:42 – 45, 2005.

[58] I. I. Mazin. Intercalant-driven superconductivity in YbC_6 and CaC_6. *Phys. Rev. Lett.*, 95:227001, 2005.

[59] A. Sanna *et al.* Anisotropic gap of superconducting CaC_6: A first-principles density functional calculation. *Phys. Rev. B*, 75:020511, 2007.

[60] D. G. Hinks, D. Rosenmann, H. Claus, M. S. Bailey, and J. D. Jorgensen. Large Ca isotope effect in the CaC_6 superconductor. *Phys. Rev. B*, 75:014509, 2007.

[61] K. Sugawara, T. Sato, and T. Takahashi. Fermi-surface-dependent superconducting gap in C_6Ca. *Nature Phys.*, 5:40 – 43, 2009.

[62] C. Kurter *et al.* Large energy gaps in C_6Ca from tunneling spectroscopy: Possible evidence of strong-coupling superconductivity. *Phys. Rev. B*, 76:220502, 2007.

[63] M. Sutherland *et al.* Bulk evidence of single-gap s-wave superconductivity in the intercalated graphite superconductor C_6Yb. *Phys. Rev. Lett.*, 98:067003, 2007.

[64] J. S. Kim, L. Boeri, R. K. Kremer, and F. S. Razavi. Effect of pressure on superconducting Ca-intercalated graphite CaC_6. *Phys. Rev. B*, 74:21413, 2006.

[65] G. Grüner. The dynamics of charge-density waves. *Rev. Mod. Phys.*, 60:1129 – 1181, 1988.

[66] G. Grüner. *Density waves in solids.* Addison-Wesley Longman, 1994.

[67] M.-H. Whangbo, E. Canadell, P. Foury, and J.-P. Pouget. Hidden fermi surface nesting and charge density wave instability in low-dimensional metals. *Science*, 252:5002, 1991.

[68] D. W. Shen *et al.* Primary role of the barely occupied states in the charge density wave formation of $NbSe_2$. *Phys. Rev. Lett.*, 101:226406, 2008.

[69] B. Spivak, P. Oreto, and S. A. Kivelson. Theory of quantum metal to superconductor transitions in highly conducting systems. *Phys. Rev. B*, 77:214523, 2008.

[70] S. A. Kivelson *et al.* How to detect fluctuating stripes in the high-temperature superconductors. *Rev. Mod. Phys.*, 75:1201 – 1241, 2003.

[71] R. E. Peierls. *Quantum Theory of Solids.* Oxford University Press, 1955.

[72] K. Iwaya *et al.* Electronic state of $NbSe_2$ investigated by STM/STS. *Physica B*, 329, 2003.

[73] W. Han, E. R. Hunt, O. Pankratov, and R. F. Frindt. Bias-dependent STM images of charge-density waves on TaS_2. *Phys. Rev. B*, 50:14746 – 14749, 1994.

[74] J. Zaanen and O. Gunnarsson. Charged magnetic domain lines and the magnetism of high-T_C oxides. *Phys. Rev. B*, 40:7391 – 7394, 1989.

[75] C. Brun *et al.* Charge-density waves in rubidium blue bronze $Rb_{0.3}MoO_3$ observed by scanning tunneling microscopy. *Phys. Rev. B*, 72:235119, 2005.

[76] I. Ekvall, H. E. Brauer, E. Wahlström, and H. Olin. Locally modified charge-density waves in Na intercalated VSe_2 studied by scanning tunneling microscopy and spectroscopy. *Phys. Rev. B*, 59:7751 – 7761, 1999.

[77] A. Fang, N. Ru, I. R. Fisher, and A. Kapitulnik. STM studies of $TbTe_3$: Evidence for a fully incommensurate charge density wave. *Phys. Rev. Lett.*, 99:046401, 2007.

[78] J. Ishioka *et al.* Chiral charge-density waves. *Phys. Rev. Lett.*, 105:176401, 2010.

[79] P. Mallet *et al.* Contrast reversal of the charge density wave STM image in purple potassium molybdenum bronze $K_{0.9}Mo_6o_{17}$. *Phys. Rev. B*, 60:2122 – 2126, 1999.

[80] K. McElroy *et al.* Relating atomic-scale electronic phenomena to wave-like quasiparticle states in superconducting $Bi_2Sr_2CaCu_2O_{8+\delta}$. *Nature*, 422:592 – 596, 2003.

[81] R. V. Coleman, B. Drake, P. K. Hansma, and G. Slough. Charge-density waves observed with a tunneling microscope. *Phys. Rev. Lett.*, 55:395 – 397, 1985.

[82] T. Valla *et al.* Quasiparticle spectra, charge-density waves, superconductivity, and electron-phonon coupling in 2H-$NbSe_2$. *Phys. Rev. B*, 92:086401, 2004.

[83] B. Sipos *et al.* From Mott state to superconductivity in 1T-TaS_2. *Nature Mater.*, 7:960 – 965, 2008.

[84] A. M. Gabovich *et al.* Competition of superconductivity and charge density waves in cuprates: Recent evidence and interpretation. *Adv. Cond. Matt. Phys.*, page 681070, 2010.

[85] S. V. Borisenko *et al.* Two energy gaps in fermi-surface arcs in $NbSe_2$. *Phys. Rev. Lett.*, 102:166402, 2009.

[86] H. Frölich. On the theory of superconductivity: The one-dimensional case. *Proc. R. Soc. Lond. A*, 223:296, 1954.

[87] O. Degtyareva *et al.* Competition of charge-density waves and superconductivity in sulfur. *Phys. Rev. Lett.*, 99:155505, 2007.

[88] A. M. Gabovich, A. I. Voitenko, and M. Ausloos. Charge- and spin-density waves in existing superconductors: competition between Cooper pairing and Peierls or excitonic instabilities. *Phys. Reports*, 367:53 – 709, 2002.

[89] J. Chang *et al.* Direct observation of competition between superconductivity and charge density wave order in $YBa_2Cu_3O_y$. http://arxiv.org/ftp/arxiv/papers/1206/1206.4333.pdf.

[90] S. Pruvost, C. Hérold, A. Hérold, and P. Lagrange. Structural study of novel graphite-lithium-calcium intercalation compounds. *Euro. J. Inorg. Chem.*, 2004:1661 – 1667, 2004.

[91] T. E. Weller. *Superconductivity in alkali-metal graphite intercalation compounds.* PhD thesis, University College London, 2005.

[92] V. Eremenko *et al.* Magnetostriction of charge density wave superconductor. *J. Low Temp. Phys.*, 24:979 – 980, 2006.

[93] T. Wanatabe, T. Fujii, and A. Matsuda. Anisotropic resistivities of precisely controlled single-crystal $Bi_2Sr_2CaCu_{8+\delta}$: systematic study on spin gap effect. *Phys. Rev. Lett.*, 79:2113 – 2116, 1997.

[94] J. Frenkel. On the electrical resistance of contacts between solid conductors. *Phys. Rev.*, 36:1604 – 1618, 1930.

[95] I. Giaever. Energy gap in superconductors measured by electron tunneling. *Phys. Rev. Lett.*, 5:147 – 148, 1960.

[96] I. Giaever and K. Megerle. Study of superconductors by electron tunneling. *Phys. Rev.*, 122:1101 – 1111, 1961.

[97] G. Binnig, H. Rohrer, Ch. Gerber, and E. Weibel. Tunneling through a controllable vacuum gap. *Appl. Phys. Lett.*, 40:178 – 180, 1982.

[98] G. Binning, H. Rohrer, Ch. Gerber, and E. Weibel. Surface studies by scanning tunneling microscopy. *Phys. Rev. Lett.*, 49:57 – 61, 1982.

[99] G. Binnig, H. Rohrer, Ch. Gerber, and E. Weibel. 7 x 7 reconstruction on si(111) resolved in real space. *Phys. Rev. Lett.*, 50:120 – 123, 1983.

[100] G. Binnig and H. Rohrer. Scanning tunneling microscopy. *Surf. Sci.*, 126:236 – 244, 1983.

[101] C. J. Chen. *Introduction to Scanning Tunneling Microscopy.* Oxford University Press, 1993.

[102] J. Bardeen. Tunnelling from a many particle point of view. *Phys. Rev. Lett.*, 6:57 – 59, 1961.

[103] J. Tersoff and D. R. Hamann. Theory and application for the scanning tunneling microscope. *Phys. Rev. Lett.*, 50:1998 – 2001, 1983.

[104] J. Tersoff and D. R. Hamann. Theory of the scanning tunneling microscope. *Phys. Rev. B*, 31:805 – 813, 1985.

[105] N. D. Lang. Resistance of a one-atom contact in the scanning tunneling microscope. *Phys. Rev. B*, 36:8173 – 8176, 1987.

[106] Y. Kohsaka. WaveMetrics Igor Pro 6 running the Kohsaka Macro analysis package.

[107] J. W. Cooley and J. W. Tukey. An algorithm for the machine calculation of complex fourier series. *Math. Comput.*, 19:297 – 301, 1965.

[108] B. Burk, R. E. Thomson, A. Zettl, and John Clarke. Charge-density-wave domains in 1T-TaS_2 observed by satellite structure in scanning-tunneling-microscopy images. *Phys. Rev. Lett.*, 66:3040 – 3043, 1991.

[109] C. Renner, G. Aeppli, B. G. Kim, Yeong-Ah Soh, and S. W. Cheong. Atomic-scale images of charge ordering in a mixed-valence manganite. *Nature*, 416:518 – 521, 2002.

[110] H. Jahn and E. Teller. Stability of polyatomic molecules in degenerate electronic states. I. Orbital degeneracy. *Proc. R. Soc. Lond. A*, 161:220 – 235, 1937.

[111] I. Ekvall, E. Wahlström, D. Claesson, H. Olin, and E. Olsson. Preparation and characterization of electrochemically etched W tips for STM. *Meas. Sci. Technol.*, 10:11 – 18, 1999.

[112] W. P. Dyke and J. K. Trolan. Field emission: Large current densities, space charge, and the vacuum arc. *Phys. Rev.*, 89:799 – 808, 1953.

[113] D. J. Coulman, J. Wintterlin, R. J. Behm, and G. Ertl. Novel mechanism for the formation of chemisorption phases: The (2x1)O-Cu(110) added row reconstruction. *Phys. Rev. Lett.*, 64:1761 – 1764, 1990.

[114] D. Tomanék *et al.* Theory and observation of highly asymmetric atomic structure in scanning-tunneling-microscopy images of graphite. *Phys. Rev. B*, 35:7790 – 7793, 1987.

[115] V. W. Brar *et al.* Scanning tunneling spectroscopy of inhomogeneous electronic structure in monolayer and bilayer graphene on SiC. *App. Phys. Lett.*, 91:122102, 2007.

[116] A. Deshpande, W. Bao, F. Miao, C. N. Lau, and B. J. LeRoy. Spatially resolved spectroscopy of monolayer graphene on SiO_2. *Phys. Rev. B*, 79:205411, 2009.

[117] S. Marchini, S. Günther, and J. Wintterlin. Scanning tunneling microscopy of graphene on Ru(0001). *Phys. Rev. B*, 76:075429, 2007.

[118] A. L. Tchougreeff and R. Hoffman. Charge and spin density waves in the electronic structure of graphite. Application to analysis of STM images. *J. Phys. Chem.*, 96:8993 – 8998, 1992.

[119] Experiments by collaborators at University College London and the University of Paris reveal a 1:1000 intensity peak in X-ray scattering measurements of CaC_6 and YbC_6 which correspond to a hexagonal phase of unit cell size 0.36 nm. Due to difficulties reconcilling this with any known MC_6 structure the data is as yet not published.

[120] J. Osing and I. V. Shvets. Bulk defects in graphite observed with a scanning tunnelling microscope. *Surf Sci.*, 417:145 – 150, 1998.

[121] Y. Kobayashi, K. i. Fukui, T. Enoki, K. Kusakabe, and Y. Kaburagi. Observation of zigzag and armchair edges of graphite using scanning tunneling microscopy and spectroscopy. *Phys. Rev. B*, 71:193406, 2005.

[122] K. Vey, R. A. Goschke, T. Buslaps, U. Walter, and F. Steglich. STM-mediated surface degradation on 1T-TaS_2. *Surf. Sci.*, 311:53 – 63, 1994.

[123] P. Mallet, H. Guyot, J. Y. Veuillen, and N. Motta. Charge-density-wave STM observation in η-Mo_4O_{11}. *Phys. Rev. B*, 63:165428, 2001.

[124] Yu. I. Latyshev *et al.* Interlayer tunneling spectroscopy of layered CDW materials. *J. Phys. IV France*, 131:197 – 202, 2005.

[125] G. Li, A. Luican, and E. Y. Andrei. Scanning tunneling spectroscopy of graphene on graphite. *Phys. Rev. Lett.*, 102:176804, 2009.

[126] C. Brun *et al.* Surface charge density wave phase transition in $NbSe_3$. *Phys. Rev. Lett.*, 104:256403, 2010.

[127] B. M. Murphy *et al.* Phonon modes at the 2H-$NbSe_2$ surface observed by grazing incidence inelastic x-ray scattering. *Phys. Rev. Lett.*, 95:256104, 2005.

[128] M. Calandra and F. Mauri. Possibility of superconductivity in graphite intercalated with alkaline earths investigated with density functional theory. *Phys. Rev. B*, 74:094507, 2006.

[129] Cotton and Wilkinson. *Advanced inorganic chemistry.* Interscience, 1972.

[130] R. S. Gonnelli *et al.* Evidence of gap anisotropy in CaC_6 from directional point-contact spectroscopy. *Phys. Rev. Lett.*, 100:207004, 2008.

[131] S. Nakamae *et al.* Absence of superconductivity down to 80 mk in graphite intercalated BaC_6. *Sol. Stat. Comms.*, 145:493, 2008.

[132] V. M. Krasnov, A. E. Kovalev, V. A. Oboznov, and N. F. Pedersen. Magnetic field decoupling and 3D-2D crossover in Nb/Cu multilayers. *Phys. Rev. B*, 54:15448, 1996.

[133] A. Das *et al.* Monitoring dopants by raman scattering in an electrochemically top-gated graphene transistor. *Nat. Nanotechnol.*, 3:210 – 215, 2008.

[134] M. Calandra, G. Profeta, and F. Mauri. Adiabatic and nonadiabatic phonon dispersion in a wannier function approach. *Phys. Rev. B*, 82:165111, 2010.

[135] C. A. Howard, M. P. M. Dean, and F. Withers. Phonons in potassium-doped graphene: The effects of electron-phonon interactions, dimensionality, and adatom ordering. *Phys. Rev. B*, 84:241404, 2011.